

Magnetic Fields in the Milky Way and in Galaxies ¹

Rainer Beck & Richard Wielebinski

Max-Planck-Institut für Radioastronomie, Bonn, Germany



Abstract. Most of the visible matter in the Universe is ionized, so that cosmic magnetic fields are quite easy to generate and due to the lack of magnetic monopoles hard to destroy. Magnetic fields have been measured in or around practically all celestial objects, either by in-situ measurements of spacecrafts or by the electromagnetic radiation of embedded cosmic rays, gas, or dust. The Earth, the Sun, solar planets, stars, pulsars, the Milky Way, nearby galaxies, more distant (radio) galaxies, quasars, and even intergalactic space in clusters of galaxies have significant magnetic fields, and even larger volumes of the Universe may be permeated by “dark” magnetic fields. Information on cosmic magnetic fields has increased enormously as the result of the rapid development of observational methods, especially in radio astronomy. In the Milky Way, a wealth of magnetic phenomena was discovered that are only partly related to objects visible in other spectral ranges. The large-scale structure of the Milky Way’s magnetic field is still under debate. The available data for external galaxies can well be explained by field amplification and ordering via the dynamo mechanism. The measured field strengths and the similarity of field patterns and flow patterns of the diffuse ionized gas give strong indication that galactic magnetic fields are dynamically important. They may affect the formation of spiral arms, outflows, and the general evolution of galaxies. In spite of our increasing knowledge on magnetic fields, many important questions on the origin and evolution of magnetic fields, like their first occurrence in young galaxies, or the existence of large-scale intergalactic fields remained unanswered. The present upgrades of existing instruments and several radio astronomy projects have defined cosmic magnetism as one of their key science projects.

KEYWORDS:

Cosmic rays – dynamo action – Faraday rotation – Galactic Center – galaxies: radio emission – halos – interstellar medium – jets – magnetic fields: origin, evolution, strength, structure – Milky Way: radio emission – polarization – pulsars – radio telescopes – spiral arms – synchrotron emission – Zeeman effect

1. Introduction

The first report of a cosmic magnetic field outside the Earth was the result of a direct measurement of the Zeeman effect in the magnetic fields in sunspots in 1908. In 1950 it was suggested that the observed cosmic rays would require magnetic fields for their creation and their containment within the Galaxy. Optical polarization observations were first successful in 1949. Polarization of optical and infrared emission can also be caused by elongated dust grains which are aligned in magnetic fields due to the Davis-Greenstein mechanism first described in 1951. This interpretation was not accepted for a long time in the optical astronomy community. With the advent of radio astronomy this controversy was resolved and an active study of magnetic fields could begin.

Radio astronomy began in 1932 with the detection of continuum radio emission from the Milky Way. It became quickly clear that the observed radio waves were of a non-thermal nature and an interpretation of this phenomenon was actively sought. This was given in 1950 – the radio emission is due to relativistic cosmic-ray electrons gyrating in magnetic fields, emitting radio waves by the synchrotron process – when the theory of synchrotron emission theory was developed. In particular, it was soon pointed out that synchrotron emission should be highly polarized. In fact, in homogenous magnetic fields, up to 75% linear polarization of the continuum emission is expected. This suggestion was taken up by observers of optical radiation who found in 1954 that the Crab Nebula was highly

¹ Revised version of Chapter 13 in: *Planets, Stars and Stellar Systems, Vol. 5, ed. G. Gilmore, Springer, Berlin 2013*

polarized and hence emitting light through the synchrotron process. The radio confirmation of the polarization of the Crab Nebula followed in 1957. The first definite detection of the linear polarization of the Galactic radio waves was published by in 1962. At the same time the polarization of the bright radio galaxy Cygnus A and the Faraday rotation of the polarization angles of the linearly polarized radio emission in Centaurus A were detected. Observations at two frequencies of a section of the Milky Way showed that the interstellar medium of the Milky Way can also cause Faraday effect. During this exciting time of definite detections of interstellar and extragalactic magnetic fields by observations of linear polarization, the Zeeman effect of radio spectral lines proved to be more elusive. Several groups attempted to measure magnetic fields by this direct method. It was in 1968 that finally the Zeeman effect at radio wavelengths was successfully observed in the absorption profile of the HI line in the direction of Cassiopeia A. From that time onward considerable data was collected on the distribution of magnetic fields in the Milky Way. The all-sky maps of synchrotron polarization obtained with ground-based radio telescopes and with the WMAP and PLANCK space observatories shed new light on the large-scale magnetic fields in the Milky Way.

In the optical and near-infrared ranges, polarization is produced by the different extinction along the minor and major axis of dust grains, while at far-infrared and submillimeter wavelengths the elongated dust grains themselves emit polarized emission that was first detected in the 1980s. Progress has been slow, until recently an increase in reliable data became possible with the advent of submillimeter telescopes on excellent sites and sensitive polarimeters. The PLANCK data on polarized dust emission opened a new era in studying magnetic fields in dense clouds of the Milky Way.

The first suggestions about the presence of magnetic fields in nearby galaxies were made in 1958, based on observations of the polarization of stars in the Andromeda galaxy, M31. In 1967 observations of the linear polarization of diffuse starlight started in bright nearby galaxies. In 1970 the polarization of stars in the Magellanic Clouds implied the presence of magnetic fields in these neighboring galaxies. Low-frequency radio observations of galaxies showed non-thermal spectra and hence indicated the presence of magnetic fields. The first detection of the linear polarization of the radio emission from nearby galaxies in 1972 led the way to massive improvement on our knowledge of the morphology of magnetic fields in galaxies. These early radio observations were in good agreement with the early optical polarization studies of galaxies. A history of radio polarization measurements was compiled by Wielebinski (2012).

In this review, the status of our knowledge about the magnetic fields in our Milky Way and in nearby star-forming galaxies is summarized. Magnetic fields are a major agent in the interstellar and intra-cluster medium and affect the physical processes in various ways. They contribute significantly to the total pressure which balances the gas disk of a galaxy against gravitation. Magnetic reconnection is a possible heating source for the interstellar medium (ISM) and halo gas. Magnetic fields affect the dynamics of the turbulent ISM and the gas flows in spiral arms. The shock strength in spiral density waves is decreased and structure formation is reduced in the presence of a strong field. The interstellar fields are closely connected to gas clouds. Magnetic fields stabilize gas clouds and reduce the star-formation efficiency to the observed low values. On the other hand, magnetic fields are essential for the onset of star formation as they enable the removal of angular momentum from protostellar clouds via ambipolar diffusion. MHD turbulence distributes energy from supernova explosions within the ISM and drives field amplification and ordering via the dynamo mechanism. In galaxies with low star-formation activity or in the outer disks, the magneto-rotational instability can generate turbulence and heat the gas. Magnetic fields control the density and distribution of cosmic rays in the ISM. Cosmic rays accelerated in supernova remnants can provide the pressure to drive a galactic outflow and generate buoyant loops of magnetic fields (through the Parker instability). Understanding the interaction between the gas and the magnetic field is a key to understand the physics of galaxy disks and halos and the evolution of galaxies.

The magnetic field of the Milky Way is of particular importance for experiments to detect *ultra-high-energy cosmic rays* (UHECRs). Results from the first years of AUGER indicate that the arrival directions of detected UHECRs with energies of more than 10^{19} eV show some coincidence with the positions of known nearby active galaxies. This interpretation only holds if the deflections in the magnetic fields of the intergalactic medium and the Milky Way halo are not too large. However, little is known about the structure and strength of the magnetic field in the halo of our Milky Way and beyond.

There is one class of galaxies where magnetic fields play a crucial role: “active” galaxies that are governed by a central Black Hole. The formation of jets and radio lobes can only be understood with

the presence of magnetic fields. The physics of these phenomena is quite different from that in “normal” star-forming galaxies and will not be discussed in this review.

Magnetic fields have also been detected in the intergalactic medium surrounding the galaxies in a cluster through observations of non-thermal diffuse radio halos and the Faraday effect of background radio sources seen through the cluster. These intracluster magnetic fields are probably generated by turbulent gas motions as the result of massive interactions between galaxies and the intracluster gas. Magnetic fields affect thermal conduction in galaxy clusters and hence their evolution. Intracluster magnetic fields are reviewed elsewhere (e.g. Feretti et al. 2012; Han 2017). Outflows from galaxies may have magnetized the intergalactic medium, so that the general intergalactic space may be pervaded with magnetic fields. Unfortunately, cosmic rays and dust grains are rare outside of galaxies and galaxy cluster, so that magnetic fields remain invisible.

Cosmological models of structure formation indicate that the intergalactic space is probably permeated by magnetic filaments. Galactic winds, jets from active galaxies, and interactions between galaxies can magnetize the intergalactic medium. The detection of magnetic fields in intergalactic filaments and observations of the interaction between galaxies and the intergalactic space is one of the important tasks for future radio telescopes. Until now the arguments for the presence of magnetic fields in the distant Universe is based on observations of the non-thermal radio emission and Faraday rotation in galaxies at high redshift. Magnetic fields existed already in QSOs at epochs with redshifts of at least $z \approx 5$ and in starburst galaxies at redshifts of at least $z \approx 4$, but the earliest magnetic fields are yet to be discovered (section 5).

For further reading, the books by Ruzmaikin et al. (1988), Wielebinski & Beck (2005), Rüdiger et al. (2013), Klein & Fletcher (2015), Lazarian et al. (2015), and Kronberg (2016) are recommended.

2. Observational methods

As the methods of measuring of magnetic fields have been discussed widely in the literature, a short summary of the methods clarifies the present limitations.

2.1 Optical and infrared polarization

Elongated dust grains can be oriented with their major axis perpendicular to the field lines by paramagnetic alignment (Davis & Greenstein 1951) or, more efficiently, by radiative torque alignment (Hoang & Lazarian 2008; 2014). When particles on the line of sight to a star are oriented with their major axis perpendicular to the line of sight (and the field is oriented in the same plane), the different levels of extinction along the major and the minor axis leads to polarization of the starlight, with the E-vectors pointing parallel to the field. This is the basis to measure magnetic fields with optical and near-infrared polarization, by observing individual stars or of diffuse starlight. Extinction is most efficient for grains of sizes similar to the wavelength. These small particles are only aligned in the medium between molecular clouds, not in the dense clouds themselves (Cho & Lazarian 2005).

The detailed physics of the alignment is complicated and depends on the magnetic properties of the particles. The degree of polarization p (in optical magnitudes) due to a volume element along the line of sight δL is given by Ellis & Axon (1978):

$$p = \frac{K B_{\perp}^2 \zeta \delta L}{N_H T_g T^{1/2}}$$

where T is the gas temperature,
 T_g the grain temperature,
 N_H the gas density,
 ζ the space density of grains,
 B_{\perp} the magnetic field strength perpendicular to the line of sight.

Light can also be polarized by scattering, a process unrelated to magnetic fields. This contamination is small when observing stars, but needs to be subtracted from diffuse light, requiring multi-colour measurements.

In the far-infrared (FIR) and submillimeter wavelength ranges, the emission of elongated dust grains is intrinsically polarized and scattered light is negligible. If the grains are again aligned perpendicular to the magnetic field lines, the E-vectors point perpendicular to the field. FIR polarimetry probes dust particles in the warm parts of molecular clouds, while sub-mm polarimetry probes grains with large sizes which are aligned also in the densest regions. The field strength can be crudely estimated from the velocity dispersion of the molecular gas along the line of sight and the dispersion of the polarization angles in the sky plane, the *Chandrasekhar-Fermi method* (Chandrasekhar & Fermi 1953), further developed for the case of a mixture of large-scale and turbulent fields by Hildebrand et al. (2009) and Houde et al. (2009).

2.2 Synchrotron emission

Charged particles (mostly electrons) moving at relativistic speeds (cosmic rays) around magnetic fields lines on spiral trajectories generate electromagnetic waves. Cosmic rays in interstellar magnetic fields are the origin of the diffuse radio emission from the Milky Way (Fermi 1949; Kiepenheuer 1950). For particles with a continuous power spectrum of energies, the maximum contribution at a given frequency comes from electrons with energy E (in GeV) emitting in a magnetic field with a component perpendicular to the line of sight of strength B_{\perp} (in μG) (Webber 1980):

$$\nu \approx 16 \text{ MHz } E^2 B_{\perp}$$

where B_{\perp} is the strength of the magnetic field component perpendicular to the line of sight.

The half-power lifetime of the observable synchrotron-emitting cosmic-ray electrons (CREs) is:

$$t_{\text{syn}} \approx 8.35 \cdot 10^9 \text{ yrs } B_{\perp}^{-2} E^{-1} \approx 1.06 \cdot 10^9 \text{ yrs } B_{\perp}^{-1.5} \nu^{-0.5}$$

where B_{\perp} is measured in μG , E in GeV, and ν in GHz.

The emissivity ε from cosmic-ray electrons with a power-law energy spectrum in a volume with a magnetic field strength B_{\perp} is given by:

$$\varepsilon \sim N_0 \nu^{(\gamma+1)/2} B_{\perp}^{(1-\gamma)/2}$$

where ν is the frequency,
 N_0 the density of cosmic-ray electrons per energy interval,
 γ the spectral index of the power-law energy spectrum of the cosmic-ray electrons ($\gamma \approx -2.8$ for typical spectra in the interstellar medium of galaxies).

A source of size L along the pathlength has the intensity:

$$I_{\nu} \sim N_0 B_{\perp}^{(1-\gamma)/2} L$$

A power-law energy spectrum of the cosmic-ray electrons with the spectral index γ leads to a power-law synchrotron spectrum $I \sim \nu^{\alpha}$ with the spectral index $\alpha = (\gamma + 1)/2$. The initial spectrum of young particles injected by supernova remnants with $\gamma_0 \approx -2.2$ (Caprioli 2011) leads to an initial synchrotron spectrum with $\alpha_0 \approx -0.6$. These particles are released into the interstellar medium. A stationary energy spectrum with continuous injection and dominating synchrotron loss has $\gamma \approx -3.2$ and $\alpha \approx -1.1$. If the cosmic-ray electrons escape from the galaxy faster than within the synchrotron loss time, the initial spectrum is observed. The diffusion coefficient D of high-energy cosmic-ray electrons with energies E larger than about 5 GeV depends on energy ($D = D_0 (E/E_0)^{\delta}$, where δ is the exponent of the energy dependence of the electron diffusion coefficient, $\delta \approx 0.3 - 0.6$, Blasi & Amato 2012), so that the spectral slopes become $\gamma \approx (\gamma_0 - \delta) \approx -2.8$ and $\alpha \approx (\alpha_0 - \delta/2) \approx -0.9$. The synchrotron spectrum can be flattened at low radio frequencies by absorption in thermal gas clouds or by ionization losses of CREs, or steepened at high radio frequencies by synchrotron or inverse Compton losses of CREs (Basu et al. 2015a).

The energy densities of cosmic rays (mostly relativistic protons + electrons), of magnetic fields and of turbulent gas motions, averaged over a large volume of the interstellar medium and averaged over time, are comparable (*energy equipartition*):

$$W_{\text{cr}} \sim \frac{B^2}{8\pi} \sim \frac{\rho v^2}{2}$$

where W_{cr} is the energy density of cosmic rays,
 $B^2 / 8\pi$ the energy density of the total magnetic field,
 $\rho v^2 / 2$ the energy density of turbulent gas motions with density ρ and velocity dispersion v .

On spatial scales smaller than the diffusion length of cosmic-ray electrons (typically a few 100 pc) and on time scales smaller than the acceleration time of cosmic rays (typically a few million years), energy equipartition is not valid.

Equipartition between the total energies of cosmic rays and magnetic fields allows us to estimate the total magnetic field strength:

$$B_{\text{eq}} \sim ((k+1) I_v / L)^{2/(5-\gamma)}$$

This revised formula by Beck & Krause (2005) (see also Arbutina et al. 2012) is based on integrating the energy spectrum of the cosmic-ray protons and assuming a ratio k between the number densities of protons and electrons in the relevant energy range. The revised formula may lead to significantly different field strengths than the classical textbook formula which is based on integration over the radio frequency spectrum. Note that the exponent of $2/7$ given in the minimum-energy formula in many textbooks is valid only for $\gamma = -2$. The widely used *minimum-energy* estimate of the field strength is smaller than B_{eq} by the factor $((1 - \gamma) / 4)^{2/(5-\gamma)}$, hence similar to B_{eq} for $\gamma \approx -3$. For cosmic-ray spectra flatter than $\gamma = -2$, the above formula is not valid, and the integration over the energy spectrum of the cosmic rays to obtain W_{cr} has to be restricted to a limited energy interval.

For electromagnetic particle acceleration mechanisms, the proton/electron number density ratio k for GeV particles is $\approx 40 - 100$ which follows from their different masses (Bell 1978). (For an electron-positron plasma, $k = 0$.) If energy losses of the electrons are significant, e.g. in strong magnetic fields or far away from their places of origin, the spectral index of the cosmic-ray electron spectrum becomes steeper than that of the cosmic-ray protons, so that k increases and the equipartition estimate is a lower limit of the true field strength. Due to the small exponent in the formula, the dependence on the input parameters is weak, so that even large uncertainties do not affect the result much. On the other hand, the nonlinear relation between I_v and B_{\perp} may lead to an overestimate of the true field strength when using the equipartition estimate if strong fluctuations in B_{\perp} occur within the observed volume. Another uncertainty occurs if only a small volume of the galaxies is filled with magnetic fields.

In spite of these uncertainties, the equipartition assumption provides a reasonable first-order estimate. Independent measurements of the field strength by the Faraday effect in “magnetic arms” leads to similar values (section 4.2). Furthermore, estimates of the synchrotron loss time based on the equipartition assumption can well explain the extent of radio halos around galaxies seen edge-on (see section 4.6). Finally, the magnetic energy density based on the equipartition estimate is similar to that of the turbulent gas motions (Fig. 20), as expected from turbulent field amplification. Note that the equipartition estimate still holds in starburst galaxies where secondary electrons can contribute significantly (Lacki & Beck 2013).

Combination of data from radio waves and γ -rays that are emitted by the same cosmic-ray electrons via bremsstrahlung, also yields field strengths similar to equipartition in the Large Magellanic Cloud (Mao et al. 2012) and in the starburst region of M82 (Yoast-Hull et al. 2013), but probably not in NGC253 (Yoast-Hull et al. 2014).

In our Galaxy the accuracy of the equipartition assumption can be tested directly, because there is independent information about the energy density and spectrum of local cosmic rays from in-situ measurements and from γ -ray data. Combination with the radio synchrotron data yields a local strength of the total field of $\approx 6 \mu\text{G}$ and $\approx 10 \mu\text{G}$ in the inner Galaxy. These values are similar to those derived from energy equipartition.

Linear polarization is a distinct signature of synchrotron emission. The emission from a single electron gyrating in magnetic fields is elliptically polarized. An ensemble of electrons shows only very low circular polarization, but strong linear polarization with the plane of the E vector normal to the magnetic field direction. The intrinsic degree of linear polarization p is given by:

$$p_0 = \frac{1 - \gamma}{7/3 - \gamma}$$

Considering galactic radio emission with $\gamma \approx -2.8$ a maximum of $p_0 = 74\%$ linear polarization is expected. In normal observing situations the percentage polarization is reduced due to fluctuations of the magnetic field orientation within the volume traced by the telescope beam (section 2.3) or by Faraday depolarization (section 2.4). The observed degree of polarization is also smaller due to the contribution of unpolarized thermal emission which may dominate in star-forming regions.

2.3 Magnetic field components

Table 1: Magnetic field components and their observational signatures

Field component	Notation	Geometry	Observational signatures
Total field	$B^2 = B_{\text{turb}}^2 + B_{\text{reg}}^2$	3D	Total synchrotron intensity, corrected for inclination
Total field perpendicular to the line of sight	$B_{\perp}^2 = B_{\text{turb},\perp}^2 + B_{\text{reg},\perp}^2$	2D	Total synchrotron intensity
Turbulent or tangled field (a)	$B_{\text{turb}}^2 = B_{\text{iso}}^2 + B_{\text{aniso}}^2$	3D	Total synchrotron emission, partly polarized, corrected for inclination
Isotropic turbulent or tangled field perpendicular to the line of sight	$B_{\text{iso},\perp}$	2D	Unpolarized synchrotron intensity, beam depolarization, Faraday depolarization
Isotropic turbulent or tangled field along line of sight	$B_{\text{iso},\parallel}$	1D	Faraday depolarization
Ordered field perpendicular to the line of sight	$B_{\text{ord},\perp}^2 = B_{\text{aniso},\perp}^2 + B_{\text{reg},\perp}^2$	2D	Intensity and vectors of radio, optical, IR or submm polarization
Anisotropic turbulent or tangled field perpendicular to the line of sight (b)	$B_{\text{aniso},\perp}$	2D	Intensity and vectors of radio, optical, IR or submm polarization, Faraday depolarization
Regular field perpendicular to the line of sight (b)	$B_{\text{reg},\perp}$	2D	Intensity and vectors of radio, optical, IR or submm polarization, Goldreich-Kylafis effect
Regular field along line of sight	$B_{\text{reg},\parallel}$	1D	Faraday rotation and depolarization, longitudinal Zeeman effect

Notes: (a) Turbulent fields and fields tangled by small-scale gas motions have different power spectra that can possibly be distinguished by future observations with high spatial resolution. (b) Anisotropic turbulent fields and regular fields cannot be distinguished by polarization observations with limited resolution; Faraday rotation helps.

The intensity of synchrotron emission is a measure of the number density of cosmic-ray electrons in the relevant energy range and of the strength of the *total magnetic field* component in the sky plane. Polarized emission emerges from *ordered fields*. As polarization angles are ambiguous by multiples of 180° , they cannot be used to distinguish *regular fields* with a well-defined direction within the telescope beam from *anisotropic turbulent fields*. The latter are generated from isotropic turbulent magnetic fields by compression or shearing gas flows and have a preferred orientation, but frequently reverse their direction on scales smaller than the telescope beam. Anisotropic fields increase the diffusion coefficient of cosmic-ray electrons and hence decrease their residence time in the galactic disk (Giacinti et al. 2017). Unpolarized synchrotron emission indicates *isotropic turbulent fields* with random directions which are amplified and tangled by turbulent gas flows.

Magnetic fields preserve their direction over the *coherence scale*, given by field tangling or by turbulence. The isotropic turbulent field B_{turb} can be described by cells with the size of the turbulence

scale. If N is the number of cells within the volume observed by the telescope beam, wavelength-independent *beam depolarization* occurs, in case of constant turbulence length (Sokoloff et al. 1998):

$$DP = p/p_0 = N^{-1/2}$$

If the medium is pervaded by an isotropic turbulent field B_{turb} (unresolved field with randomly changing direction) plus an ordered field B_{ord} (regular and/or anisotropic turbulent) with a constant orientation in the volume observed by the telescope beam, it follows for constant density of cosmic-ray electrons:

$$DP = 1 / (1 + q^2)$$

while for the equipartition case (Sokoloff et al. 1998):

$$DP = (1 + 3.5 q^2) / (1 + 4.5 q^2 + 2.5 q^4)$$

where $q = B_{\text{iso},\perp} / B_{\text{ord},\perp}$ (the components in the sky plane, with $B_{\text{iso},\perp} = B_{\text{iso}} \sqrt{2/3}$). The latter case gives larger DP values (i.e. less depolarization) than for the former case.

2.4 Faraday rotation and Faraday depolarization

The linearly polarized radio wave is rotated by the Faraday effect in the passage through a magneto-ionic medium (Fig. 1). This effect gives us another method of studying magnetic fields – their regular component along the line of sight. The rotation angle Φ of a polarized radio wave is given by:

$$\Phi = \lambda^2 RM$$

where λ is the wavelength of observation (in m) and
 RM the *Rotation Measure* (in rad m⁻²).

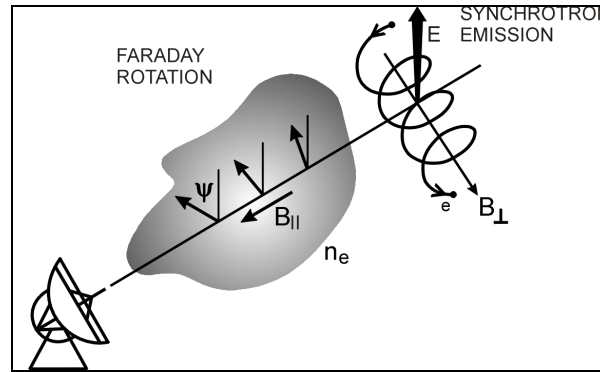


Fig. 1: Synchrotron emission and Faraday rotation.

RM is constant only in the rare cases when Φ is a linear function of λ^2 . Measurement of RM needs polarization observations in at least three frequency channels with a large frequency separation. In case of significant Faraday depolarization (see below), the polarization angle Φ is no longer a linear function of λ^2 . Deviations from the λ^2 law can also occur if several emitting and Faraday-rotating sources are located within the volume traced by the telescope beam. In such cases, RM varies with wavelength, and the *Faraday Depth* (FD) has to be used (Burn 1966):

$$\Phi = \lambda^2 FD$$

where
 with n_e the thermal electron density in cm⁻³,
 B_{\parallel} the mean strength of the magnetic field component along the line of sight in μG ,
 dl the pathlength along the magnetic field,
 L the pathlength from the source to the observer in parsec.

If the rotating region is located in front of the emitting region (*Faraday screen*), the values of RM and FD agree. In case of a single emitting and rotating region with a symmetric magnetic field profile and negligible Faraday depolarization (see below), the value of RM is half of the FD value. In other cases, *RM Synthesis* (see below) needs to be applied.

As the Faraday rotation angle is sensitive to the sign of the field direction, only regular fields give rise to Faraday rotation, while turbulent fields do not. For typical plasma densities and regular field strengths in the interstellar medium of galaxies, Faraday rotation becomes significant at wavelengths larger than a few centimeters. Only in the central regions of galaxies, Faraday rotation is strong already at 1 – 3 cm wavelength. Measurements of the Faraday rotation angle from multi-wavelength observations allow determination the strength and direction of the regular field component along the line of sight. Its combination with the total intensity and the polarization pseudo-vectors yields in principle the three-dimensional picture of galactic magnetic fields and the three field components regular, anisotropic turbulent and isotropic turbulent.

By definition, the regular magnetic field points towards the observer for $RM > 0$. The quantity $\langle n_e B_{\parallel} \rangle$ is the average of the product ($n_e B_{\parallel}$) along the line of sight which generally is not equal to the product of the averages $\langle n_e \rangle \langle B_{\parallel} \rangle$ if fluctuations in n_e and B_{\parallel} are correlated or anticorrelated. As a consequence, the field strength $\langle B_{\parallel} \rangle$ determined from RM is uncertain even if additional information about $\langle n_e \rangle$ is available, e.g. from pulsar dispersion measures (section 3.3.2).

In a region containing cosmic-ray electrons, thermal electrons and purely regular magnetic fields, wavelength-dependent Faraday depolarization occurs because the polarization planes of waves from the far side of the emitting layer are more rotated than those from the near side. This effect is called *differential Faraday rotation* and is described (for one single layer with a symmetric distribution of thermal electron density and field strength along the line of sight) by (Burn 1966; Sokoloff et al. 1998):

$$DP = p/p_0 = | \sin (2 RM \lambda^2) / (2 RM \lambda^2) |$$

where RM is the observed rotation measure. RM is half of the Faraday depth FD through the whole layer. DP varies periodically with λ^2 . With $|RM| = 100 \text{ rad m}^{-2}$, typical for normal galaxies, DP has zero points at wavelengths of $(12.5 \sqrt{n}) \text{ cm}$ where $n = 1, 2, \dots$ (Fig. 2).

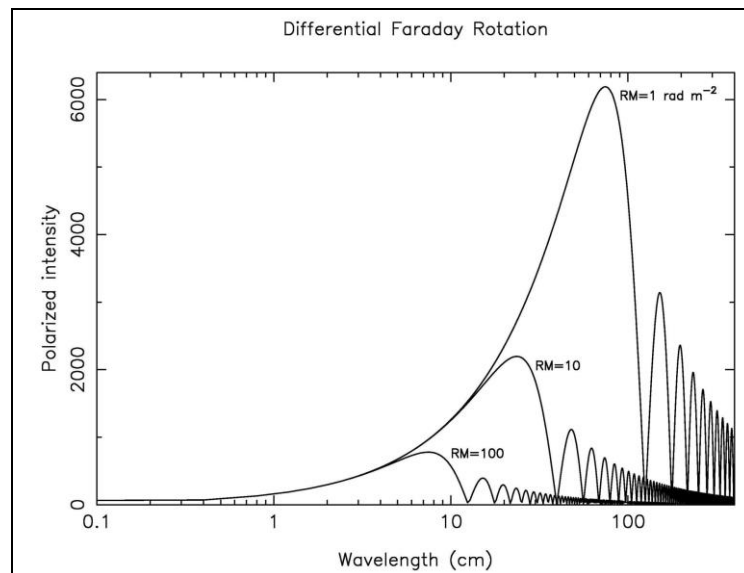


Fig. 2: Spectrum of polarized emission (in arbitrary units) for a synchrotron source with an intrinsic spectral index of $\alpha = -0.9$ (visible at short wavelengths) and depolarization by differential Faraday rotation (Arshakian & Beck 2011).

At each zero point of the curves in Fig. 2 the polarization angle jumps by 90° . Observing at a fixed wavelength hits zero points at certain values of the intrinsic RM, giving rise to *depolarization canals* along the level lines of RM. At wavelengths below that of the first zero point in DP, only the central

layer of the emitting region is observed, because the emission from the far side and that from the near side cancel (their Faraday rotation angles differ by 90°). Beyond the first zero point, only a small layer on the near side of the disk remains visible.

For multiple emitting and rotating layers within the telescope beam and/or the line of sight, the above equation and Fig. 2 are not valid and *RM Synthesis* needs to be applied (Brentjens & de Bruyn 2005). RM Synthesis Fourier-transforms the complex polarization data from a limited part of the λ^2 space into a data cube that provides at each point of the radio image a *Faraday spectrum* that gives the intensity of polarized emission (and its intrinsic polarization angle) as a function of FD. Each emitting source along the line of sight usually has its specific FD. The total span and the distribution of the frequency channels in λ^2 space define the resolution in the Faraday spectrum, given by the width of the *Rotation Measure Spread Function (RMSF)*. This allows cleaning of the Faraday spectrum, similar to cleaning of synthesis data from interferometric telescopes (Heald 2015). If the RMSF is sufficiently narrow, magnetic field reversals and turbulent fields can be identified from the Faraday spectrum (Frick et al. 2011; Bell et al. 2011; Beck et al. 2012). RM Synthesis is also able to separate FD components in the Faraday spectrum, generated by several emitting and rotating regions within the telescope beam and/or the line of sight, signature of the 3D structure of the magnetized medium. However, even simplified models of galaxies reveal complicated Faraday spectra (Ideguchi et al. 2014). Still, the shape of the Faraday spectrum can be used to extract global parameters of the magnetic field (Ideguchi et al. 2017).

Turbulent fields cause wavelength-dependent depolarization, called *Faraday dispersion* (Sokoloff et al. 1998). For an emitting and Faraday-rotating region (*internal dispersion*):

$$DP = p/p_0 = (1 - \exp(-S)) / S$$

where $S = 2 \sigma_{RM}^2 \lambda^4$. σ_{RM}^2 is the dispersion in rotation measure and depends on the turbulent field strength along the line of sight, the turbulence scale, the thermal electron density and the pathlength through the medium. The main effect of Faraday dispersion is that the interstellar medium becomes “Faraday thick” for polarized radio emission beyond a wavelength, depending on σ_{RM} (Fig. 3), and only a front layer remains visible in polarized intensity. Galaxy halos and intracluster media have typical values of $\sigma_{RM} = 1 - 10 \text{ rad m}^{-2}$, while for galaxy disks typical values are $\sigma_{RM} = 10 - 100 \text{ rad m}^{-2}$. Central regions of galaxies can have even higher dispersions. Fig. 3 shows the optimum wavelength ranges to detect polarized emission for these regions.

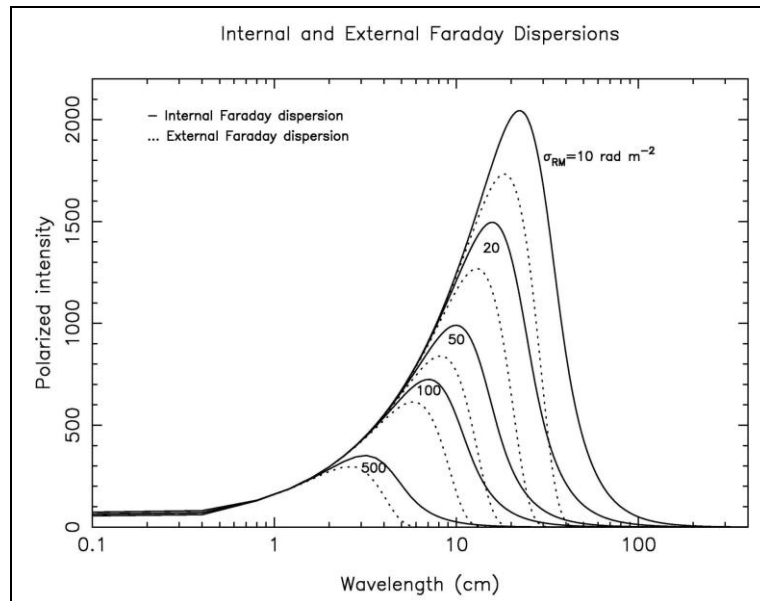


Fig. 3: Spectrum of polarized emission (in arbitrary units) for a synchrotron source with spectral index $\alpha = -0.9$ (visible at short wavelengths) and depolarization by Faraday dispersion parameterized by σ_{RM} . Solid curve: internal Faraday dispersion within an emitting source; dotted curve: external Faraday dispersion in a non-emitting object in the foreground (Arshakian & Beck 2011).

Regular fields in a non-emitting foreground *Faraday screen* do not depolarize, while turbulent fields do (*external Faraday dispersion*). For sources larger than the telescope beam:

$$DP = \exp(-S)$$

At long wavelengths $S = \sigma_{RM} \lambda^2$ (Tribble 1991). Unresolved *RM gradients* within the beam also lead to depolarization, similar to Faraday dispersion.

Wavelength-dependent Faraday depolarization is classified as *depth depolarization* (differential Faraday rotation, Faraday dispersion along the line of sight) and *beam depolarization* (RM gradients, Faraday dispersion in the sky plane). Both types occur in emitting regions, while in non-emitting Faraday screens only beam depolarization occurs.

2.5 Zeeman effect

The Zeeman effect is the most direct method of remote sensing of magnetic fields. It is used in optical astronomy since the first detection of magnetic fields in sunspots of the Sun. The radio detection was first made in the HI line. In the presence of a regular magnetic field B_{\parallel} along the line of sight, the line at the frequency ν_0 is split into two components (*longitudinal Zeeman effect*, Fig. 4):

$$\nu_0 \pm \frac{e B_{\parallel}}{4 \pi m c}$$

where e , m , and c are the usual physical constants. The two components are circularly polarized of the opposite sign. The frequency shift is minute, e.g. 2.8 MHz/Gauss for the HI line. More recent observation of the OH or H₂O lines used the larger frequency shifts of these molecular line species (e.g. Heiles & Crutcher 2005; McBride & Heiles 2013).

In magnetic fields perpendicular to the line of sight, two shifted lines together with the main unshifted line are all linearly polarized. This *transversal Zeeman effect* is much more difficult to observe. For unresolved and symmetric lines, no net polarization is observed. Detection of linearly polarized lines becomes possible for unequal populations of the different sublevels, a gradient in optical depth or velocity or an anisotropic velocity field, the *Goldreich-Kylafis effect* (Goldreich & Kylafis 1981). The orientation of linear polarization can be parallel or perpendicular to the magnetic field orientation. The effect was detected in molecular clouds, star-forming regions, outflows of young stellar systems and supernova remnants of the Milky Way and in the ISM of the galaxy M33 (Li & Henning 2011).

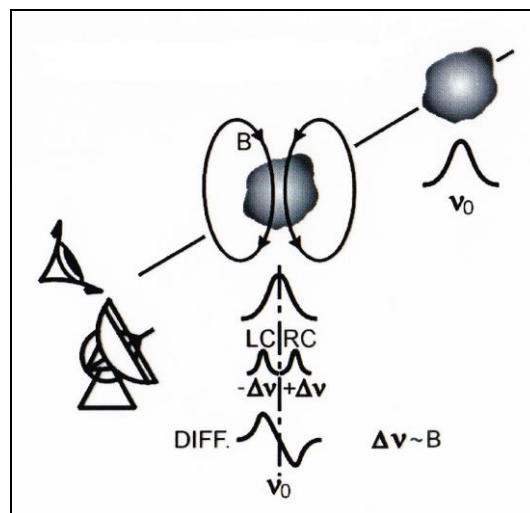


Fig. 4: The longitudinal Zeeman effect, splitting of a spectral line into two components with opposite circular polarization.

2.6 Field origin and amplification

The origin of the first magnetic fields in the Universe is still a mystery. The generation of the very first “seed” fields needs separation of electric charges. A large-scale intergalactic field of $\leq 10^{-12}$ G may be generated in the early Universe (Durrer & Neronov 2013). A lower limit of $\geq 10^{-16}$ G was derived from high-energy γ -ray observations with HESS and FERMI, assuming that the secondary particles are deflected by the intergalactic fields (Neronov & Vovk 2010). Analysis of the CMB power spectra from PLANCK data gave an upper limit of about 5 nG on a (comoving) scale of 1 Mpc (Ade et al. 2015b). Strong primordial fields would affect the formation of the first galaxies and hence the reionization of the intergalactic medium (IGM). The observation that the IGM was mostly ionized at a redshift of about 7 leads to an upper limit of 2 – 3 nG (Schleicher & Miniati 2011).

Models of field amplification in galaxies from large-scale primordial fields from early cosmological epochs (see a summary in Widrow 2002) are little developed and are not supported by the data. A large-scale seed field wound up in a differentially rotating galaxy can generate only the even bisymmetric mode (S1) or the odd dipolar mode (A0), but for both modes there is no convincing evidence so far (see Tables 5 – 7 in the Appendix). Furthermore, a large-scale primordial field is hard to maintain because galaxies rotate differentially, so that field lines get strongly wound up and destroyed by turbulent diffusion, in contrast to the observations (Shukurov 2005). For example, the large-scale regular field observed in M31 (Fig. 29), cannot be explained by the primordial field model. Similar issues occur with kinematical models of field amplification by shearing and compressing gas flows that can generate fields with a coherence length of less than a kiloparsec and frequent reversals.

A seed field of $\leq 10^{-12}$ G could be generated also in protogalaxies, e.g. by the *Weibel instability* (Lazar et al. 2009) or fluctuations in the intergalactic thermal plasma after the onset of reionization (Schlickeiser 2012; Schlickeiser & Felten 2013). Magnetization of protogalaxies to $\geq 10^{-9}$ G could also be achieved by field ejection from the first stars or the first black holes (Fig. 5) or the first supernova remnants (Hanayama et al. 2005), followed by dynamo action.

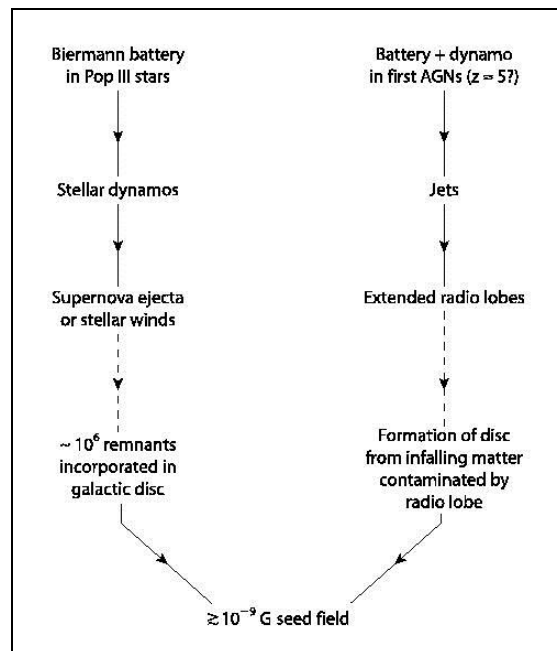


Fig. 5: Origin of seed fields in protogalaxies (Rees 2005).

The dynamo transfers mechanical into magnetic energy. It amplifies and orders a seed field. *The small-scale or fluctuation dynamo* does not need general rotation, only turbulent gas motions (Brandenburg & Subramanian 2005). The source of turbulence can be thermal virialization in protogalactic halos or supernovae in the disk or the *magneto-rotational instability (MRI)* (Rüdiger et al. 2013). Within less than 10^8 yr weak seed fields are amplified to about 10% of the energy density level

of kinetic turbulence, reaching strengths of a few μG (Kulsrud et al. 1997; Schleicher et al. 2010; Schober et al. 2012; A. Beck et al. 2012; Machida et al. 2013; Rieder & Teyssier 2016). However, due to the small viscosity and resistivity of the primordial gas, the magnetic Reynolds number and the magnetic Prandtl number have very high values, much higher than what can be reached in numerical simulations, so that the amplification rate and possibly the saturation level of the small-scale field will be underestimated (Schober et al. 2012).

The *large-scale dynamo* (α - Ω dynamo or α^2 dynamo) is driven by turbulent gas motions from supernova explosions or cosmic-ray driven Parker loops (α) and by differential rotation (Ω), plus magnetic diffusivity (η) (e.g. Parker 1979; Ruzmaikin et al. 1988; Beck et al. 1996). It generates a large-scale (“mean”) regular field from the turbulent field in a typical spiral galaxy within a few 10^9 yr. If the small-scale dynamo already amplified turbulent fields of a few μG in the protogalaxy, the large-scale dynamo is needed only for the organization of the field (“order out of chaos”). The field pattern is described by modes of order m in azimuthal symmetry in the plane and vertical symmetry (S) or antisymmetry (A) perpendicular to the plane. Several modes can be excited in the same object. In almost spherical, rotating bodies like stars, planets or galaxy halos, the strongest mode consists of a toroidal field component with a sign reversal across the equatorial plane (vertically antisymmetric or odd-symmetry mode A0 with azimuthal axisymmetry in the plane) and a poloidal field component of odd symmetry with field lines crossing the equatorial plane (Fig. 6). The halo mode can also be oscillatory and reverse its symmetry with time (e.g. causing the cycle of solar activity). The oscillation timescales (if any) are very long for galaxies and cannot be determined by observations.

In flat, rotating objects like galaxy disks, the α - Ω dynamo dominates. The strongest mode consists of a toroidal field component that is symmetric with respect to the equatorial plane and has the azimuthal symmetry of an axisymmetric spiral ($m = 0$) in the disk without a sign reversal across the plane (vertically symmetric or even-symmetry mode S0) and a weaker poloidal field component of even symmetry, also without a reversal of the vertical field component across the equatorial plane (Fig. 6). The next higher azimuthal mode is of bisymmetric spiral shape ($m = 1$) with two sign reversals in the plane, followed by more complicated modes. For a forcing with $m = 2$ symmetry (e.g. a two-arm spiral), the $m = 2$ and even $m = 4$ modes dominate over the $m = 1$ mode (Chamandy et al. 2013).

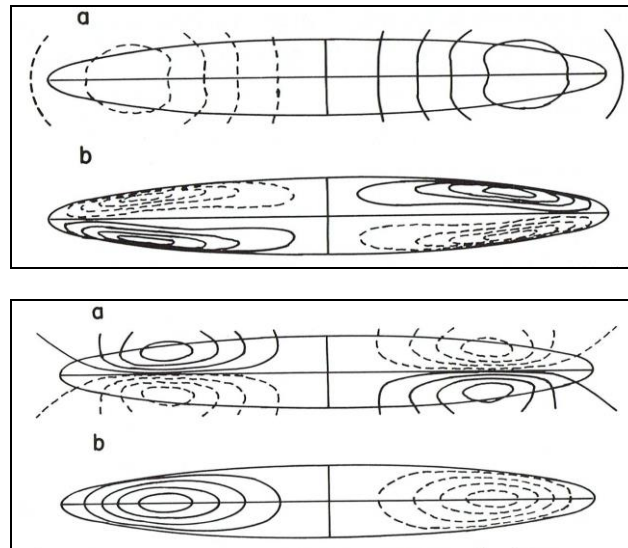


Fig. 6: Poloidal field lines (a) and contours of constant toroidal field strength (b) for the simplest version of an odd-symmetry dipolar (top) and an even-symmetry quadrupolar (bottom) dynamo field (Stix 1975). More realistic dynamo fields have many “poles”.

In principle, the halo and the disk of a galaxy may drive different dynamos and host different field modes. However, there is a tendency of “mode slaving”, especially in case of outflows from the disk into the halo. The more dynamo-active region determines the global symmetry, so that the halo and disk field should have the same symmetry (Moss et al. 2010). This seems to be the case in a few external galaxies (section 4.7), while our Milky Way seems to be different (section 3.5).

The ordering time scale of the α - Ω dynamo depends on the size of the galaxy (Arshakian et al. 2009). Very large galaxies may not yet have had sufficient time to build up a fully coherent regular field and may still host complicated field patterns, as often observed. The process of field ordering may also be interrupted by tidal interactions or merging with another galaxy which may destroy the regular field and significantly delay the development of coherent fields (section 5). Strong star formation as the result of a merger event or mass inflow amplifies the turbulent field and can suppress the α - Ω dynamo in a galaxy if the total star-formation rate is larger than about 20 solar masses per year. Continuous injection of small-scale fields by the small-scale dynamo in turbulent flows in star-forming regions may also decelerate the α - Ω dynamo and allow initial field reversals to persist (Moss et al. 2012).

The α - Ω dynamo generates large-scale magnetic helicity with a non-zero mean in each hemisphere of a galaxy. As total magnetic helicity is a conserved quantity, small-scale fields with opposite helicity are generated which suppress dynamo action, unless these are removed from the system (e.g. Vishniac et al. 2003). Hence, an outflow with moderate velocity related to star formation in the disk is essential for an effective α - Ω dynamo (Sur et al. 2007; Chamandy et al. 2014). This effect may relate the efficiency of dynamo action to the star-formation rate in the galaxy disk (Rodrigues et al. 2015). For fast outflows the advection time for the field becomes smaller than the dynamo amplification time, so that dynamo action is no longer efficient (Chamandy et al. 2015). α - Ω dynamo models including outflows with moderate velocities can also generate X-shaped fields (Moss et al. 2010).

Enhanced supply of turbulent magnetic fields by the small-scale dynamo in spiral arms may result in a concentration of large-scale regular magnetic fields between the material arms (Moss et al. 2013; 2015), as observed in many galaxies (section 4.4). A similar result was obtained by the inclusion of fast outflows from spiral arms that can suppress large-scale dynamo action (Chamandy et al. 2015).

There are several unsolved problems with dynamo theory (e.g. Vishniac et al. 2003). The “mean-field” approximation is simplified because it assumes a dynamical separation between the small and the large scales. The large-scale field is assumed to be smoothed by turbulent diffusion that may require fast and efficient field reconnection. One of the main future tasks is to compute the “mean” quantities α and η from the small-scale properties of the interstellar medium which is possible with numerical modelling. MHD simulations of dynamos driven by the buoyancy of cosmic rays in spiral galaxies (Hanasz et al. 2009), barred galaxies (Kulpa-Dybeł et al. 2011), dwarf galaxies (Siejkowski et al. 2014), and of dynamos driven by supernovae (Gressel et al. 2013; Gent et al. 2013) confirmed the overall concept of the α - Ω model.

The predictions of the α - Ω dynamo model are generally consistent by present-day observations (sections 4.4 and 4.7). The predicted pitch angles of the spiral field for the saturated dynamo state are reasonably consistent with the data (Chamandy et al. 2016). However, the quantitative comparison by Van Eck et al. (2015) did not reveal the expected correlations between observable quantities and predictions in most cases. Processes in addition to the dynamo are amplifying and shaping the field.

Improved dynamo models, with a spatial resolution of smaller than the turbulence scale of $\approx 10 - 50$ pc, should include the differentially rotating galaxy disk and halo and consider gravitational perturbations of gas density and velocity, possibly resulting in MHD spiral density waves (Lou et al. 1999) and field reversals (Dobbs et al. 2016). The multiphase interstellar medium has also to be taken into account (de Avillez & Breitschwerdt 2005).

Numerical MHD models of evolving galaxies are not yet able to resolve the turbulent scales, but include some kind of dynamo action. After the small-scale dynamo has reached saturation, the field strength is relatively low. Differential rotation forms spiral field segments, but the azimuthal component reveals many reversals (Machida et al. 2013; Pakmor et al. 2014; Rieder & Teyssier 2016). While the large-scale dynamo is not required to amplify the field from its primordial value, it needs to be included at later evolutionary stages to maintain the field strength by compensating dissipative losses and to build up a large-scale field order. The field strength may increase linearly in the disk by shear and finally reach or even exceed equipartition with the turbulent energy density (Pakmor et al. 2017), as observed (section 4.2), and hence affect galaxy evolution. However, none of the numerical models predicts magnetic spiral arms that are observed between the gaseous arms (section 4.4.1). Rapid progress in modelling galactic magnetic fields can be expected, triggered by future radio observations with higher resolution and sensitivity.

3. Magnetic fields in the Milky Way

3.1 Optical, infrared, and sub-mm polarization

The earliest optical polarization observations in 1949 were interpreted to be due to dust alignment in magnetic fields and hence a tracer of magnetic fields in galaxies. It took some time to convince the optical community that the polarization was due to dust grains aligned in magnetic fields. The radio polarization observations (section 3.2) confirmed the magnetic explanation. A large catalogue of the polarization of stars was made by Behr (1961). This work continued in the southern skies, as well as other observers, culminating in an all-sky catalogue of Mathewson & Ford (1970a) with 1800 entries and Axon & Ellis (1976) with 5070 entries. The general conclusion of this work, that there is a magnetic field aligned along the Galactic plane, still holds today. A very homogeneous region of alignment, with high polarization values, was seen towards the anticenter (Galactic longitude $l \approx 140^\circ$). Well aligned magnetic field vectors are also seen along the North Polar Spur that extends in to the northern halo from $l \approx 30^\circ$. These early observations were possible for nearby stars, a few at a maximal distance of 4 kpc. A more recent compilation of 9286 stars, collected by Heiles (2000) and discussed by Fosalba et al. (2002) (Fig. 7), included some stars out to ≈ 8 kpc. In view of these distance limitations it is not possible on the basis of optical polarization alone to model the magnetic field of the Milky Way. Constraints on the field symmetry could be set by Pavel et al. (2012), based on near-infrared starlight polarimetry along from $-75^\circ < b < +10^\circ$ at constant $l = 150^\circ$ (section 3.5).

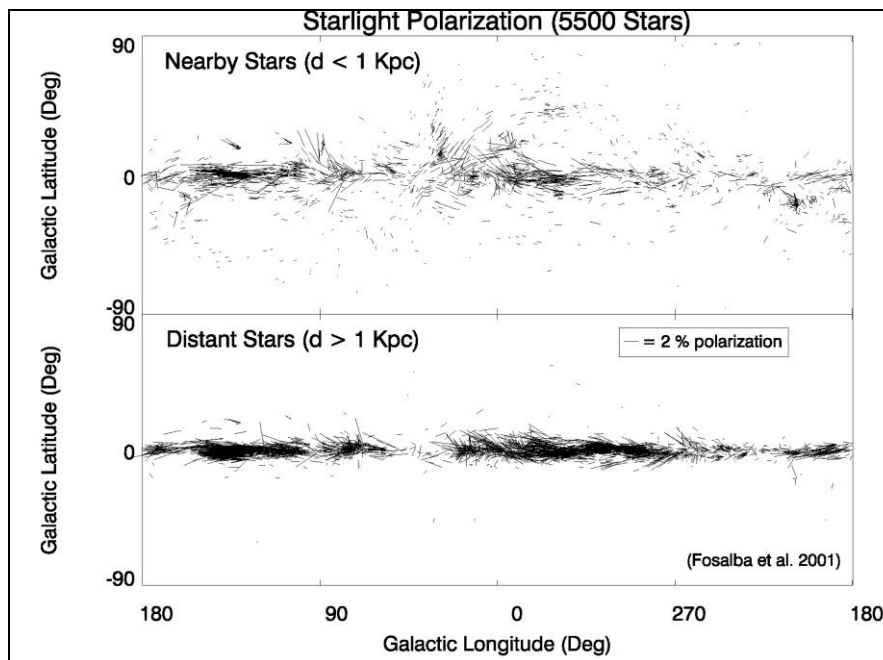


Fig. 7: Optical starlight polarization in the Galactic plane for two distance intervals (Fosalba et al. 2002).

Polarization observations of the diffuse far-infrared or sub-mm emission in the Milky Way are restricted to dense molecular/dust clouds. The Chandrasekhar-Fermi method (section 2.1) gives field strengths of a few mG, similar to Zeeman measurements of OH maser lines in other dense clouds (section 3.4). Interferometric observations in the sub-mm range with sub-parsec resolution reveals hourglass morphologies in the envelopes of dust cores in the molecular clouds associated with ultra-compact HII regions (Tang et al. 2009). The supercritical cores seem to collapse in a subcritical envelope supported by strong magnetic fields, suggesting that ambipolar diffusion plays a key role in the evolution of the cloud. The correlation of the field orientation in the intercloud medium on a scale of several 100 pc, derived from optical polarization, with that in the cloud core on a scale of less than 1 pc, derived from sub-mm polarimetry, further indicates that the fields are strong and preserve their orientation during cloud formation (Li et al. 2009).

3.2 Radio continuum

3.2.1 All-sky surveys in total intensity

The radio continuum emission of the Milky Way and star-forming galaxies at frequencies below 10 GHz mostly originates from the synchrotron process and hence traces the distribution of magnetic fields and cosmic rays. The contribution of thermal radio emission is generally small, except in bright star-forming regions. Only at frequencies higher than 10 GHz the thermal emission may dominate locally. At frequencies below about 300 MHz absorption of synchrotron emission by thermal gas can become strong. Hence, the observation of total radio continuum intensity in the frequency range of about 300 MHz – 10 GHz is a perfect method to investigate magnetic fields. Since the observed intensity is the integral from many emission areas along the line of sight, its interpretation is not always simple. Furthermore, the angular resolution of all-sky surveys (Fig. 10) is limited and hence cannot show the details of extended sources.

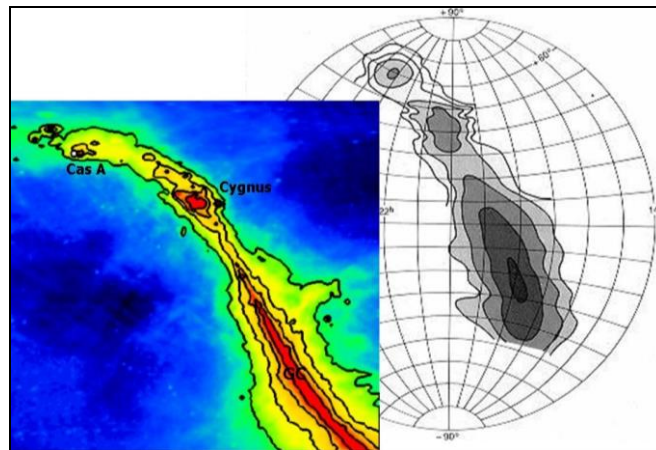


Fig. 8: The early sky map at 160 MHz of Reber (1944) (black-white) and a recent map at 1.4 GHz (colour) (courtesy Wolfgang Reich).

Numerous radio continuum surveys from the early days of radio astronomy (Appendix, Table 2) showed Galactic emission with a maximum towards the Galactic center, a band of emission along the Galactic plane, maxima in the tangential directions of the local spiral arm: Cygnus ($l \approx 80^\circ$) in the northern and Vela ($l \approx 265^\circ$) in the southern skies and some “spurs” of emission. In addition a few strong extragalactic sources were seen superposed on the Galactic emission.

The analysis of total synchrotron emission gives an equipartition strength of the total field of $6 \pm 2 \mu\text{G}$ in the local neighborhood and $10 \pm 3 \mu\text{G}$ at 3 kpc radius (Berkhuijsen, in Beck 2001). The radial exponential scale length of the total field is about 12 kpc. These values are similar to those in external galaxies (section 4.2).

Voyager 1 reached interstellar space in 2012 and measured a smooth increase in field strength to $4.8 \pm 0.4 \mu\text{G}$ (Burlaga & Ness 2016). This value is very close to the equipartition value and to those obtained with other methods (see below).

The angular resolution has improved so that at present all-sky surveys with resolution of under 1° are available (see Table 4 of the Appendix). At 1.4 GHz the surveys delineated many extended Galactic sources (HII regions, SNRs) seen along the Galactic plane. Some extragalactic sources like Centaurus A, Virgo A, Cygnus A and the Magellanic Clouds are also clearly seen in the surveys. Surveys at 45 MHz covered most of the sky with medium angular resolution. At these low frequencies, absorption of the synchrotron emission by ionized gas takes place near the Galactic plane.

The WMAP satellite surveys at frequencies from 23 GHz to 94 GHz (Bennett et al. 2003; Hinshaw et al. 2009) gave us a new view of the radio continuum sky at high radio frequencies. At the highest WMAP frequencies mainly thermal emission originating in interstellar dust is observed. An additional component due to spinning dust has been postulated (Draine & Lazarian 1998), to be seen in the 10 –

100 GHz frequency range. This spinning dust component has been confirmed (Dobler et al. 2009) in the WMAP data set. The PLANCK satellite provided further improved all-sky surveys between 20 GHz and 100 GHz (Ade et al. 2016).

To fill the gap between the lower-frequency and the high-frequency data, surveys in the range 2 – 10 GHz with compatible angular resolution are needed. The southern sky has been observed at 2.3 GHz with the Parkes telescope (S-PASS; Carretti et al., in prep.). The northern sky has been observed at 5 GHz with a 6.1-m telescope at OVRO; observations of the southern sky with a 7.6-m MeerKAT telescope are underway (C-BASS; King et al. 2014). Table 2 in the Appendix lists the all-sky surveys with the best angular resolution at a given frequency.

3.2.2 All-sky surveys in linear polarization

Linear polarization of the continuum emission is a more direct indicator of magnetic fields, because there is no confusing thermal component. However, linear polarization is subject to Faraday effects (section 3.3). After the first detections of polarized Galactic radio waves in 1962 (Fig. 9) several all-sky or all-hemisphere polarization surveys were made or are underway (Appendix, Table 3). The early polarization surveys did not have sufficient angular resolution to elucidate many details and were made at 408 MHz where Faraday effects are considerable. A multi-frequency collection of polarization data for the northern sky was published by Brouw & Spoelstra (1976), albeit not fully sampled.

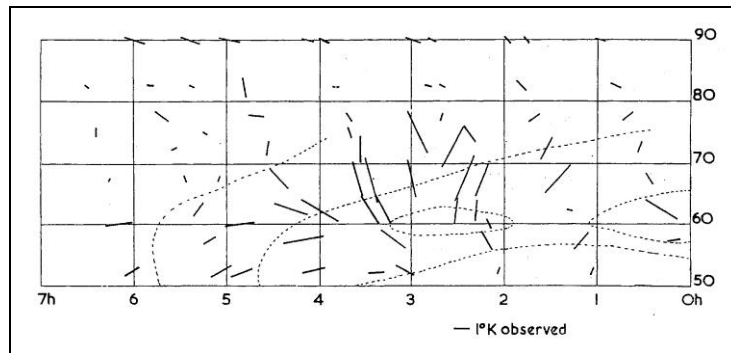


Fig. 9: First detection of polarized synchrotron emission (E-vectors) in the Milky Way at 408 MHz (Wielebinski et al. 1962).

Major progress was achieved by Wolleben et al. (2006) and Testori et al. (2008) who mapped the whole sky in linear polarization at 1.4 GHz with the 26-m DRAO and 30-m Villa Elisa telescopes with an angular resolution of 36 arcminutes (Fig. 10). Several polarization maxima are seen, e.g. towards the “Fan region” at $l \approx 140^\circ$, $b \approx 10^\circ$, where the line of sight is oriented perpendicular to the local spiral arm. The “North Polar Spur” (NPS) emerges from the Galactic plane at $l \approx 30^\circ$, as well as additional spur-like features that are the results of magnetic fields compressed by expanding supernova remnants. In polarization, the NPS can be followed to the southern sky. Towards the inner Galaxy (Galactic longitude $90^\circ > l > 270^\circ$, Galactic latitude $|b| < 30^\circ$) strong turbulence in polarized intensity is seen, due to Faraday effects on small scales (section 2.4). Diffuse polarized in the NRAO VLA sky survey (NVSS) has been analyzed by Rudnick & Brown (2009). All-sky polarization data at 23 GHz was published by the WMAP team (Kogut et al. 2007; Hinshaw et al. 2009). There is good agreement between the 23 GHz and the 1.4 GHz polarization maps in the polarization features away from the Galactic plane, but the high-frequency map shows less Faraday depolarization towards the inner Galaxy and near the plane.

The PLANCK satellite has provided new polarization surveys in six frequency bands (30 – 350 GHz) with high sensitivity (Ade et al. 2016). The 345 GHz data refers to the dust polarization (Ade et al. 2015a) which is crucial to separate foreground synchrotron emission, spinning dust radiation, and the Cosmic Microwave Background contribution. The diffuse low-frequency Galactic foregrounds are discussed in Ade et al. (2016). A combination of PLANCK and WMAP data allowed the construction of all-sky polarized synchrotron emission maps above a few GHz. The conclusion of this study is that

most of the polarized emission, and hence indicators of magnetic fields, are associated with distant large-scale loops and filaments of Galactic emission that imply organized magnetic fields.

Another major survey, called Global Magneto-Ionic Medium Survey (GMIMS), has been started which will cover the whole sky at frequencies between 300 MHz and 1.8 GHz and will allow the measurement the Faraday depth of the diffuse emission over the whole sky (Wolleben et al. 2009). First science results from the northern sky (GMIMS-HBN) were presented by Wolleben (2010b), Sun et al. (2015), and Hill et al. (2017). A $5^\circ \times 90^\circ$ strip along the Galactic meridian $l = 254^\circ$ was observed with the Parkes telescope at 2.3 GHz (Carretti et al. 2010), a precursor of the C-PASS survey of the southern hemisphere (Carretti et al., in prep.). Iacobelli et al. (2014) used C-PASS polarization data and found indications for interstellar turbulence in the transonic regime. A concentration of strong polarization gradients was found above the Galactic center, associated with the giant magnetic outflows known as the Fermi bubbles (Robitaille et al. 2017). Another all-sky polarization surveys at 5 GHz (C-BASS) is underway. A summary of all-sky or all-hemisphere polarization surveys is given in Reich (2006) and in Table 3 of the Appendix.

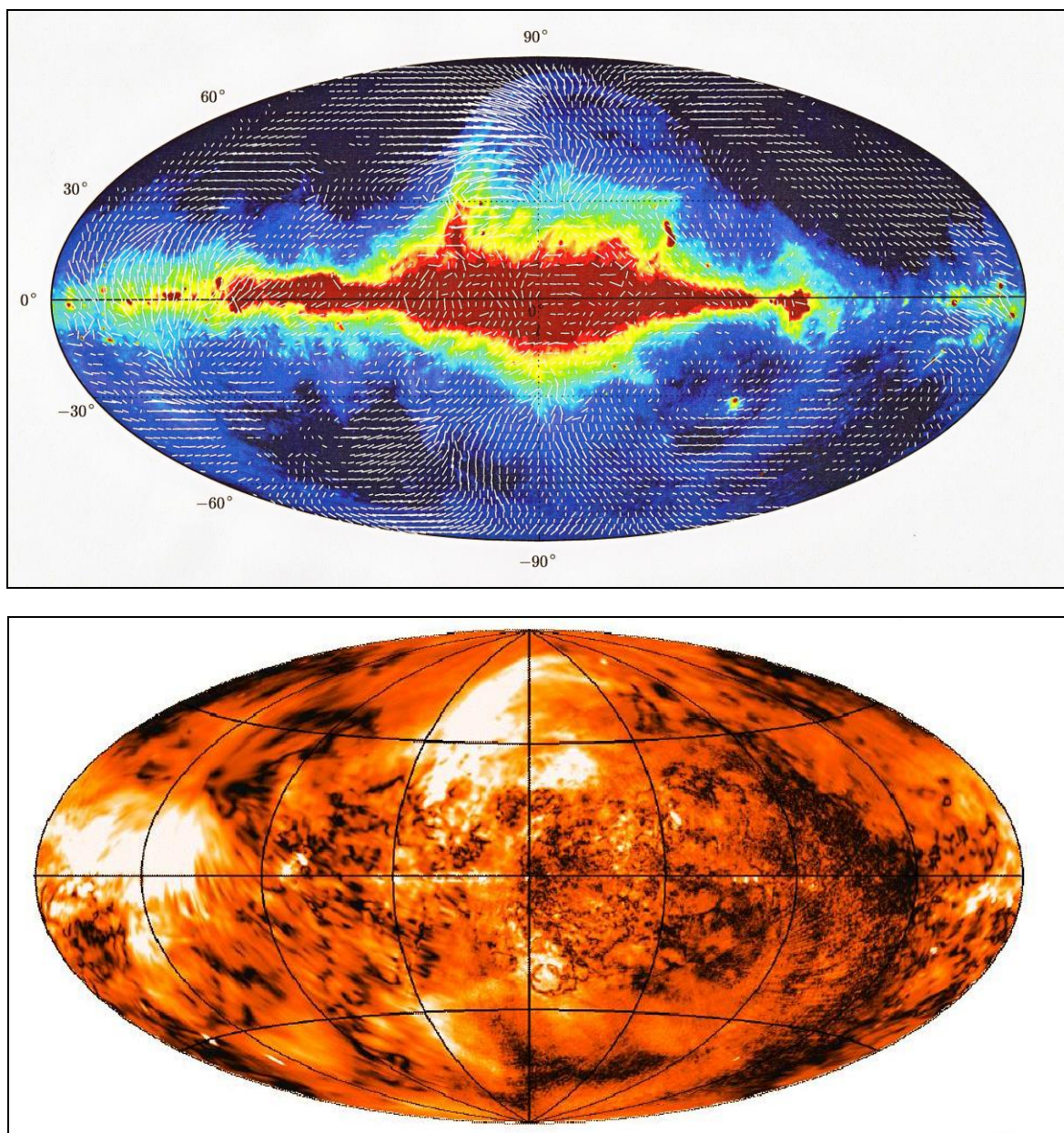


Fig. 10: All-sky surveys in total intensity with superimposed polarization E-vectors (top) and polarized intensity (bottom) at 1.4 GHz (Reich 1982; Wolleben et al. 2006; Testori et al. 2008) (image courtesy: Maik Wolleben and Wolfgang Reich).

Galactic plane surveys were performed from the earliest days of radio astronomy to delineate the extended Galactic sources like supernova remnants and HII regions, usually with no linear polarization data (Appendix, Table 4). Many of the published Galactic plane surveys between 22 MHz and 10 GHz cover only a narrow strip along the Galactic plane in the inner Galaxy. Total intensity surveys at several frequencies were used to separate the thermal HII regions (with a flat radio spectrum) from the steep-spectrum non-thermal sources (supernova remnants). From the total intensity surveys numerous previously unknown supernova remnants could be identified.

Since non-thermal sources are polarized it was obviously necessary to map the Galactic plane also in linear polarization. The first step in the evolution of our knowledge about the polarization of the Galactic plane was the 2.7 GHz survey by Junkes et al. (1987), followed by the surveys of the southern Galactic plane at 2.3 GHz (Duncan et al. 1995) and the northern counterpart at 2.7 GHz (Duncan et al. 1999) which covered a relatively wide strip ($|b| < 5^\circ$) around the plane. Early high-resolution observations by Wieringa et al. (1993) showed that a lot of small-scale polarization is present in the Galactic emission which is unrelated to any structures in total intensity. The next major development is the Effelsberg Medium Latitude Survey (EMLS) at 1.4 GHz that covers $\pm 20^\circ$ distance from the Galactic plane and is partly processed (Uyaniker et al. 1999; Reich et al. 2004). A section of the southern Galactic plane has been mapped at 1.4 GHz with arcminute resolution (Gaensler et al. 2001; Haverkorn et al. 2006), complemented on the northern sky by the CGPS survey (Taylor et al. 2003; Landecker et al. 2010) (Fig. 11).

In all these surveys *Faraday effects* (section 2.4) play an important role. At frequencies of 1.4 GHz and below, Faraday rotation generates small-scale structures in polarization which are not related to physical structures. Even at 5 GHz Faraday rotation occurs near the Galactic plane ($|b| < 5^\circ$). With high angular resolution, Faraday rotation leads to complete depolarization at certain values of Faraday rotation measure (RM) (Fig. 2), showing up as “canals” in the maps of polarized intensity (e.g. Haverkorn et al. 2003; 2004; Schnitzeler et al. 2009; Fig. 11). However, a careful determination of the extended background emission is necessary for a reliable determination of polarized intensity, polarization angles, and Faraday depth (FD). After adding the large-scale emission to the maps of Stokes Q and U (“absolute calibration”) at 1.4 GHz, most of the “canals” disappear. Some of the canals, especially those observed with LOFAR around 150 MHz (e.g. Jelić et al. 2015), are probably still depolarization structures. They mark the edge of filaments where FD changes rapidly. A method devised to distinguish canals made by irregularities in the medium from canals due to instrumental effects is the “polarization gradient” method introduced by Gaensler et al. (2011).

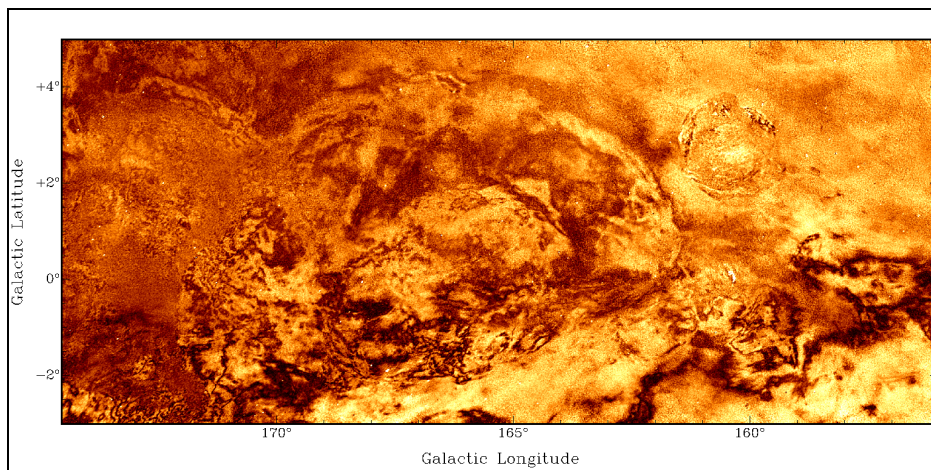


Fig. 11: A section of the Galactic plane in polarized intensity at 1.4 GHz (Landecker et al. 2010).

As a second new phenomenon, “Faraday screens” were discovered (e.g. Gray et al. 1998; Uyaniker et al. 1999; Wolleben & Reich 2004; Schnitzeler et al. 2009). These are foreground clouds of diffuse thermal gas and magnetic fields which Faraday-rotate or depolarize the extended polarized emission from the background. In addition to the well-known polarized SNRs and unpolarized HII regions, ionized envelopes of molecular clouds, pulsar-wind nebulae, and planetary nebulae were identified as Faraday screens. Depending on their Faraday rotation angle and the polarization angle of the

background emission, such screens may appear bright or dark. Such observations can trace magnetic structures on sub-parsec scales.

The present data set on the intensity distribution and polarization of the Galactic plane (Table 4 of the Appendix) is impressive. Sensitive surveys at higher radio frequencies allow a systematic study of the Faraday Screen phenomenon, e.g. by a Sino-German survey of the Galactic plane at 5 GHz with the Urumqi telescope (Sun et al. 2007; 2011; 2014; Gao et al. 2010; Xiao et al. 2011). Sun et al. (2014) investigated absolutely calibrated radio polarimetry data of the inner Galactic plane at 2.3 and 4.8 GHz and concluded that there is considerable depolarization in the 2.3 GHz emission.

The first polarization data from the Murchison Widefield Array (MWA) at 189 MHz with 15.6' resolution was presented by Bernardi et al. (2013). Observations with the Low Frequency Array (LOFAR) around 150 MHz added new information of polarized synchrotron emission at low frequencies with higher angular resolution. The power spectrum of interstellar turbulence was studied in the Fan region ($l = 137.0^\circ$; $b = +7.0^\circ$) by Iacobelli et al. (2013). Jelić et al. (2014; 2015) showed the ability of LOFAR to unravel regions with low RM that show a wide range of morphological features, e.g. straight filaments parallel to the Galactic plane that are correlated with cold filamentary structures in neutral hydrogen (Kalberla & Kerp 2016; Kalberla et al. 2017). Two remarkable polarized features extending over several degrees were assigned to almost neutral gas clouds in the local interstellar medium that are visible only in low-frequency polarization due to their small Faraday rotation and depolarization (Van Eck et al. 2017).

3.2.3 The Galactic Center

The Galactic Center is a unique source with unusual radio continuum features. Mapping of the Galactic Center region by Yusef-Zadeh et al. (1984) showed several features vertical to the plane. The radio continuum emission is most intense and has a flat spectral index (Reich et al. 1988), often accounted to thermal emission. However, this intense emission is highly polarized (e.g. Seiradakis et al. 1985) and was interpreted to be due to mono-energetic electrons (Lesch et al. 1988). The polarization “strings” imply vertical magnetic structures, much different from the azimuthal directions of the magnetic fields seen along the Galactic plane.

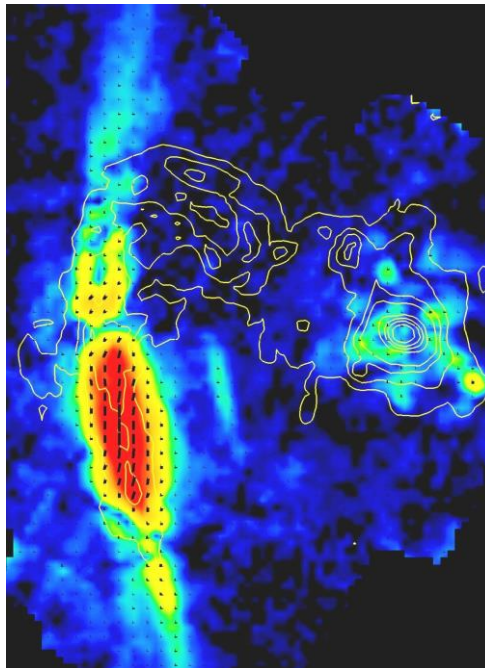


Fig. 12: Galactic Center region. Total intensity (contours), polarized intensity (colours) and B-vectors at 32 GHz, observed with the Effelsberg telescope. The map size is about 23' x 31' along Galactic longitude and latitude. The Galactic Center is located at the peak of total emission (from Wolfgang Reich, MPIfR).

Mapping of the Galactic Center at 32 GHz (Reich 2003; Fig. 12) showed that RMs in excess of ± 1600 rad m^{-2} are present in the vertical filaments. Based on Zeeman splitting observations of OH masers (e.g. Yusef-Zadeh et al. 1996), magnetic field strengths are very high (2 – 4 mG), while other authors (e.g. Crocker et al. 2010) suggested lower values of 50 – 100 μG , based on the radio synchrotron spectrum.

Detailed high-resolution studies also brought controversial results. High-resolution radio maps of the Galactic Center (e.g. Nord et al. 2004) showed a spiral structure at the position of Sgr A* and thin vertical radio continuum “strings”. Polarimetric observations at sub-mm wavelengths suggest a stretched magnetic field (Novak et al. 2000), as expected in sheared clouds, while the large-scale ordered field is mostly toroidal (Novak et al. 2003). Near-IR polarimetry suggests a smooth transition from toroidal to poloidal field configuration in the Galactic Center at $|b| \approx 0.4^\circ$ (Nishiyama et al. 2010).

A recent interpretation of the magnetic field phenomena in the Galactic Center was given by Ferrière (2009). If our Galaxy does not differ much from nearby galaxies, the vertical field detected close to the center is a local phenomenon. The high magnetic field strength that was implied from early studies (e.g. Seiradakis et al. 1985) has been confirmed by observations of large RMs towards pulsars located very close to the Galactic Center (Eatough et al. 2013; Schnitzeler et al. 2016). The line-of-sight magnetic field components of $\approx 16 - 33$ μG , combined with model predictions for the strength of the magnetic field in the GC, imply that the large-scale magnetic field has a small inclination angle with respect to the plane of the sky.

3.3 Faraday Rotation of extragalactic radio sources and pulsars

Faraday rotation (FR) is a powerful tool for studying magnetic fields. First, ionospheric rotation, later Faraday effects due to the Galactic ISM were detected soon after the discovery of linear polarization of the Galactic radio waves. At first the FR of diffuse emission was studied. Later with increasing samples of EGRS modelling of the magnetic field was attempted. Finally pulsars, most of which are concentrated to the Galactic plane were used to model the Galactic magnetic fields.

3.3.1 Extragalactic radio sources (EGRS)

Faraday rotation measures (RMs) towards polarized EGRS originate in the source itself and in the magneto-ionic media in the foreground (intergalactic space, intervening galaxies, Milky Way, interplanetary space, and ionosphere of the Earth). The contributions from intergalactic space, intervening galaxies, and interplanetary space are generally small. The contribution from the ionosphere of the Earth is also small and can be subtracted with help of a network of calibration sources with known polarization angles, leaving the RM from the Milky Way and the intrinsic RM. Interestingly, the intrinsic RM dispersion of extragalactic sources is smaller than the RM dispersion in the Galactic foreground for sightlines that are separated by at least 1° , so that the contribution by the Galactic foreground becomes important at low and intermediate Galactic latitudes (Schnitzeler 2010).

Here a word of caution should be given. The intrinsic polarization and RM of any EGRS may originate in the nucleus of a radio galaxy or in the extended lobes. Hence, when making observations at various frequencies to obtain the correct RM, care must be taken that the same source structure is measured. In particular there are problems in combining data from single dish observations with those of an interferometer at other frequencies. More recent observations use many adjacent frequency channels to accurately determine the RM, if a sufficiently wide band is used (*RM Synthesis*, section 2.4). This also helps to separate the intrinsic RM from that in the foreground. If RM Synthesis is not available, averaging over a large number of RMs is used to statistically reduce the intrinsic contributions.

The earliest catalogues of RMs towards EGRS were collected by Simard-Normandin & Kronberg (1980) showing the all-sky distribution of RMs. In this compendium of sources there were only a few sources with measured RMs along the Galactic plane, where the Galactic magnetic fields are concentrated, as was seen in the all-sky continuum surveys. Hence the interpretation of this data gave us an indication of a local magnetic field only. In recent years additional data on the RM of sources in the Galactic plane were obtained (Brown et al. 2003; 2007; Van Eck et al. 2011). However, all these surveys cover only partially the Galactic plane, so that interpretations were difficult. The highest observed values were $|RM| \approx 1000$ rad m^{-2} towards the Galactic Center. Similarly high $|RM|$ values

were determined by Roy et al. (2008) who surveyed an area directly at the center of our Galaxy. The RMs of EGRS in the very center of the Galaxy are mainly positive RMs, suggesting a magnetic field aligned with a central bar.

A statistical method to visualize the RM distribution over the sky was developed by Johnston-Hollitt et al. (2003) who used 800 sources. This work showed several areas of consistent RM values (of the same sign) as well as structures above and below the plane. A major extension of the data set was achieved by Taylor et al. (2009) who reanalyzed the NRAO VLA Sky Survey (NVSS). This study involved 37543 sources and added a huge number of new RMs, but is limited by the rather close frequency separation of the two frequency bands which leads to large RM errors and RM ambiguities, especially near the Galactic plane. The averaged RM towards extragalactic sources reveal the same sign above the plane and below the plane between Galactic longitudes -160° and -120° (Fig. 13, right) and also between $+110^\circ$ and $+150^\circ$ (Fig. 13, left): The local disk field seems to be part of a large-scale symmetric field structure. However, towards the inner Galaxy (between about -90° and $+90^\circ$ longitude) the signs of RM are opposite above and below the plane, indicating a field reversal. This reversal may be due to local features (Wolleben et al. 2010b) or to an antisymmetric toroidal field in the Milky Way's halo (section 3.5).

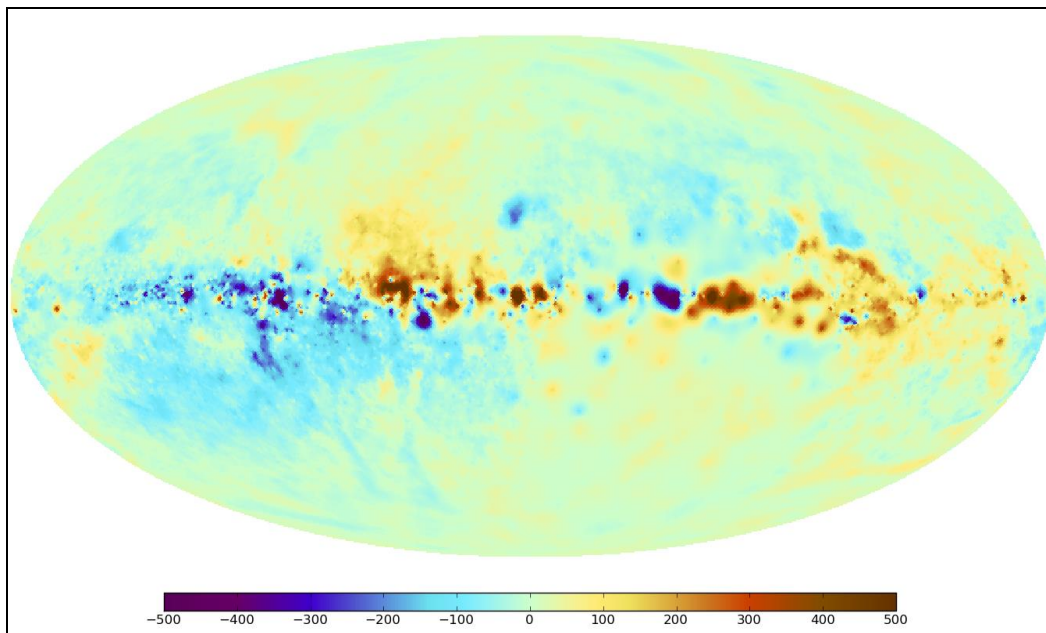


Fig. 13: All-sky map of rotation measures in the Milky Way, constructed from the RM data of about 40000 polarized extragalactic sources from the VLA NVSS survey and from other catalogs. Red: positive RMs, blue: negative RMs (Oppermann et al. 2012). Galactic longitude 0° (Galactic center) is in the map center. Galactic longitude increases from right to left, latitude increases from bottom to top.

Another project to increase the number of RMs over the whole sky was undertaken at the Effelsberg radio telescope. The combination of polarization data in 8 channels in two bands around 1.4 and 1.6 GHz enables an accurate determination of the RMs of the polarized sources. Some 1600 new RMs were added and a preliminary result was given in Wielebinski et al. (2008). The data for 2469 sources were used to model the Galactic magnetic field (Sun et al. 2008; section 3.5).

A recent update by Xu & Han (2014) reassessed the accuracy of published RMs and compiled a reliable catalogue. The coverage of the southern sky is still very spare and needs additional observations. A survey of compact sources in the southern hemisphere was carried out with the Australia Telescope Compact Array and will provide reliable Faraday depth spectra for over 3000 sightlines (Schnitzeler et al., in prep.). These sightlines will fill the gap below declination -40° that is not covered by the RM catalogue from Taylor et al. (2009), and for the first time we will have a complete and well-sampled view of the entire Milky Way and its halo.

3.3.2 Pulsars

In principle, pulsars are the ideal sources to probe the magnetic fields through the Faraday effect. Pulsars have no measurable angular structure and are highly polarized. However, pulsars with accurately measured distances are still rare. Pulsars are Galactic objects and hence their distribution is close to the Galactic plane towards the inner Galaxy. In fact very few pulsars are known towards the anti-center of the Galaxy. Hence a combination of pulsars and EGRS is optimal for studies of the Galactic magnetic field. Pulsars also allow measurement of the Dispersion Measure (DM) which follows from the signal delay occurring in the foreground medium. Together with the RM the value of the average regular magnetic field in the line of sight can be deduced (assuming that fluctuations in electron density and magnetic field strength are uncorrelated, see section 2.4):

$$\langle B_{\parallel} \rangle = 1.232 \frac{\text{RM}}{\text{DM}} \mu\text{G}$$

Application gives an average strength of the regular field in the local spiral arm of $1.4 \pm 0.2 \mu\text{G}$. In the inner Norma arm, the average strength of the regular field is $4.4 \pm 0.9 \mu\text{G}$. However, this estimate is only valid if variations in the regular strength and in electron density are *not correlated*. If they are correlated, the above formula gives an overestimate of $\langle B_{\parallel} \rangle$ and an underestimate for anti-correlated variations (Beck et al. 2003). 3D MHD simulations of incompressible turbulence revealed only a weak correlation for a Mach number of 2 and no correlation for smaller Mach numbers (Wu et al. 2015). However, compressible turbulence and larger Mach numbers have not yet been investigated.

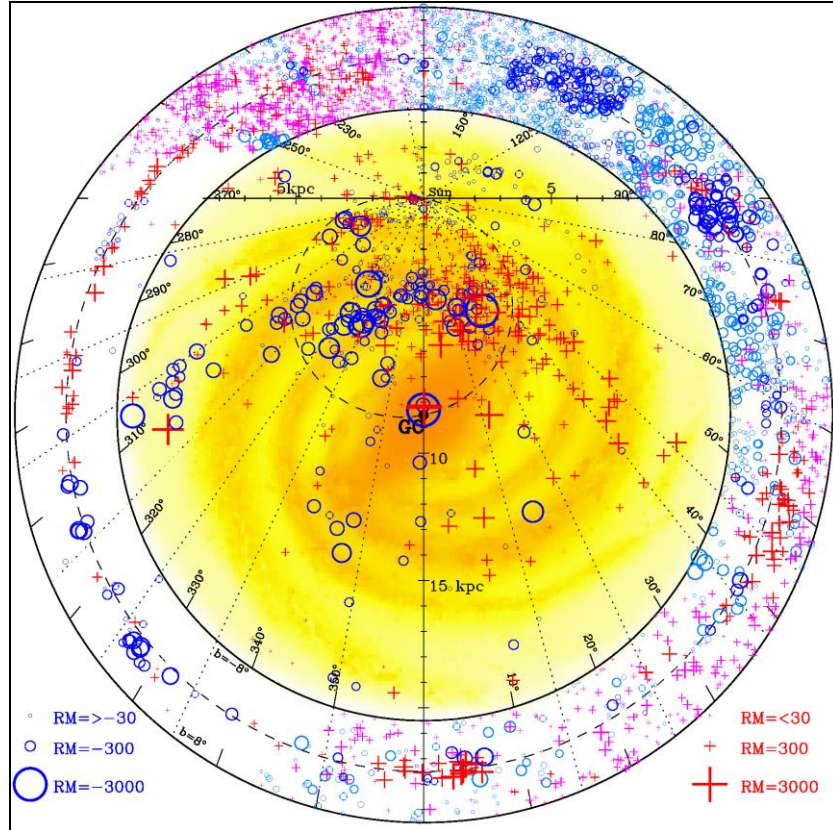


Fig. 14: Faraday rotation measures (RM) towards pulsars in the Milky Way at latitudes $|b| < 8^\circ$ (within the inner circle) and towards extragalactic radio sources at latitudes $|b| < 8^\circ$ (between the inner and outer circles). Red plus signs indicate positive RMs towards pulsars, blue circles negative RM. Pink and light blue symbols indicate RMs towards extragalactic sources compiled by Taylor et al. (2009); dark red and dark blue symbols are from the compilation of Xu & Han (2014). Our Sun is located at the crossing of coordinate lines. The dashed circle gives the locus of tangent points, assuming a spiral pitch angle of 11° . The background image is an artist's impression of the Galactic structure (Han et al. 2018).

The major compilation of pulsar rotation measures, also using already published data, are given in Han et al. (2006; 2009; 2018), additional results in Mitra (2003), Noutsos et al. (2008), and Van Eck et al. (2011). RMs with much lower uncertainties will soon become available from pulsars observed at low frequencies with LOFAR and MWA (Sobey et al. 2017).

The distribution of rotation measures, as given by Han (2018), shows a huge variation of signs and magnitudes (Fig. 14). This indicates a large-scale regular magnetic field with multiple reversals (section 3.5) or many local field distortions, e.g. by HII regions (Mitra et al. 2003; Nota & Katgert 2010).

RMs increase for distant objects, but very few pulsars were found beyond the Galactic Center (Fig. 14). The limit of $|RM| \approx 1000 \text{ rad m}^{-2}$ for EGRS holds also for pulsars. This seems to indicate that the RMs towards EGRS are partly averaged out in passage through the Galaxy. The large-scale regular field of the outer Milky Way is either weak or frequently reversing its direction. As distances to most pulsars are uncertain, this result should be taken with some caution. A larger sample of pulsar RM data and improved distance measurements to pulsars are needed.

3.4 Zeeman effect

The Zeeman effect is the most direct method of measuring magnetic fields. It has been used in the optical range for detecting magnetic fields in the Sun and in stars. At radio wavelength the use of the Zeeman effect proved to be more difficult. For one, the frequency shifts caused by the weak magnetic fields are minute and require sophisticated instrumentation. The HI line gave the first definitive detections, usually in absorption towards strong Galactic sources (Verschuur 1968). The technique was refined so that at present magnetic fields as weak as $\approx 5 \mu\text{G}$ can be detected with the Arecibo telescopes (Heiles & Crutcher 2005). The observation of the Zeeman effect in the OH molecule (e.g. Crutcher et al. 1987) advanced the field further. Even stronger fields ($\approx 80 \text{ mG}$) were detected in interstellar H_2O masers (Fiebig & Güsten 1989). Millimeter-wavelength astronomy gave us additional results for high recombination lines (Thum & Morris 1999) and in such molecules as CN (Crutcher et al. 1999) or CCS (Levin et al. 2000).

A compilation of present-day Zeeman measurements of the magnetic field in HI gas clouds gives a mean total field in the cold neutral interstellar gas of $6 \pm 2 \mu\text{G}$, so that the magnetic field dominates thermal motion, but is in equipartition with turbulence, as also found on much larger scales in external galaxies (section 4.2). Beyond cloud densities of $\approx 1000 \text{ cm}^{-3}$ the field strength scales with $n^{0.65 \pm 0.05}$ (Crutcher et al. 2010).

The importance of magnetic fields in the star-formation process is obvious. Diffuse clouds are subcritical with respect to collapse and probably balanced by magnetic fields, while dense molecular clouds are supercritical and collapse. The transition from subcritical to supercritical state may be the result of ambipolar diffusion or turbulence. Zeeman observations in the HI and OH lines can measure the ratio of mass to magnetic flux in the cloud envelope and the core. A smaller ratio in the core may indicate that supersonic turbulence plays a similarly important role as ambipolar diffusion (Crutcher et al. 2009), but effects of the field geometry also have to be taken into account (Mouschovias & Tassis 2009). More and higher-quality data are needed.

The use of the Zeeman data for the investigation of a large-scale regular magnetic field of the Galaxy was attempted by several authors (e.g. Fish et al. 2003). The number of detected sources was rather small and the interpretation in terms of Galactic magnetic fields rather inconclusive. Han & Zhang (2007) collected a large data set of Zeeman results and studied the question if the magnetic fields in molecular clouds preserve information of the direction of the large-scale magnetic fields in the spiral arms. In spite of a larger data set all that the conclusion offered was that clouds “may still remember the directions of regular magnetic fields in the Galactic ISM to some extent”.

3.5 Modelling the magnetic field of the Milky Way

Based on all the data described in previous sections models of the magnetic fields of the Milky Way have been repeatedly made. At first the low frequency all-sky data was used to describe the Galactic non-thermal emission (e.g. Yates 1968) produced in magnetic fields. The all-sky survey of Haslam et al. (1982) has been interpreted by Phillips et al. (1981) and Beuermann et al. (1985). Using the data

on the HII regions (e.g. Georgelin & Georgelin 1976) of the Galaxy it could be shown that the spiral structure is also seen in the diffuse total intensity radio emission.

The RM data first for pulsars and later for extragalactic radio sources (EGRS) led to more detailed modelling of the magnetic fields of the Milky Way. Pulsars are concentrated in the direction of the inner Galaxy; only few pulsars are known outside the inner quadrants. The data on EGRS gave information about the Faraday effects over much of the sky and in particular in the inner Galactic plane.

The collection of 543 rotation measures of EGRS distributed across the sky by Simard-Normandin & Kronberg (1980) showed that there were areas with similar RM directions, suggesting organized magnetic fields in the Galactic disk over large scales. Pulsar observers (e.g. Han & Qiao 1994) were the first to point out that in addition to large areas of similar magnetic field directions there were some regions where the field *reverses* along Galactic radius. These results were analyzed with wavelets (e.g. Stepanov et al. 2002) and confirmed the existence of at least one large-scale reversal. Since most of the EGRS investigated were away from the Galactic plane they did not trace the large-scale Galactic magnetic field in the disk, but more likely some local magnetic features. The number of RMs has been steadily increasing (e.g. Taylor et al. 2009) which increased the sampling of the Galaxy considerably. The same general conclusions were reached as in the earlier work – organized magnetic structures in sections of the Galaxy and highly disorganized magnetic fields towards the central region.

The analysis of data from radio continuum all-sky surveys at 1.4 and 23 GHz, from RMs towards EGRS, the best available thermal electron model and an assumed cosmic ray distribution (Sun et al. 2008; Sun & Reich 2010; Jaffe et al. 2010; Jansson & Farrar 2012a; 2012b; Ordog et al. 2017) constrained the average field strength of the Galaxy to $\approx 1 - 2 \mu\text{G}$ for the regular field and $\approx 3 - 5 \mu\text{G}$ for the random field in the solar neighborhood, similar to the results from pulsar RMs (section 3.3.2). An axisymmetric spiral (ASS) magnetic field configuration (section 2.6) with a pitch angle of $\approx 12^\circ$ fits the observed data best which is much smaller than the pitch angle of $\approx 30^\circ$ derived from the data of polarized emission only (Fauvet et al. 2011). This demonstrates the problems of the models to obtain a reliable estimate for the pitch angle.

Including the polarized thermal dust emission from WMAP at 94 GHz complicates the analysis (Jaffe et al. 2013). The magnetic fields in the dust-emitting regions seem to be more ordered than those in the synchrotron-emitting regions. The isotropic random component peaks in the gaseous arms, while the ordered fields are shifted, similar to the observations in external galaxies (section 4.4.1).

The local field is oriented parallel to the plane and its direction is symmetric (even symmetry) with respect to the Galactic plane, while the toroidal component of the halo field may have different directions above and below the Galactic plane (odd symmetry, see section 2.6), to account for the different signs of the observed RMs. If this antisymmetry is globally valid for the Milky Way, its halo field has a dipolar pattern, in contrast to that found in external galaxies (section 4.7). However, some of the asymmetry can be explained by distorted field lines around a local HI bubble (Wolleben et al. 2010b). Observations with better sampling of the sky are needed (section 5).

Near-infrared starlight polarization data around $l = 150^\circ$ are inconsistent with an odd-symmetry disk field and are better compatible with an even-symmetry axisymmetric spiral field with a pitch angle of about 6° (Pavel et al. 2012), smaller than that of the radio data.

Pulsars are promising objects to deduce the Galactic magnetic field because their RMs provide field directions at many distances from the Sun, but more accurate distances are needed. Since most pulsars are concentrated along the Galactic plane, they sample the field in the disk. Analysis of the pulsar and EGRS data led to several attempts to model the Galactic magnetic field (Brown et al. 2007; Van Eck et al. 2011; Han et al. 2018).

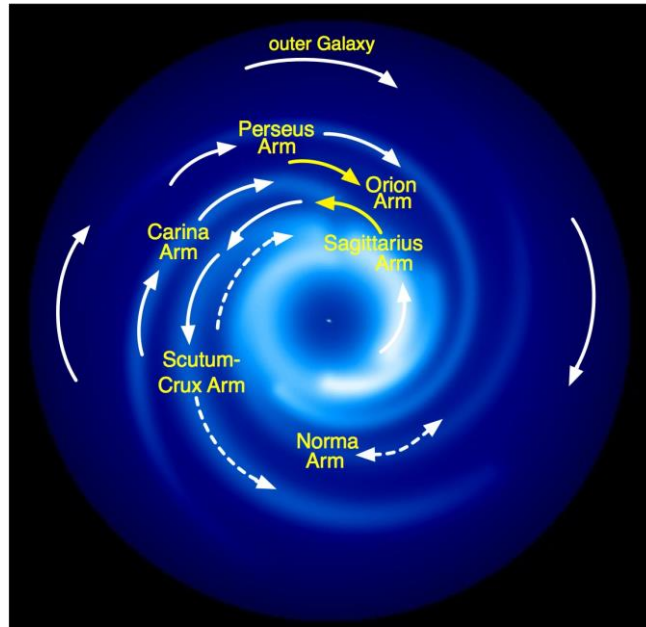


Fig. 15: Model of the large-scale magnetic field in the Milky Way's disk, derived from Faraday rotation measures of pulsars and extragalactic sources. Yellow arrows indicate confirmed results, while white and dashed arrows still need confirmation (from Jo-Anne Brown, Calgary).

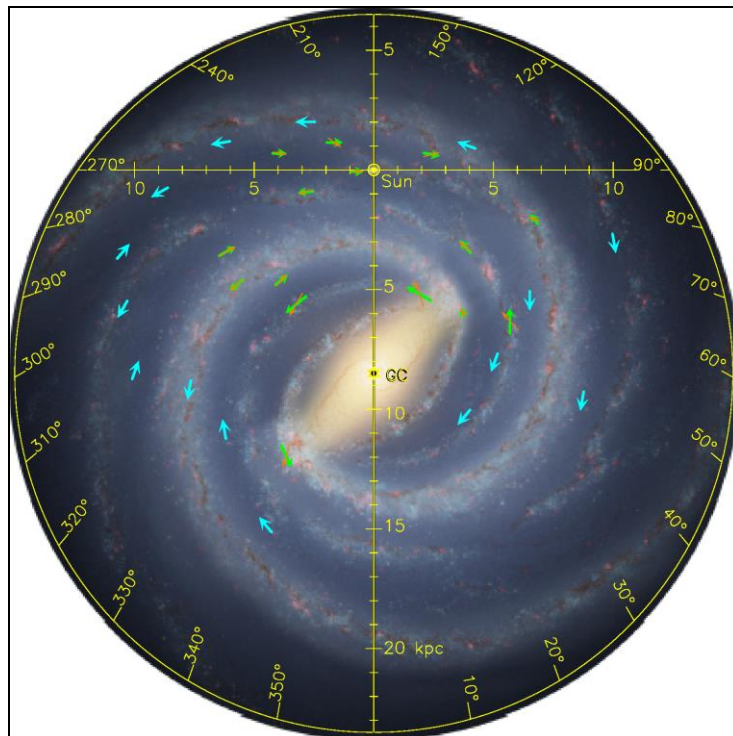


Fig. 16: Alternative model of the large-scale magnetic field in the Milky Way's disk, derived from Faraday rotation measures of pulsars and extragalactic sources. The orange arrows give the derived line-of-sight magnetic field components and the green arrows show the inferred spiral field. The blue arrows give the inferred spiral field direction derived from the comparison of RMs for EGRS with RMs for distant pulsars and are placed at the distance of the central axis of the next outer spiral feature (arm or interarm). The background image shows an artist's impression of the structure of our Galaxy (Han et al. 2018).

A large-scale magnetic field reversal is present between the clockwise directions of the local Carina-Orion arm (and the outer Perseus arm) and the counter-clockwise direction of the inner Scutum-Crux-Sagittarius arm (Fig. 15), located at about 1 – 2 kpc inside the solar radius. Comparison of rotation measures of pulsars in the disk at different distances as well as with rotation measures of background radio sources beyond the disk reveals between six and eight large-scale reversals of the field directions between spiral arms and interarm regions (Han et al. 2018; Fig. 16).

The reversals were often used as an argument in favor of a bisymmetric spiral (BSS) field structure, but a detailed analysis (e.g. Vallée 1996; Noutsos et al. 2008) showed that the concept of a single large-scale field mode is not compatible with the data. The analysis of the previous interpretations by Men et al. (2008) gave no proof of either a BSS or an ASS configuration, so that the large-scale field structure must be more complicated.

Studies of the effects of large HII regions on the RMs of pulsars beyond these Faraday screens showed that some of the claimed field reversals are only local (Mitra et al. 2003). Furthermore, the comparison of the RMs of pulsar and EGRS towards the Galactic Center (Brown et al. 2007) revealed similar values of RM, as if there were no other half of the Galaxy. This result suggests that the RMs are dominated by local ISM features and that the large-scale field is weak and cannot be delineated from the available data. Only RM data free from the effects of HII regions should be used, as was demonstrated by Nota & Katgert (2010).

Field reversals can emerge in MHD simulations of galaxies with an imposed spiral potential (Dobbs et al. 2016) and could be associated with velocity changes across the spiral shock of at least 20 km/s. Such signatures should be searched for in the velocity fields of interstellar gas.

The magnetic field structure in the disk of the Milky Way is probably quite complex and shows details that cannot be resolved yet in external spiral galaxies. The existence of one large-scale field reversal in the Milky Way is puzzling. Very few large-scale reversals have been detected so far in external spiral galaxies, and none along the radial direction (section 4.4.2). The different observational methods may be responsible for this discrepancy between Galactic and extragalactic results. RMs in external galaxies are averages over the line of sight through the whole disk and halo and over a large volume traced by the telescope beam, and they may miss field reversals, e.g. if these are restricted to a thin region near to the galaxy plane. The results in the Milky Way are mostly based on RMs of pulsars which trace the magneto-ionic medium near the plane. Alternatively, the Milky Way may be “magnetically young” and may still not have generated a coherent large-scale field over the whole disk. The timescale for fully coherent fields can be longer than the galaxy age, e.g. if frequent interactions with other galaxies occur (section 2.6). Another model to explain reversals is the continuous generation of small-scale fields; these may disturb the action of the α - Ω dynamo and allow reversals of the initial field to persist (Moss et al. 2012).

Little is known about the large-scale field in the Milky Way’s *halo*. In the Galactic Center vertical magnetic fields apparently extend into the halo (section 3.2.3). From a survey of RMs of EGRS towards the Galactic poles, Mao et al. (2010) derived a local large-scale field perpendicular to the plane of $+0.31 \pm 0.03 \mu\text{G}$ towards the south Galactic pole, but no significant field towards the north Galactic pole. This is neither consistent with an odd-symmetry halo field as suggested from the antisymmetry of the toroidal field nor with an even-symmetry halo field as found in several external galaxies (section 4.7).

Jansson & Farrar (2012a; 2012b), modelling the diffuse polarized emission and RMs, found evidence for X-shaped vertical field components, similar to those in external galaxies. A vertical halo field is also needed to explain the shape of a sample of shell-type axisymmetric supernova remnants expanding into the ambient field (West et al. 2016). A visualization of the Jansson & Farrar model is shown in Fig. 17.

Terral & Ferrière (2017) compared synthetic all-sky RM maps derived from their analytical models with the observed RMs of EGRS and found a preference for a bisymmetric halo field that can generate an X-shaped pattern. However, the halo field is probably more complicated than predicted by α - Ω dynamo models.

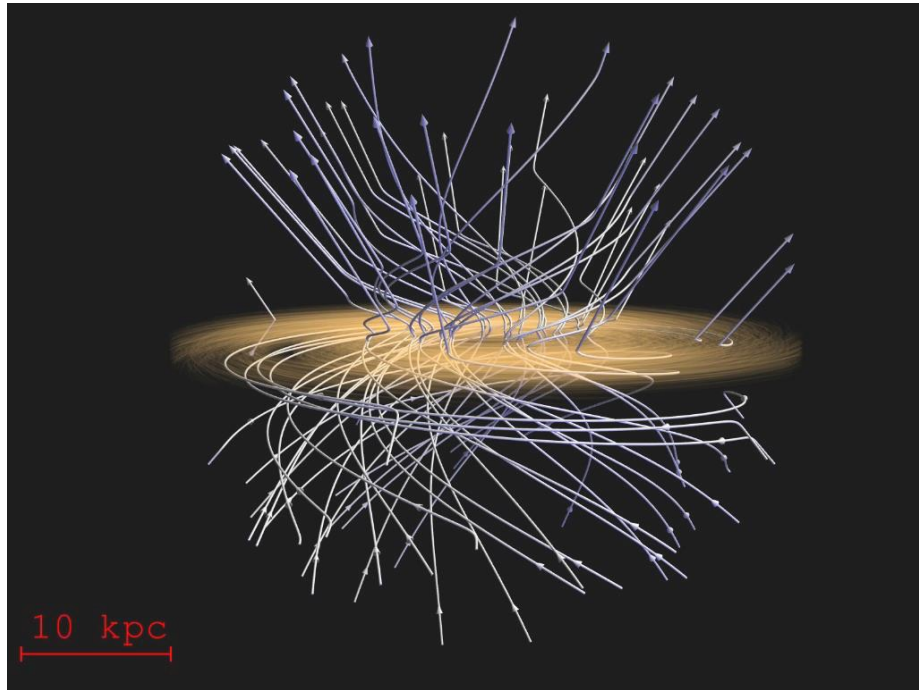


Fig. 17: Model of the outward-spiraling halo field of the Milky Way (Farrar 2016). This visualization was produced by T. Sandstrom, NASA.

While observations in the Milky Way can trace magnetic structures to much smaller scales than in external galaxies, the large-scale field is much more difficult to measure in the Milky Way. This information gap will be closed with help of future radio telescopes (section 5). Many new pulsars, together with improved distance measurements, and a large extension of the EGRS data base, especially in the southern hemisphere, will allow us to observe the detailed magnetic field structure in the Milky Way (Haverkorn et al. 2015). Next-generation modelling of the Galactic magnetic field can take advantage of IMAGINE, a software package based on Bayesian sampling (Steininger et al. 2018).

A table summarizing the various models of magnetic field configurations in the Milky Way is given in Haverkorn (2015).

4. Galaxies

Magnetic fields in external galaxies can be observed with the same methods as in the Milky Way, except for extragalactic pulsars which have been found so far only in the Magellanic clouds. Naturally the spatial resolution of the telescopes is much worse in galaxies, and the detailed structure of extragalactic fields on scales below about 100 pc is still invisible. On the other hand, the large-scale field properties, like the overall pattern and the total extent, can best be measured in external galaxies. Hence, observations in the Milky Way and in external galaxies are complementary.

4.1 Optical polarization, infrared polarization, and Zeeman effect

Weak linear polarization (generally below 1%) is the result of extinction by elongated dust grains in the line of sight which are aligned in the interstellar magnetic field (the Davis-Greenstein effect, see section 2.1). Optical polarization surveys yielded the large-scale structure of the field in the local spiral arm of our Milky Way (section 3.1). The first extragalactic results by Hiltner (1958), based on starlight polarization of globular clusters in M31, revealed a magnetic field aligned along the galaxy's major axis. Polarization of starlight in the LMC gave evidence for ordered fields near 30 Dor (Mathewson & Ford 1970b), along the Magellanic Bridge (Schmidt 1976). From a polarimetric catalog of 7207 stars, Gomes et al. (2015) found an ordered field aligned with SMC's bar with a strength of about $0.9 \mu\text{G}$.

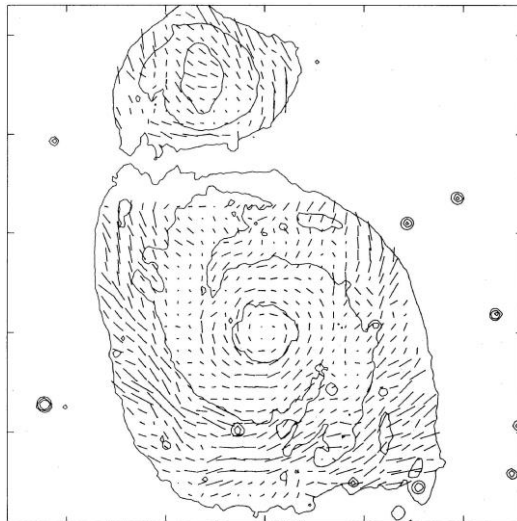


Fig. 18: Spiral galaxy M51. E-vectors of the optical polarization of diffuse light, tracing the magnetic field orientations (Scarrott et al. 1987). Compare with the radio polarization map in Fig. 23.

Polarization from diffuse optical light was used to search for large-scale magnetic fields, though some unknown fraction of the polarized light could be due to scattering on dust particles. A survey of 70 nearby galaxies revealed degrees of polarization of $\leq 1\%$ (Jones et al. 2012). Indications for ordered fields along the spiral arms were found in M82 (Elvius 1962), M51 and M81 (Appenzeller 1967; Scarrott et al. 1987), in NGC1068 (Scarrott et al. 1991), and in NGC6946 (Fendt et al. 1998). The pattern in M51 (Fig. 18) agrees well with the radio polarization results (see Fig. 23) in the inner spiral arms, but large differences are seen in the outer arms and in the companion galaxy that is unpolarized in the radio image. In the Sa-type edge-on Sombrero galaxy M104 and the Sb-type edge-on NGC4545, optical polarization indicated a field along the prominent dust lane and vertical fields above the plane (Scarrott et al. 1990), in agreement with the results from radio polarization (section 4.7). The polarization of the Sc-type edge-on galaxies NGC891, NGC5907, and NGC7331 indicated magnetic fields that are predominantly oriented perpendicular to the plane (Fendt et al. 1996), possibly aligned along the vertical dust filaments observed in these galaxies. On the other hand, near-infrared polarimetry of NGC891 revealed magnetic fields almost aligned with the plane (Montgomery & Clemens 2014), similar to the radio data (Fig. 41). Radio continuum polarization traces the magnetic fields in the diffuse medium which are mostly oriented parallel to the plane in the inner disk and have significant vertical components only beyond some height above the plane (section 4.7).

Correction of the diffuse optical polarization for scattering effects is difficult and has not been attempted so far. Instead, polarization techniques were developed in the infrared range where scattering is negligible. Near-IR polarization in the edge-on galaxies NGC891 and NGC4565 indicate plane-parallel fields (Montgomery & Clemens 2014; Jones 1989), similar to that seen at radio wavelengths. In the far-IR and sub-mm ranges, the degrees of polarization can reach several %. The galaxy M82 was observed at 850 μm (Greaves et al. 2000), but the derived bubble-type field pattern is in contrast to the radio data indicating a field that is oriented radially outwards (Reuter et al. 1992; Adebahr et al. 2017), while near-IR polarimetry shows a vertical field (Jones 2000). Differences between IR, sub-mm, and radio polarization data should be investigated with the polarimeters at the JCMT, APEX, ALMA, and SOFIA telescopes.

Zeeman measurements in external galaxies are still very rare. Field strengths of 6 – 28 mG were detected in 14 distant starburst galaxies by the Zeeman effect in the OH megamaser emission line at 1667 MHz (McBride & Heiles 2013). However, these values refer to highly compressed gas clouds and are not typical for the interstellar medium. HI Zeeman measurements in nearby galaxies will become possible with the Square Kilometre Array (section 5).

4.2 Magnetic field strengths

The dynamical importance of the total magnetic field B may be estimated by its energy density that is proportional to B^2 . Due to its vector nature, the dynamical effect of the magnetic field also depends on its structure and degree of ordering (section 4.4). The average strength of the component B_{\perp} of the total field and $B_{\text{ord},\perp}$ of the resolved ordered field in the plane of the sky can be derived from the total and polarized radio synchrotron intensity, respectively, if energy-density equipartition between total cosmic rays and total magnetic field B is valid (section 2.2). The field strengths B_{\perp} are given by the mean surface brightness (intensities) of synchrotron emission, hence do not depend on the distance to the galaxy.

The observed radio emission from galaxies has a contribution of thermal emission from ionized gas (and at frequencies beyond about 50 GHz also from dust) which needs to be subtracted to obtain the pure synchrotron part. The mean thermal fraction is about 10% at 21 cm and about 30% at 3 cm, but may increase to $\geq 50\%$ in star-forming regions. A proper subtraction of the radio thermal intensity needs an independent thermal template, e.g. the H α intensity corrected for extinction with help of a dust model based on far-infrared data (Tabatabaei et al. 2007) or of the ratio of hydrogen recombination lines. For a crude separation of thermal and synchrotron intensity components, comparison of the observed radio spectral index with an assumed synchrotron spectral index is sufficient.

The average equipartition strength of the total fields (corrected for inclination) for a sample of 74 spiral galaxies is $B = 9 \pm 2 \mu\text{G}$ (Niklas 1995). The average strength of 21 bright galaxies observed since 2000 is $B = 17 \pm 3 \mu\text{G}$ (Fletcher 2010). Dwarf galaxies host fields of similar strength as spirals if their star-formation rate per volume is similarly high. Blue compact dwarf galaxies are radio bright with equipartition field strengths of 10 – 20 μG (Klein et al. 1991). Spirals with moderate star-forming activity and moderate radio surface brightness like M31 (Fig. 26) and M33 (Fig. 36), our Milky Way's neighbors, have $B \approx 6 \mu\text{G}$. In "grand-design" galaxies with massive star formation like M51 (Fig. 23), M83 (Fig. 24) and NGC6946 (Fig. 25), $B \approx 15 \mu\text{G}$ is a typical average strength of the total field.

In the density-wave spiral arms of M51 the total field strength B is 25 – 30 μG (Fig. 19). Field compression by external forces like interaction with other galaxies may amplify the fields (section 4.8). The strongest fields in spiral galaxies (50 – 300 μG) are found in starburst galaxies like M82 (Adebahr et al. 2013; 2017; Lacki & Beck 2013), the "Antennae" NGC4038/9 (Fig. 44), in nuclear starburst regions, like in the nuclear ring of NGC1097 (Fig. 35), and in nuclear jets (Fig. 49).

If energy losses of cosmic-ray electrons are significant in starburst regions or massive spiral arms, the equipartition values are lower limits (section 2.2). The average equipartition field strength in normal spirals is proportional to the average gas surface density, but this relation is no longer valid for starburst galaxies (Thompson et al. 2006). Due to strong energy losses of the cosmic-ray electrons and even protons, the equipartition field strength is probably underestimated by a factor of a few.

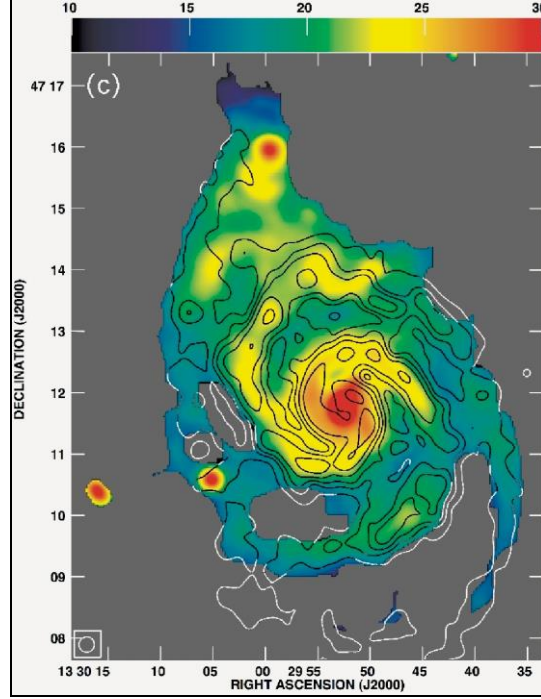


Fig. 19: Spiral galaxy M51. Total equipartition magnetic field strengths (in μG), corrected for the inclination of the galaxy (Fletcher et al. 2011).

The relative importance of various competing forces in the interstellar medium can be estimated by comparing the corresponding energy densities. In the local Milky Way, the energy densities of the stellar radiation field, turbulent gas motions, cosmic rays and total magnetic fields are similar (Boulares & Cox 1990). The mean energy densities of the total magnetic field and of the cosmic rays are $\approx 10^{-11}$ erg cm^{-3} in NGC6946 (Beck 2007), M63, M83, NGC4736 (Basu & Roy 2013), and IC342 (Beck 2015), and $\approx 10^{-12}$ erg cm^{-3} in M33 (Tabatabaei et al. 2008), in all cases similar to that of the kinetic energy of the cold, neutral gas with density ρ across the star-forming disk (Fig. 20), as predicted by dynamo models (section 2.6). The kinetic energy may be underestimated if v_{turb} is larger than 7 km/s. On the other hand, the turbulent velocity tends to decrease with radius (Tamburro et al. 2009) which would enhance the ratio of magnetic to kinetic energy.

The energy density of the warm ionized gas E_{th} with electron density n_e is one order of magnitude smaller than that of the total magnetic field E_B which means that the ISM in spiral galaxies is a *low- β plasma* ($\beta = E_{\text{th}}/E_B$), similar to that of the Milky Way (Boulares & Cox 1990). The energy density of hot gas in the ISM, neglected in Fig. 20, is similar or somewhat larger than that of warm gas, depending on its volume filling factor (Ferrière 2001), so that its inclusion would not change the above result significantly. The dominance of turbulent energy over thermal energy (supersonic turbulence) was also derived from numerical ISM simulations (de Avillez & Breitschwerdt 2005).

The radial distribution of synchrotron intensity in many spiral galaxies can be well described by an exponential decrease with a scalelength l_{syn} of about 4 kpc. In case of equipartition between the energy densities of magnetic fields and cosmic rays, the scalelength of the total field is $(3 - \alpha) l_{\text{syn}} \approx 15$ kpc (where $\alpha \approx -0.8$ is the synchrotron spectral index). The scalelength of the ordered field is even larger (Fig. 20). These are still lower limits because energy losses of cosmic-ray electrons increase with increasing distance from their origin in the galaxy's star-forming regions, and a lower density of cosmic-ray electrons needs a stronger field to explain the observed synchrotron intensity. Fields in the outer disk of galaxies can be amplified by the α - Ω dynamo (Mikhailov et al. 2014), even without star-formation activity because turbulence can be generated by the magneto-rotational instability (MRI, section 2.6). The typical scalelengths of the density of neutral and ionized gas are only about 3 kpc, so that the magnetic field energy dominates over the turbulent energy in the outer region of galaxies if a constant turbulent velocity is assumed (Fig. 20). The speculation that magnetic fields may affect the global gas rotation (Battaner & Florido 2000; Ruiz-Granados et al. 2010; Elstner et al. 2014) needs testing by future radio observations with higher sensitivity.

In spiral arms of galaxies the typical degree of radio polarization is only a few %. The total field B_{\perp} in the spiral arms is mostly *isotropic turbulent* with random orientations within the telescope beam that typically corresponds to a few 100 pc at the distance of nearby galaxies. The typical ratios of isotropic turbulent fields to resolved ordered fields are ≥ 5 in spiral arms and circum-nuclear starburst regions, 0.5 – 2 in interarm regions and 1 – 3 in radio halos. Turbulent fields in spiral arms are probably generated by turbulent gas motions due to supernovae (de Avillez & Breitschwerdt 2005) or by spiral shocks (Dobbs & Price 2008), driving a small-scale dynamo (section 2.6).

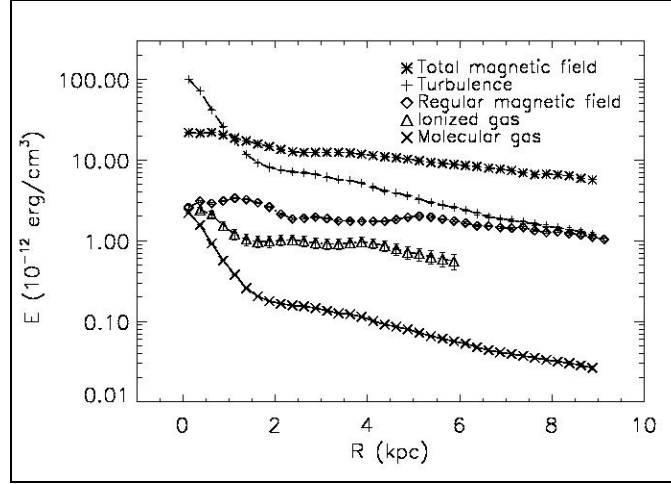


Fig. 20: Spiral galaxy NGC6946. Radial variation of the energy densities of the total magnetic field E_B ($B^2/8\pi$), the ordered (mostly regular) magnetic field ($B_{\text{reg}}^2/8\pi$), the turbulent motion of the neutral gas E_{turb} ($0.5 \rho_n v_{\text{turb}}^2$, where $v_{\text{turb}} \approx 7$ km/s), the thermal energy of the ionized gas E_{th} ($1.5 n_e k T_e$) and the thermal energy of the neutral molecular gas E_n ($1.5 \rho_n k T_n$), determined from observations of synchrotron and thermal radio continuum, and the CO and HI line emissions (Beck 2007).

Magnetic turbulence occurs over a large spectrum of scales. The maximum scale of the turbulence spectrum in the Milky Way derived from the dispersion of rotation measures of pulsars is $d \approx 50$ pc (Rand & Kulkarni 1989). This scale can also be estimated from beam depolarization by the superposition of emission from turbulent fields at centimeter wavelengths (section 2.3): For a typical degree of polarization of 3% in spiral arms, 500 pc resolution in nearby galaxies, and 1 kpc pathlength through the turbulent medium, $d \approx 70 \text{ pc } f^{1/3}$ where f is the filling factor of the magneto-ionic medium. At decimeter radio wavelengths the same turbulent field causes internal Faraday dispersion (section 2.4). Typically, $DP \approx 0.1$ at 20 cm ($\sigma_{\text{RM}} \approx 50 \text{ rad m}^{-2}$). An average electron density of the thermal gas of 0.03 cm^{-3} and an average strength of the turbulent field of $10 \mu\text{G}$ yields $d \approx 130 \text{ pc } f$. The two estimates agree for $d \approx 50$ pc and $f \approx 0.4$, consistent with the results derived with other methods.

Faraday dispersion can also be used to measure the strength of isotropic turbulent magnetic fields. However, the achievable accuracy is limited because the ionized gas density has to be determined from independent measurements. The increase of the mean degree of polarization at 1.4 GHz with increasing distance from the plane of edge-on galaxies can constrain the parameters and, for NGC891 and NGC4631, yields strengths of the isotropic turbulent magnetic fields in the plane of $11 \mu\text{G}$ and $7 \mu\text{G}$ and scale heights of 0.9 kpc and 1.3 kpc, respectively (Hummel et al. 1991).

The strength of the *resolved ordered* (regular and/or anisotropic turbulent) fields B_{ord} in spiral galaxies is determined from the total equipartition field strength and the degree of polarization of the synchrotron emission. Present-day observations with typical spatial resolutions of a few 100 pc give average values of 1 – 5 μG . B_{ord} is not correlated with global shear, as would be expected from the α - Ω dynamo, while almost linearly correlated with the rotational velocity (Tabatabaei et al. 2016), suggesting a coupling between B_{ord} and the dynamical mass of a galaxy.

The ordered field is generally strongest in the regions between the optical spiral arms with peaks of about $12 \mu\text{G}$, e.g. in NGC6946, is oriented parallel to the adjacent optical spiral arms and is stronger than the tangled field. In several galaxies like in NGC6946 the field forms coherent *magnetic arms*

between the optical arms (section 4.4.1). In galaxies with strong density waves some of the ordered field is concentrated at the inner edge of the spiral arms, e.g. in M51 (Fig. 23), but the arm-interarm contrast of the ordered field is small, much less than that of the isotropic turbulent field.

The strength of the *regular* (coherent) component of the ordered field can in principle be determined from Faraday rotation measures (section 2.4), if the mean electron density is known. In the Milky Way, the pulsar dispersion measure is a good measure of the total electron content along the pathlength to the pulsar. Only 19 extragalactic radio pulsars have been found so far, all in the LMC and SMC. In all other galaxies, the only source of information on electron densities of the warm ionized medium comes from thermal emission, e.g. in the H α line. However, thermal emission is dominated by the HII regions which have a small volume filling factor, while Faraday rotation is dominated by the diffuse ionized emission with a much larger filling factor. If the average electron density of the diffuse ionized medium in the Milky Way of $0.03 - 0.05 \text{ cm}^{-3}$ is assumed also for other galaxies, Faraday rotation measures yield regular field strengths of a few μG . The strongest regular field of $8 \mu\text{G}$ was found in NGC6946 (Beck 2007), similar to the strength of the ordered field, hence most of the ordered field is regular in this galaxy. The similarity between the average regular (RM-based) and the ordered (equipartition-based) field strengths in NGC6946 and several other galaxies demonstrates that both methods are reliable and hence no major deviations from equipartition occur in this galaxy on scales of a few kpc (though deviations may occur locally).

The situation is different in radio-bright galaxies like M51 and IC342, where the average regular field strength is several times smaller than the ordered field (section 4.4.2). The total field is strong, so that the energy loss of cosmic-ray electrons is high and the equipartition field is probably underestimated (section 2.2). This even increases the discrepancy between the two methods because RMs are not affected. The high-resolution observations of M51 indicate that anisotropic turbulent fields related to the strong density waves contribute mostly to the ordered field (section 4.4.1).

4.3 The radio – infrared correlation

The highest total radio intensity (mostly synchrotron emission, tracing the total, mostly turbulent field) generally coincides with the strongest emission from dust and gas in the spiral arms. The total radio and far-infrared or mid-IR intensities are highly correlated within galaxies. The radio-IR correlation also holds between the integrated luminosities of galaxies (e.g. Bell 2003; Basu et al. 2015b). It is one of the tightest correlations known in astronomy. The tightness needs multiple feedback mechanisms that are not yet fully understood (Lacki et al. 2010).

Synchrotron intensity depends on the density of cosmic-ray electrons that are accelerated in supernova remnants and diffuse into the interstellar medium, and on about the square of the strength of the total magnetic field (section 2.2). Infrared intensity (luminosity) between wavelengths of about $20 \mu\text{m}$ and $70 \mu\text{m}$ (emitted from warm dust particles in thermal equilibrium, heated mainly by UV photons) is a measure of the local (global) star-formation rate. Below about $20 \mu\text{m}$ wavelength, large PAH particles and stars contribute; emission beyond about $70 \mu\text{m}$ comes from cold dust that is heated by the general radiation field.

The exponent of the correlation is different in the spiral arms and the interarm regions (Dumas et al. 2011; Basu et al. 2012). Deviations from the correlation may occur in interacting galaxies, where the magnetic field is compressed by shear or shock fronts, and in galaxies with strong magnetic arms where B is enhanced in interarm regions with low star-formation rate (Tabatabaei et al. 2013a; section 4.4.1). The scale-dependent correlations (using wavelets) between the radio synchrotron and IR emissions are strong at large spatial scales, but break down below a scale of a few 100 pc which can be regarded as a measure of the electron diffusion length that seems to depend on the degree of field ordering (Tabatabaei et al. 2013b).

The radio synchrotron-IR correlation requires that magnetic fields and star-formation processes are connected somehow. In the “electron calorimeter” model, valid for starburst galaxies with strong fields where energy losses of the cosmic-ray electrons are strong, B^2 is assumed to increase with the infrared luminosity to obtain a linear radio-IR correlation (Lisenfeld et al. 1996). However, galaxies with low or medium star-formation rate (SFR) are no calorimeters because the cosmic-ray electrons can leave the galaxy and a combination of several processes with self-regulation is needed to explain the correlation within galaxies. If the dust is warm and optically thick to UV radiation, the IR intensity is

proportional to the local SFR. Then, a possible scenario is the coupling of magnetic fields to the gas clouds or equipartition between magnetic and kinetic energy densities ($B \sim \rho^a$, where ρ is the neutral gas density), the Schmidt-Kennicutt law of the star-formation rate ($\text{SFR} \sim \rho^b$) (Niklas & Beck 1997). Depending on the values of the exponents a and b , and whether or not equipartition between the energy densities of magnetic fields and cosmic rays is valid, a linear or nonlinear synchrotron-IR correlation is obtained (Dumas et al. 2011; Basu et al. 2012). Present data clearly favour a nonlinear relation (see Fig. 6 in Li et al. 2016).

In the non-calorimeter model, the synchrotron-IR correlation is interpreted as a correlation between the strength of the isotropic turbulent field and the star-formation rate (Fig. 21; Heesen et al. 2014) or the energy rate injected by supernovae (Li et al. 2016). The tightest relation in a sample of 55 dwarf and spiral galaxies is that between B and the star formation rate per galaxy area, with an exponent of 0.33 ± 0.03 (Chyży et al. 2017). This exponent is consistent with field amplification by the small-scale dynamo and an exponent of $4/3$ for the synchrotron-IR correlation in spiral galaxies (Schleicher & Beck 2016). In dwarf galaxies, star-formation is no longer steady, and the timescale for energy losses of CRE becomes shorter than the injection timescale, and the exponent of the correlation should steepen to about $5/3$, to be tested with future observations.

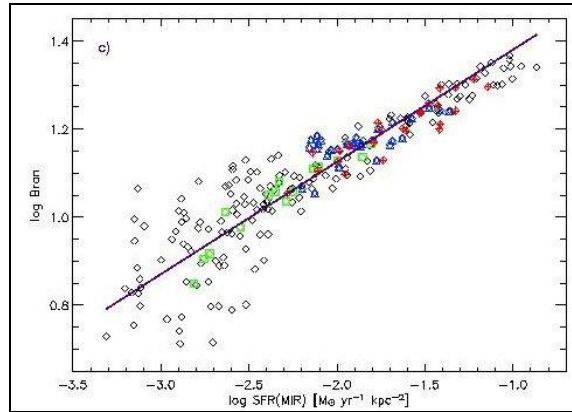


Fig. 21: Spiral galaxy NGC4254. Correlation between the strength of the isotropic turbulent field and the star-formation rate per area (determined from the $24 \mu\text{m}$ intensities) within the galaxy, plotted on logarithmic scales. The slope of the fitted line gives an exponent of 0.26 ± 0.01 (Chyży 2008).

The detection of strong radio emission in distant galaxies (which is at least partly of synchrotron origin) demonstrates that magnetic fields existed already in the early Universe. The correlation holds for starburst galaxies up to redshifts of at least 4 hosting fields of several $100 \mu\text{G}$ strengths (Murphy 2009). A steepening and finally a breakdown of the radio-IR correlation is expected when the inverse Compton losses of the cosmic-ray electrons interacting with CMB photons become stronger than the synchrotron losses; the redshift of this breakdown gives information about the field evolution in young galaxies (Schleicher & Beck 2013). Detailed predictions about the investigation of magnetic fields in young galaxies with present and future radio telescopes were given by Schober et al. (2016).

4.4 Magnetic field structures in spiral galaxies

4.4.1 Ordered fields

At wavelengths $\leq 6 \text{ cm}$, Faraday rotation of the polarized synchrotron emission is generally small (except in central regions), so that the B-vectors directly trace the orientations of the ordered field (which can be regular or anisotropic turbulent, see section 2.3). Spiral patterns were found in almost every galaxy, even in those lacking optical spiral structure like the ringed galaxy NGC4736 (Fig. 22) and flocculent galaxies, while irregular galaxies show at most some patches of spiral structure (sections 4.6 and A.2). Spiral fields are also observed in the nuclear starburst regions of barred galaxies (section 4.5). Galaxies of type Sa and S0 and elliptical galaxies without an active nucleus have little star formation and hence produce only few cosmic rays that could emit synchrotron emission (section 4.10).

The gas flow in “smooth” galaxies (no bar, no tidal interaction, no strong density wave) is almost circular, while the field lines are spiral. If large-scale magnetic fields were frozen into the gas, differential rotation would wind them up to very small pitch angles. The observed smooth spiral patterns with significant pitch angles ($10^\circ - 40^\circ$, see Fletcher 2010) indicate a general *decoupling* between magnetic fields and the gas flow due to magnetic diffusivity which is a strong indication for α - Ω dynamo action (section 2.6). There is presently no other model to explain the magnetic spiral patterns in the many types of galaxies.

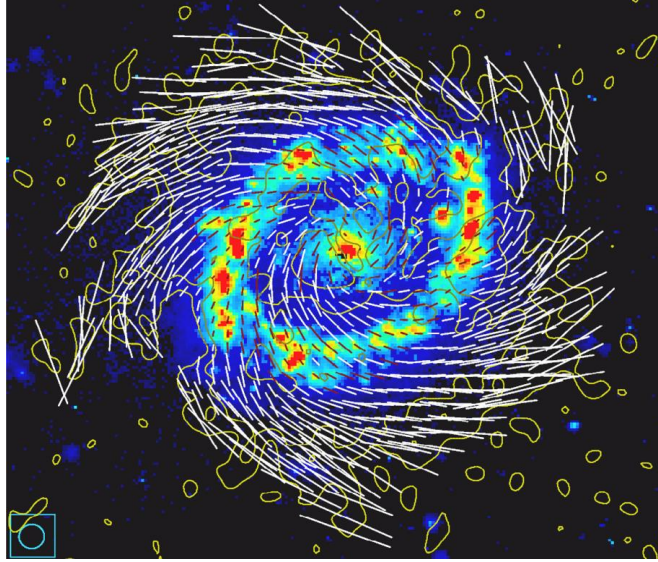


Fig. 22: Ring galaxy NGC4736. B-vectors of polarized radio intensity at 8.46 GHz (3.5 cm), observed with the VLA (Chyży & Buta 2008), trace the magnetic field orientations. The background $H\alpha$ image is from Johan Hendrik Knapen (Inst. Astr. de Canarias).

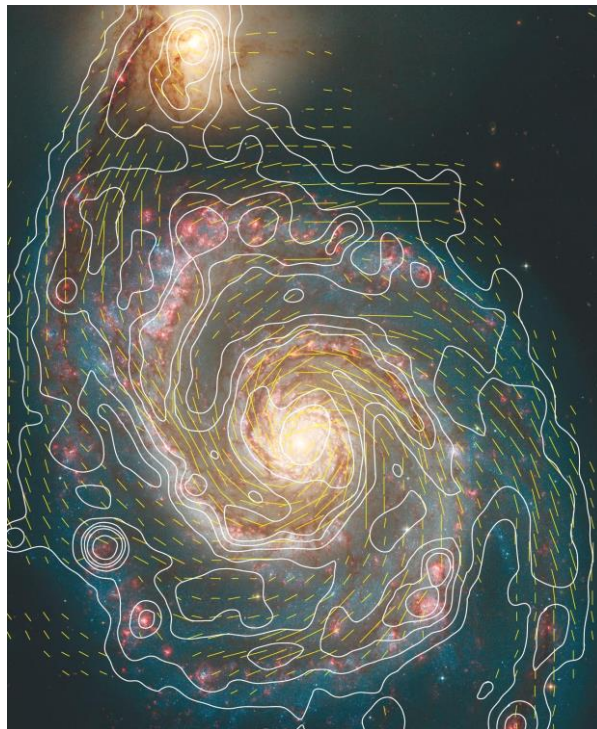


Fig. 23: Spiral galaxy M51. Total radio intensity (contours) and B-vectors at 4.86 GHz (6.2 cm), combined from observations with the VLA and Effelsberg 100-m telescopes (Fletcher et al. 2011). The background optical image is from the HST (Hubble Heritage Team). Graphics: Sterne und Weltraum.

However, the spiral pattern of magnetic fields cannot be solely the result of α - Ω dynamo action. In gas-rich galaxies with strong density waves, the magnetic spiral pattern generally follows the spiral pattern of the gas arms. In the prototypical density-wave galaxy M51, for example, the pitch angles of the magnetic lines are similar to those of the gaseous arms in the inner galaxy, but major deviations occur in the outer parts of the galaxy, where the tidal effects of the companion galaxy are strong (Patrikeev et al. 2006). In dynamo theory, the pitch angle of the magnetic lines depends on global parameters (Van Eck et al. 2015; Chamandy et al. 2016) and is difficult to adjust to the pitch angle of the spiral structure of the gas. In the outer parts of M51, ordered fields coincide with the outer spiral arms in the south and south-west; these are possibly tidal arms with strong shear. The field in the north-east deviates from the gas arm and points towards the companion, a signature of interaction.

If the beautiful spiral pattern of M51 seen in radio polarization (Fig. 23) were due to a regular field, it should be accompanied by a large-scale pattern in Faraday rotation which is not observed. This means that most of the ordered field is *anisotropic turbulent* and probably generated by compression and shear of the non-axisymmetric gas flow in the density-wave potential. From an analysis of dispersions of the radio polarization angles at 6.2 cm in M51, Houde et al. (2013) measured a ratio of the correlation lengths parallel and perpendicular to the local ordered magnetic field of 1.83 ± 0.13 . The anisotropic field is strongest at the positions of the prominent dust lanes on the inner edge of the inner gas spiral arms, due to compression of isotropic turbulent fields in the density-wave shock. Anisotropic fields also fill the interarm space, without signs of compression, probably generated by shearing flows. Regular fields also exist in M51, but are much weaker (section 4.4.2).

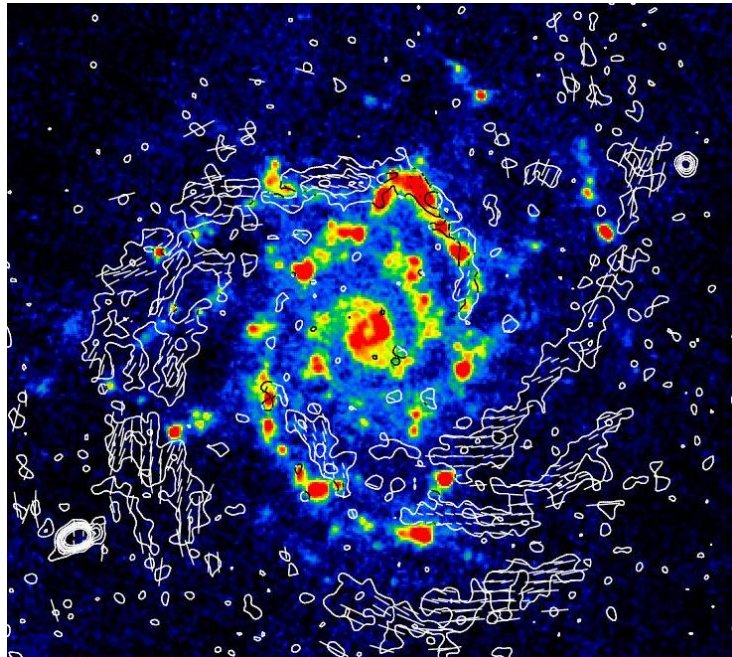


Fig. 24: Spiral galaxy M74. Polarized radio intensity (contours) and B-vectors at 3.1 GHz (9.7 cm), observed with the VLA (Mulcahy et al. 2017). The background infrared image at 70 μm is from the Herschel telescope.

M74 (Fig. 24), M83 (Frick et al. 2016), IC342 (Fig. 27), and NGC2997 (Han et al. 1999) are cases similar to M51, with enhanced ordered (anisotropic) fields at the inner edges of the inner optical arms, ordered fields in interarm regions and ordered fields coinciding with the outer optical arms. Density-wave galaxies with less star-formation activity, like M81 (Krause et al. 1989b) and NGC1566 (Ehle et al. 1996), show little signs of field compression and ordered fields occur mainly in the interarm regions.

A detailed analysis revealed that the magnetic pitch angles in several spiral galaxies (except M51) are systematically larger than the pitch angles of the gaseous spiral arms by about 20° in M83 (Frick et al. 2016), by about 8° in M101 (Berkhuisen et al. 2016), and by $12^\circ - 23^\circ$ in M74 (Mulcahy et al. 2017). This is evidence for the action of a large-scale dynamo where the magnetic field is not coupled to the gas flow and obtains a significant radial component. Magnetic fields are *dynamically active* in spirals.

Observations of another gas-rich spiral galaxy, NGC6946, revealed a surprisingly regular distribution of polarized emission with two symmetric *magnetic arms* located in interarm regions, with orientations parallel to the adjacent optical spiral arms and no signs of compression at the inner edge of the gas arms (Fig. 25). These are seen at several radio wavelengths (Williams et al. 2018) and hence cannot be due to weaker Faraday depolarization in the interarm regions. Their degree of polarization is exceptionally high (up to 50%); the field is almost totally ordered and mostly regular, as indicated by Faraday rotation measures. With the higher sensitivity achieved at 20 cm wavelength, more magnetic arms appear in the northern half of NGC6946, extending far beyond the optical arms, but located between outer HI arms. Magnetic arms have also been found in the western part of M74 (Fig. 24), the north-west of IC342 (Fig. 27), in NGC2997, and in several other gas-rich spiral galaxies. Magnetic arms can be explained in the framework of α - Ω dynamo models (see extended discussion in Beck 2016). Alternatively, magnetic reconnection in the interarm regions may contribute to the field ordering (Weżgowiec et al. 2016).

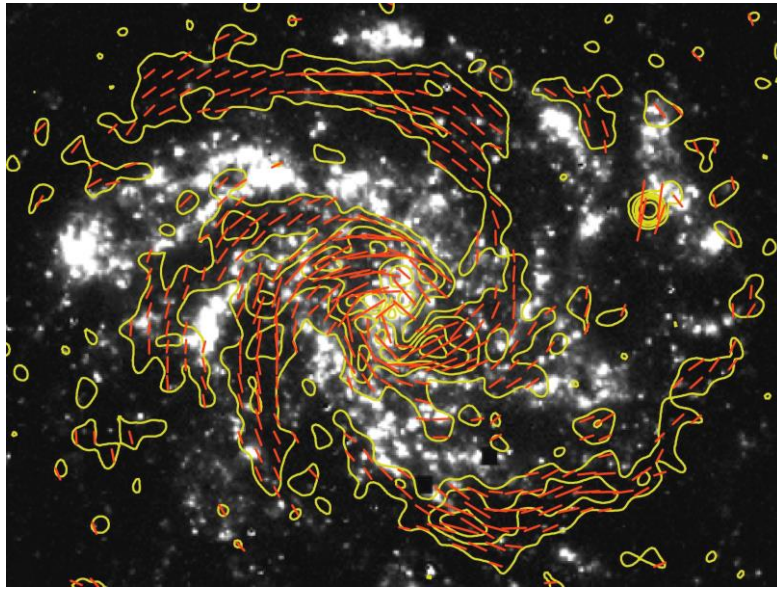


Fig. 25: Spiral galaxy NGC6946. Polarized radio intensity (contours) and B-vectors at 4.86 GHz (6.2 cm), combined from observations with the VLA and Effelsberg 100-m telescopes (Beck 2007). The background H α image is from Anne Ferguson. Graphics: Sterne und Weltraum.

Ordered magnetic fields may also form spiral features that are disconnected from the optical spiral pattern. Long, highly polarized filaments were discovered in the outer regions of IC342 where only faint arms of HI line emission exist (Krause et al. 1989a). Sensitive observations at 20 cm revealed a system of such features extending to large distances from the center (Beck 2015).

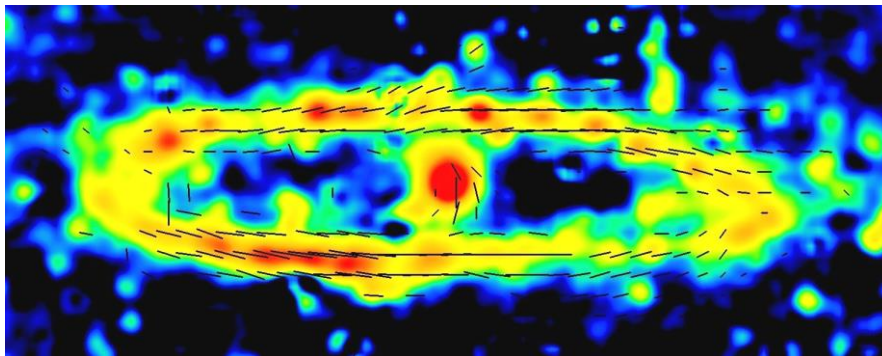


Fig. 26: Spiral galaxy M31. Total radio intensity (colours) and B-vectors (corrected for Faraday rotation) at 4.75 GHz (6.3 cm), observed with the Effelsberg telescope (Berkhuijsen et al. 2003).

In the highly inclined Andromeda galaxy, M31 (Fig. 26), the spiral arms are hard to distinguish due to the insufficient angular resolution. Star formation activity is concentrated to a limited radial range at around 10 kpc distance from the center (the “ring”). The ordered fields are strongest in the massive dust lanes where the degree of polarization is about 40%. The field follows the “ring” with a coherent direction (Fig. 29) and hence is regular.

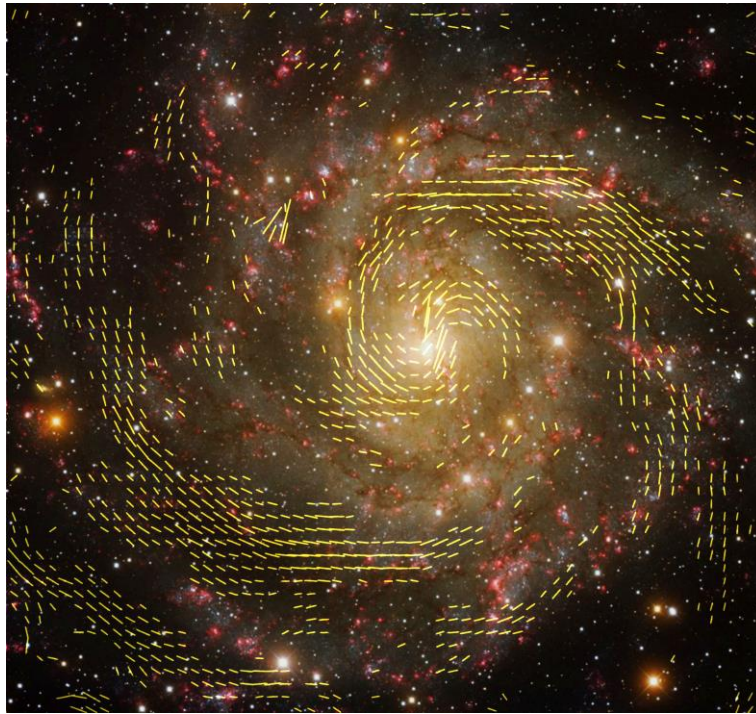


Fig. 27: Spiral galaxy IC342. Polarization B-vectors at 4.86 GHz (6.2 cm), combined from observations with the VLA and Effelsberg telescopes (Beck 2015). The background colour image is from the Kitt Peak Observatory (credit: T.A. Rector, University of Alaska Anchorage, and H. Schweiker, WIYN and NOAO/AURA/NSF). A region of $16' \times 16'$ (about 16×16 kpc) is shown.

The ordered magnetic field in the nearby spiral galaxy IC342 reveals several polarization spiral arms of different origins (Fig. 27). In contrast to NGC6946, there is only a rudimentary magnetic arm in an interarm region in the north-west, probably because of weaker dynamo action in IC342. A polarization narrow arm of about 300 pc width, displaced inwards with respect to the inner arm east of the central region, indicates that magnetic fields are compressed by a density wave, like in M51. A broad polarization arm of 300 – 500 pc width around the northern optical arm shows systematic variations in polarized emission, polarization angles and Faraday rotation measures on a scale of about 2 kpc, indicative of a helically twisted flux tube generated by the Parker instability. Several broad polarization arms in the outer galaxy are coincident with spiral arms in the total neutral gas.

At wavelengths of around 20 cm, a striking asymmetry of the polarized emission occurs along the major axis of all 12 spiral galaxies observed so far with sufficiently high sensitivity that have inclinations of less than about 60° . The emission is almost completely depolarized by Faraday dispersion on one side of the major axis that is always the kinematically *receding* one (positive radial velocities). In strongly inclined galaxies, both sides of the major axis become Faraday-depolarized at around 20 cm, as a result of the long pathlength. The asymmetry is still visible at 11 cm, but disappears at smaller wavelengths. This tells us that, in addition to spiral fields in the disk, regular fields in the halo are needed, as predicted by α - Ω dynamo models (Urbanik et al. 1997; Braun et al. 2010; section 4.7). The effect of such halo fields becomes prominent at 20 cm because most of the polarized emission from the disk is Faraday-depolarized (section 2.4).

At even longer wavelengths, Faraday effects depolarize the synchrotron emission almost completely. With help of RM Synthesis applied to 90 cm data, an extremely low average degree of polarization of 0.21 ± 0.05 % was measured in the star-forming “ring” of M31 (Gießübel et al. 2013).

4.4.2 Regular fields

Ordered magnetic fields as observed by polarized emission can be anisotropic turbulent or regular (section 2.3). *Faraday rotation measures* (RMs) are signatures of such regular fields. RM is determined from multi-wavelength radio polarization observations (section 2.4). Spiral dynamo modes (section 2.6) can be identified from the periodicity of the azimuthal variation of RMs in inclined galaxy disks (Fig. 28), where the RM can be determined from diffuse polarized emission (Krause 1990) or from RM data of polarized background sources (Stepanov et al. 2008). As several dynamo modes can be superimposed, Fourier analysis of the RM variation is needed. The resolution of present-day radio observations is sufficient to identify not more than 2 – 3 modes (Fletcher 2010). Spectro–polarimetric data of spiral galaxies are still rare and the application of RM Synthesis (section 2.4) has just started.

The disks of a few spiral galaxies reveal large-scale RM patterns giving strong evidence for modes generated by the α - Ω dynamo. M31 is the prototype of a dynamo-generated magnetic field (Fig. 29). The discovery became possible thanks to the large angular extent and the high inclination of M31. The polarized intensity at 6 cm is largest near the minor axis where the field component B_{\perp} is largest (Fig. 30a), while the maxima in $|RM|$ are observed near the major axis where the line-of-sight field component B_{\parallel} is strongest (Fig. 30b). This single-periodic RM variation is a signature of a dominating axisymmetric spiral (ASS) disk field (dynamo mode $m = 0$) (Fletcher et al. 2004) which extends to at least 25 kpc distance from the center when observed with an *RM grid* (see below) (Han et al. 1998).

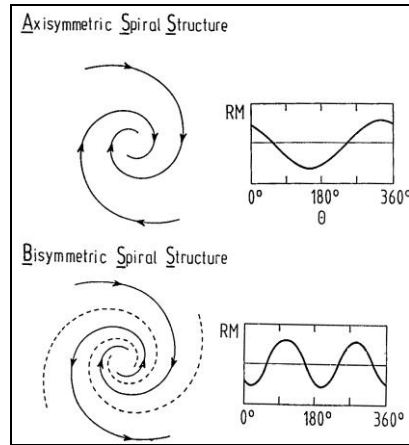


Fig. 28: Azimuthal RM variations (measured from the major axis) for axisymmetric spiral (ASS) and bisymmetric spiral (BSS) fields in inclined galaxies (Krause 1990).

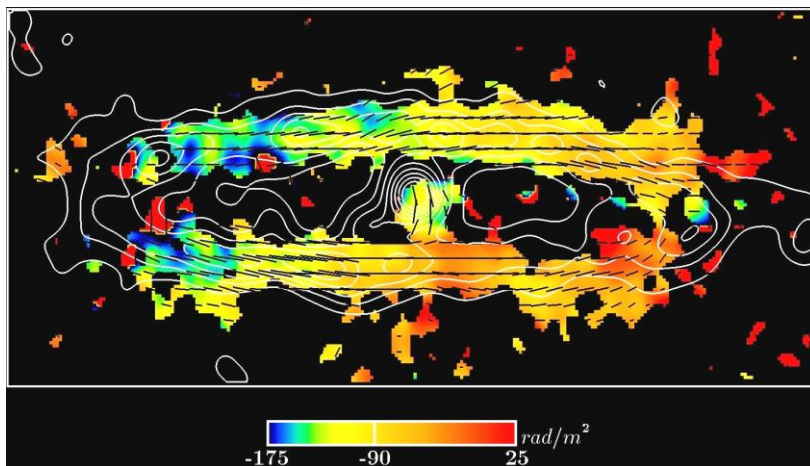


Fig. 29: Spiral galaxy M31. Total radio intensity at 4.75 GHz (6.3 cm) (contours), B -vectors and Faraday rotation measures between 4.75 GHz (6.3 cm) and 2.7 GHz (11.1 cm) (colours), derived from observations with the Effelsberg telescope (Berkhuijsen et al. 2003). The average rotation measure of about -90 rad m^{-2} is caused by the foreground medium in the Milky Way.

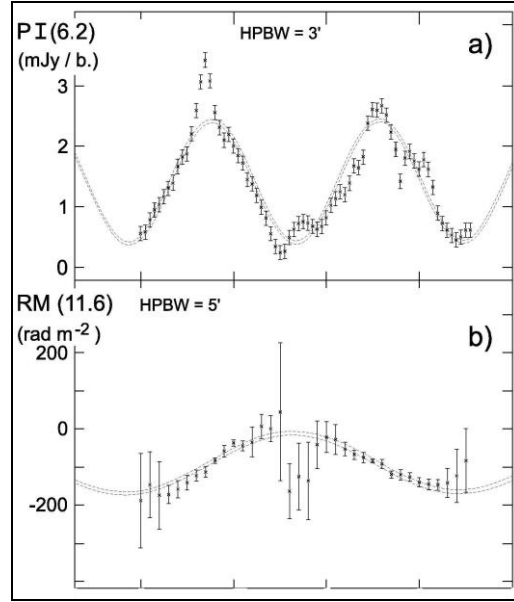


Fig. 30: Spiral galaxy M31. (a) Polarized intensity and (b) Faraday rotation measures between 4.75 GHz (6.3 cm) and 2.7 GHz (11.1 cm) along the azimuthal angle in the plane of the galaxy, counted counterclockwise from the northern major axis (left side in Fig. 29) (Berkhuijsen et al. 2003).

Other galaxies with a dominating ASS disk field are IC342, the Virgo galaxy NGC4254, the almost edge-on galaxies NGC253, NGC891 and NGC5775, the irregular Large Magellanic Cloud (LMC), and a few further candidates (see Appendix).

By measuring the signs of the RM distribution and the velocity field on both sides of a galaxy's major axis, the *inward* and *outward* directions of the radial component of the ASS field can be distinguished (Fig. 31). Dynamo models predict that both signs have the same probability, which is confirmed by observations. The ASS field of M31, IC342, NGC253, and the ASS field component in NGC6946 points inwards, while that of NGC4254, NGC5775, and the ASS component of the disk field in M51 points outwards.

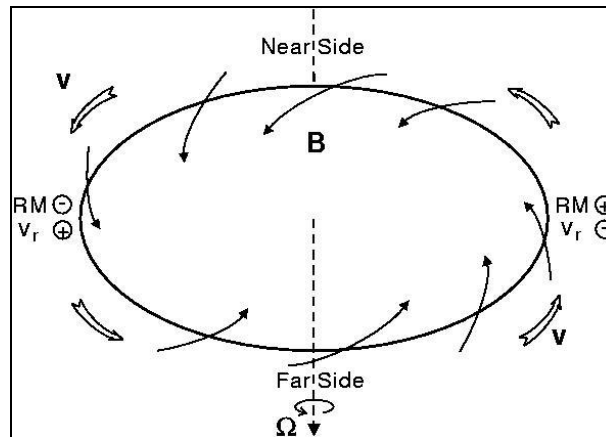


Fig. 31: The sign of the Faraday rotation measure (RM) and the sign of the rotation velocity component (v_r) along the line of sight, measured near the major axis of a galaxy, are opposite in the case of the inward direction of the radial component of an ASS-type field, while the signs are the same for the outward field direction. Trailing spirals are assumed (Krause & Beck 1998).

M81, M83, and an intervening galaxy at a redshift of 0.4 (Kronberg et al. 1992) are the only candidates so far for a bisymmetric spiral (BSS) field ($m = 1$), characterized by a double-periodic RM variation, but

the data quality is limited in all these cases. Dominating BSS fields are rare, as predicted by dynamo models. It was proposed that tidal interaction can excite the BSS mode, but no preference for BSS was found even in the most heavily interacting galaxies in the Virgo cluster (section 4.8). The idea that galactic fields are wound-up primordial intergalactic fields and hence are of BSS type (section 2.6) can also be excluded from the existing observations.

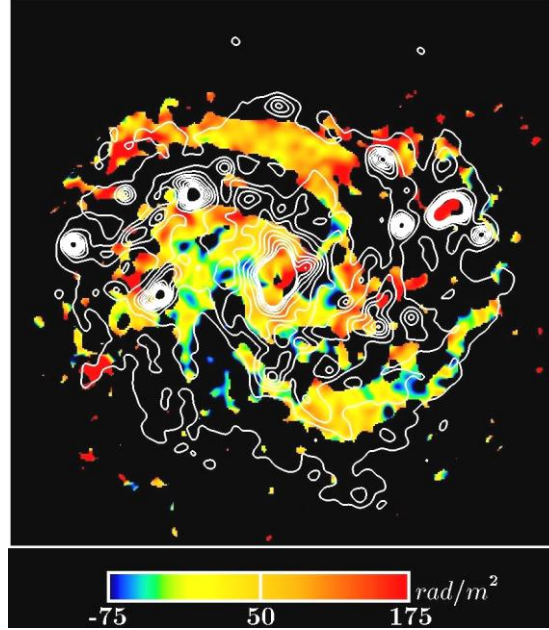


Fig. 32: Spiral galaxy NGC6946. Total radio intensity at 4.86 GHz (6.2 cm) (contours) and Faraday rotation measures between 8.46 GHz (3.5 cm) and 4.86 GHz (6.2 cm) (colours), derived from combined observations with the VLA and Effelsberg telescopes (Beck 2007). The average rotation measure of about $+50 \text{ rad m}^{-2}$ is caused by the foreground medium in the Milky Way.

Faraday rotation in NGC6946 (Fig. 32) and in other similar galaxies with magnetic arms can be described by a superposition of two azimuthal dynamo modes ($m = 0$ and $m = 2$) with about equal amplitudes, where the quadrisymmetric spiral (QSS) $m = 2$ mode is phase shifted with respect to the density wave (Beck 2007). This model is based on the RM pattern of NGC6946 that shows different field directions in the northern and southern magnetic arm (Fig. 32). A weaker QSS mode superimposed onto the dominating ASS mode is indicated in the disk of M51 and in the inner part of the ring of M31. A superposition of ASS and BSS modes can describe the fields of M33 and NGC4254, while three modes (ASS+BSS+QSS) are needed for several other galaxies (Fletcher 2010; update in Beck 2016; see also Appendix, Table 5).

In most galaxies observed so far, a spiral polarization pattern was found, but no large-scale RM pattern as a signature of regular fields. In many cases the available polarization data is insufficient to derive reliable RMs. In other cases the data quality is high, but no large-scale RM patterns are visible. In density-wave galaxies, strong compression and shearing flows generate *anisotropic* fields (with frequent reversals) of spiral shape which are much stronger than the underlying regular field, like in M51 (Fletcher et al. 2011) and in IC342 (Beck 2015). In galaxies without density waves, several dynamo modes may be superimposed, but cannot be distinguished with the limited sensitivity and resolution of present-day telescopes. Another explanation is that the timescale for the generation of large-scale modes is longer than the galaxy's lifetime, so that the regular field is not fully organized and still restricted to small regions.

Large-scale *field reversals* were discovered from pulsar RMs in the Milky Way (section 3.5), but nothing similar has yet been detected in spiral galaxies, although high-resolution RM maps of Faraday rotation are available for many spiral galaxies. In M81 the dominating BSS field implies two large-scale reversals (Krause et al. 1989b). The disk fields of several galaxies may be composed of a mixture of modes where reversals emerge in a limited radial and azimuthal range of the disk, like in NGC4414 (Soida et al. 2002). However, no reversals along the radial direction, like those in the Milky Way, were

found so far in the disk of any external galaxy. A satisfying explanation is still lacking (section 3.5). Reversals on smaller scales are probably frequent, but difficult to observe in external galaxies with the resolution of present-day telescopes. In the barred galaxy NGC7479, where a jet serves as a bright polarized background (Fig. 50), several reversals on 1 – 2 kpc scale were detected in the foreground disk of the galaxy (Laine & Beck 2008).

The central regions of M31 (Fig. 26) and IC342 (Fig. 27) host regular spiral fields that are disconnected from the disk fields (Gießübel & Beck 2014; Beck 2015). As the direction of the radial field component points outwards, *opposite* to that of the disk field, two separate dynamos seem to operate in these galaxies.

While the azimuthal symmetry of dynamo modes is known for many galaxies, the vertical symmetry (*even* or *odd*) is much harder to determine. The RM patterns of even and odd modes are similar in mildly inclined galaxies. The toroidal field of odd modes reverses its sign above and below the galactic plane (Fig. 6 top). Thus, in a mildly inclined odd field, half of the RM is observed compared to that in an even field which cannot be distinguished in view of the large RM variations caused by ionized gas density and field strength. The symmetry type becomes only visible in strongly inclined galaxies as a RM sign reversal above and below the plane. Only even-symmetry fields were found so far, in M31, NGC253, NGC891, and NGC5775 (section 4.7), in agreement with the prediction of dynamo models.

In summary, magnetic field structures in spiral galaxies are complex. The observations can best be explained as a superposition of dynamo-generated modes of regular fields coupled to the diffuse warm gas, plus anisotropic turbulent fields by shearing and compressing flows, plus isotropic turbulent fields coupled to the cold gas in spiral arms. The magnetic fields in barred galaxies behave similarly (section 4.5). For a more detailed model of the physics of the field-gas interaction, spectro-polarimetric data (RM Synthesis, section 2.4) and high resolution with future telescopes (section 5) are required.

4.5 Magnetic fields in barred galaxies

Gas and stars in the gravitational potential of strongly barred galaxies move in highly noncircular orbits. Numerical models show that gas streamlines are deflected in the bar region along shock fronts, behind which the cold gas is compressed in a fast shearing flow (Athanasoula 1992). The compression regions traced by massive dust lanes develop along the edge of the bar that is leading with respect to the galaxy's rotation because the gas rotates faster than the bar pattern. The warm, diffuse gas has a higher sound speed and is not compressed. According to simulations, the shearing flows around a bar should amplify magnetic fields and generate complicated field patterns changing with time (Otmianowska-Mazur et al. 2002). Field reversals may appear between the bar and the spiral arms (Kulpa-Dybeł et al. 2011). The asymmetric gas flow can also enhance dynamo action and excite the QSS ($m = 2$) mode (Moss et al. 2001).

20 galaxies with large bars were observed with the Very Large Array (VLA) and with the Australia Telescope Compact Array (ATCA) (Beck et al. 2002; 2005a). The total radio luminosity (a measure of the total magnetic field strength) is strongest in galaxies with high far-infrared luminosity (indicating high star-formation activity), a result similar to that in non-barred galaxies. The average radio intensity, radio luminosity and star-formation activity all correlate with the relative bar length. Polarized emission was detected in 17 of the 20 barred galaxies. The pattern of the ordered field in the galaxies with long bars (NGC1097, 1365, 1559, 1672, 2442, and 7552) is significantly different from that in non-barred galaxies: Field enhancements occur outside of the bar (upstream) and the field lines are oriented at large angles with respect to the bar.

NGC1097 (Fig. 33) is one of the nearest barred galaxies and hosts a huge bar of about 16 kpc length. The total radio intensity (not shown in the figure) and the polarized intensity are strongest in the downstream region of the dust lanes (southeast of the center). This can be explained by a compression of isotropic turbulent fields in the bar's shock, leading to strong and anisotropic turbulent fields in the downstream region. The surprising result is that the polarized intensity is also strong in the upstream region (south of the center in Fig. 33) where RM data indicate that the field is regular. The pattern of field lines in NGC1097 is similar to that of the gas streamlines as obtained in numerical simulations (Athanasoula 1992). This suggests that the ordered (partly regular) magnetic field is aligned with the flow and amplified by strong shear. Remarkably, the optical image of NGC1097 shows dust filaments in the upstream region, oriented almost perpendicular to the bar and aligned with

the ordered field. Between the region upstream of the southern bar and the downstream region the field lines smoothly change their orientation by almost 90° . The ordered field is probably coupled to the diffuse gas (having a larger sound speed) and thus avoids being shocked in the bar. The magnetic energy density in the upstream region is sufficiently high to affect the flow of the diffuse gas.

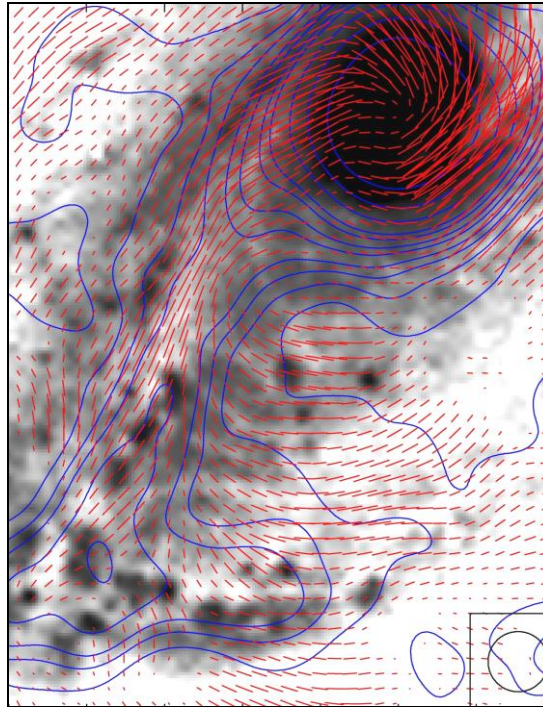


Fig. 33: Southern half of the barred galaxy NCC1097. Total radio intensity (contours) and B-vectors at 8.46 GHz (3.5 cm), observed with the VLA (Beck et al. 2005a). The background optical image is from Halton Arp (Cerro Tololo Observatory).

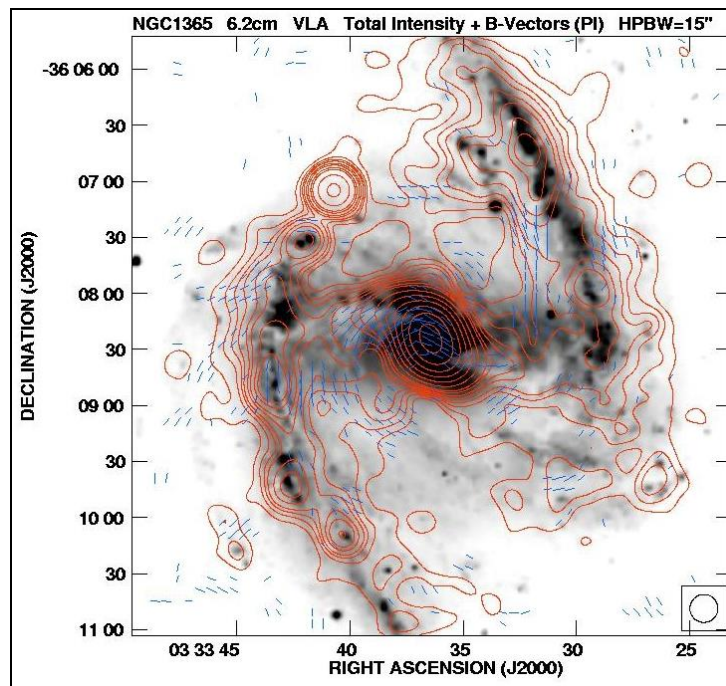


Fig. 34: Barred galaxy NGC1365. Total radio intensity (contours) and B-vector at 4.86 GHz (6.2 cm), observed with the VLA (Beck et al. 2005a). The background optical image is from Per Olof Lindblad (ESO).

NGC1365 (Fig. 34) is similar to NGC1097 in its overall properties, but the polarization data indicate that the shear is weaker. The ordered field bends more smoothly from the upstream region into the bar, again with no indication of a shock. M83 is the nearest barred galaxy, but with a short bar; it shows compressed ordered fields at the leading edges of the bar on both sides of the nucleus and some polarization in the upstream regions (Frick et al. 2016). In all other galaxies observed so far (section A.2) the resolution is insufficient to separate the bar and upstream regions.

The central regions of barred galaxies are often sites of ongoing intense star formation and strong magnetic fields that can affect the gas flow. Radio emission from ring-like regions was found in NGC1097, NGC1672, and NGC7552 (Beck et al. 2005b). NGC1097 hosts a bright ring with about 1.5 kpc diameter and an active nucleus in its center (Fig. 35). The ordered field in the ring has a spiral pattern and extends towards the nucleus. The orientation of the innermost spiral field agrees with that of the spiral dust filaments visible on optical images. Magnetic stress in the circum-nuclear ring can drive mass inflow at a rate of $dM/dt = -h/\Omega \langle b^2 \rangle + Br B\Phi$, where h is the scale height of the gas, Ω its angular rotation velocity, b the strength of the turbulent field and B that of the ordered field, and r and Φ denote the radial and azimuthal field components (Balbus & Hawley 1998). For NGC1097, $h \approx 100$ pc, $v \approx 450$ km/s at 1 kpc radius, $br \approx b\Phi \approx 50$ μ G gives an inflow rate of several solar masses per year which is sufficient to fuel the activity of the nucleus (Beck et al. 2005a). A similar inflow rate was determined for the central region of the starburst galaxy M82 (Adebahr et al. 2017).

In summary, the isotropic turbulent field in galaxies with massive bars is coupled to the cold gas and compressed in the bar's shock. The ordered field outside the bar region follows the general flow of the cold and warm gas, possibly due to shear, but decouples from the cold gas in front of the shock and goes with the diffuse warm gas. The polarization pattern in barred galaxies can be used a tracer of the flow of diffuse gas in the sky plane and hence complements spectroscopic measurements of radial velocities. Detailed comparisons between polarimetric and spectroscopic data are required, as well as MHD models including the back-reaction of the magnetic fields onto the gas flow.

Radio polarization data have revealed differences, but also similarities between the behaviours of ordered magnetic fields in barred and non-barred galaxies. In galaxies without bars and without strong density waves the field lines have a spiral shape, they do not follow the gas flow and are probably amplified by dynamo action. In galaxies with massive bars or strong density waves the field lines mostly follow the flow of the diffuse warm gas. Near the shock fronts galaxies with strong bars and with strong density waves (section 4.4) reveal a similar behaviour: Isotropic turbulent fields are coupled to the cold gas, are shocked and become anisotropic turbulent, while regular fields are coupled to the warm diffuse gas and hence avoid shock compression.

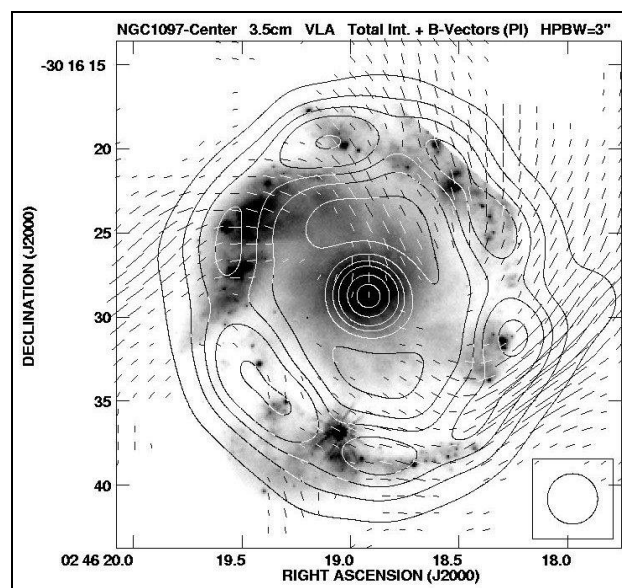


Fig. 35: Central star-forming ring of the barred galaxy NGC1097. Total radio intensity (contours) and B-vectors at 8.46 GHz (3.5 cm), observed with the VLA (Beck et al. 2005a). The background optical image is from the Hubble Space Telescope.

4.6 Flocculent and irregular galaxies

Flocculent galaxies have disks, but no prominent spiral arms. Nevertheless, spiral magnetic patterns are observed in all flocculent galaxies, indicative that the α - Ω dynamo works independently of density waves. The multi-wavelength data of M33 and NGC4414 call for a mixture of dynamo modes or an even more complicated field structure (Appendix, Table 5). Ordered magnetic fields with strengths similar to those in grand-design spiral galaxies have been detected in the flocculent galaxies M33 (Fig. 36), NGC3521, NGC5055, and NGC4414, and also the mean degree of polarization is similar between grand-design and flocculent galaxies (Knapik et al. 2000).

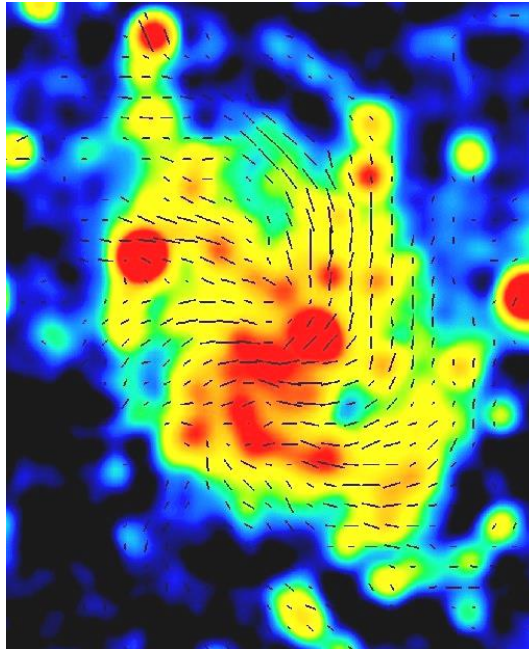


Fig. 36: Flocculent galaxy M33. Total radio intensity (colours) and B-vectors of the flocculent galaxy at 8.35 GHz (3.6 cm), observed with the Effelsberg telescope (Tabatabaei et al. 2008)

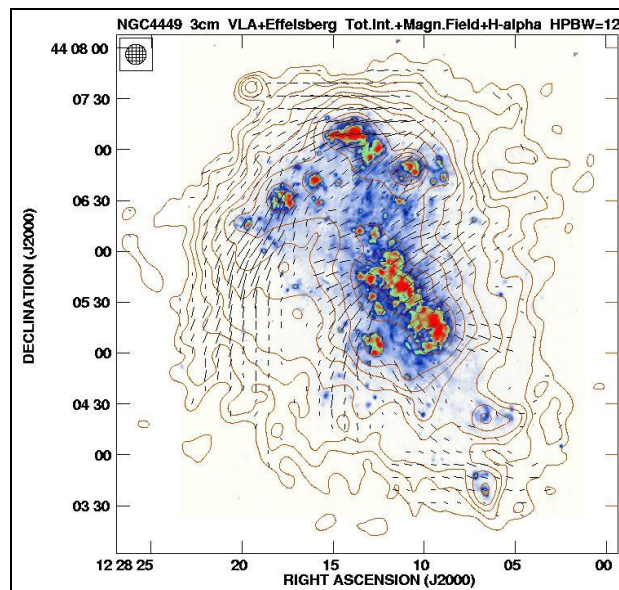


Fig. 37: Magellanic-type galaxy NGC4449. Total radio intensity (contours) and B-vectors at 8.46 GHz (3.5 cm), combined from VLA and Effelsberg observations (Chyży et al. 2000). The background image shows the $H\alpha$ emission.

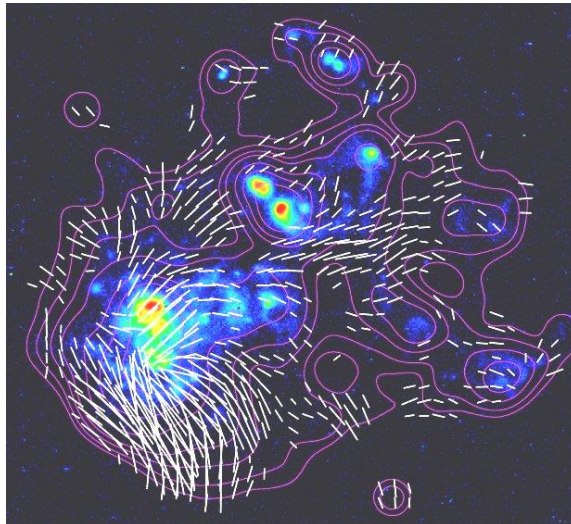


Fig. 38: Irregular galaxy IC10. Total radio intensity (contours) and B-vectors at 4.86 GHz (6.2 cm), observed with the VLA (from Chris Chyży, Kraków University). The background H α image is from Dominik Bomans (Bochum University).

Radio continuum maps of irregular, slowly rotating galaxies may reveal strong total equipartition magnetic fields, e.g. in the Magellanic-type galaxy NGC4449 (Fig. 37), IC10 (Fig. 38), and NGC2976. IC10 and NGC2976 are even able to drive galactic winds and inflate a huge radio halo with vertical magnetic fields (Chyży et al. 2016; Drzazga et al. 2016). In NGC4449 some fraction of the field is ordered with about 7 μ G strength and a spiral pattern. Faraday rotation shows that this ordered field is partly regular and the α - Ω dynamo is operating in this galaxy. The total field is of comparable strength (10 – 15 μ G) in starburst dwarfs like NGC1569 (Kepley et al. 2010) where star formation activity is sufficiently high for the operation of the small-scale dynamo (section 2.6). In these galaxies the energy density of the magnetic fields is only slightly smaller than that of the (chaotic) rotation of the gas and thus may affect the evolution of the whole system. The starburst dwarf galaxy NGC1569 shows polarized emission, but no large-scale regular field. In dwarf galaxies with very weak star-forming activity, no polarized emission is detected and the isotropic turbulent field strength is several times smaller than in spiral galaxies (Chyży et al. 2011), sometimes less than 5 μ G (Chyży et al. 2003). The latter value may indicate a sensitivity limit of present-day observations or a threshold for small-scale dynamo action.

The Magellanic Clouds are the closest irregular galaxies and deserve special attention. Polarization surveys with the Parkes single-dish telescope at several wavelengths had low angular resolution and revealed weak polarized emission. Two magnetic filaments were found in the LMC south of the 30 Dor star-formation complex (Klein et al. 1993). ATCA surveys of an RM grid towards background sources show that the LMC probably contains a large-scale magnetic field similar to large spirals (Gaensler et al. 2005) and that the field of the SMC is weak and uniformly directed away from us, possibly part of a pan-Magellanic field joining the two galaxies (Mao et al. 2008).

4.7 Radio halos

Radio halos are observed around the disks of most edge-on galaxies, but their radio intensity varies significantly. The halo luminosity in the radio range correlates with those in H α and X-rays (Tüllmann et al. 2006), although the halo shapes differ strongly between the different spectral ranges. The data suggests that star formation in the disk is the energy source for halo formation. Shape and radial extents of radio halos are determined by the energy input from supernova explosions per surface area in the projected disk (Dahlem et al. 1995).

In spite of the different intensities and vertical extents of radio halos, their exponential scale heights at 5 GHz were found to be similar (Dumke & Krause 1998; Heesen 2009a). The scale heights of the weakest halos, like NGC4565, and of the brightest ones known, NGC253 (Fig. 39) and NGC891 (Fig. 41), are similar. The average scale height of a sample of 13 galaxies edge-on galaxies from the

CHANG-ES sample (Wiegert et al. 2015) is 1.1 ± 0.3 kpc at 6 GHz and 1.4 ± 0.7 kpc at 1.5 GHz (Krause et al. 2018). The halo scale heights increase about linearly with the optical and radio diameters, while no significant relations were found with the star-formation rate nor with the magnetic field strength. Heesen et al. (2018) modelled the vertical profiles of the synchrotron emission and the spectral indices of 12 nearby edge-on galaxies to derive the exponential scale heights of the total magnetic field; they also found no correlations with the total star-formation rate nor with the star-formation rate per surface area.

In case of equipartition between the energy densities of magnetic field and cosmic rays, the exponential scale height of the total field h_B is at least $(3 - \alpha)$ times larger than the synchrotron scale height (where $\alpha \approx -1$ is the synchrotron spectral index in the halo). The values from Krause et al. (2018) yield $h_B \geq 5$ kpc. The real value depends on the energy losses of the cosmic-ray electrons propagating into the halo (section 2.2). With such large scale heights, the magnetic energy density in halos is much higher than that of the thermal gas, while still lower than that of the kinetic energy of the gas outflow.

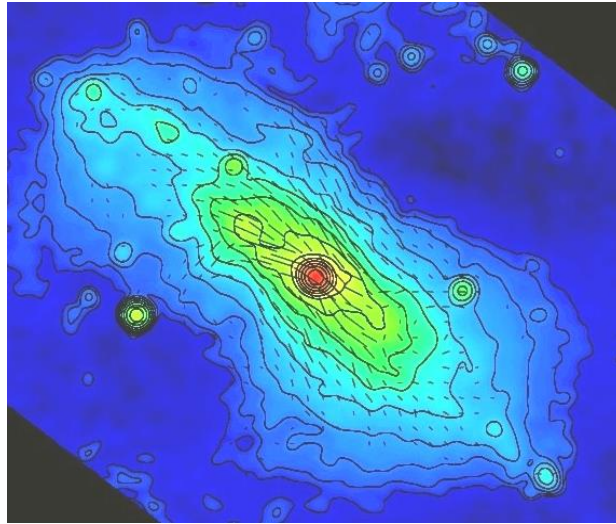


Fig. 39: Almost edge-on spiral galaxy NGC253. Total radio intensity (contours) and B -vectors at 4.86 GHz (6.2 cm), combined from observations with the VLA and the Effelsberg telescope (Heesen et al. 2009b).

Radio halos grow in size with decreasing observation frequency. The scale height of the halo of NGC891 is about twice higher in the LOFAR image at about 150 MHz compared to the VLA image at 1.5 GHz (Mulcahy et al., in prep.). The extent is limited by energy losses of the cosmic-ray electrons (CREs), i.e. synchrotron, inverse Compton, or adiabatic losses, or by escape from the halo (Heesen et al. 2009a; Krause et al. 2018). The stronger magnetic field in the central region causes stronger synchrotron loss, leading to the “dumbbell” shape of many radio halos, e.g. around NGC253 (Fig. 39). From the radio scale heights of NGC253 at three frequencies and the electron lifetimes (due to synchrotron, inverse Compton, and adiabatic losses) an outflow bulk speed of about 300 km/s was measured (Fig. 40) which is larger than the escape velocity. The scale heights of the halo of NGC891, measured at 150 MHz and 1.5 GHz in different regions along the galaxy’s major axis, decrease with increasing magnetic field strength which is a signature of dominating synchrotron losses of CREs (Mulcahy et al 2018).

Escaping flows are called *galactic winds*, while outflows slower than the escape velocity and returning to the disk are called *fountain flows*. Indications for galactic winds were found in many other edge-on galaxies (Heesen et al. 2018). The modelled outflow velocities range from about 100 km/s to about 700 km/s, similar to the escape velocities, and display a significant correlation with the star-formation rate. The halo scale height reveals a tight and almost linear anticorrelation with the mass surface density that is a measure of the gravitational potential of a galaxy. This gives evidence for a gravitational deceleration of the outflow (Krause et al. 2018).

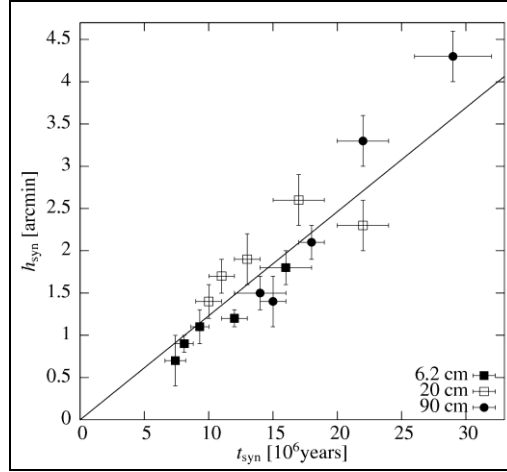


Fig. 40: Synchrotron scaleheights of the northern radio halo of NGC253 at different distances from the center and at different wavelengths, as a function of synchrotron lifetime of cosmic-ray electrons. The slope of the linear fit corresponds to a bulk outflow speed of about 300 km/s (Heesen et al. 2009a).

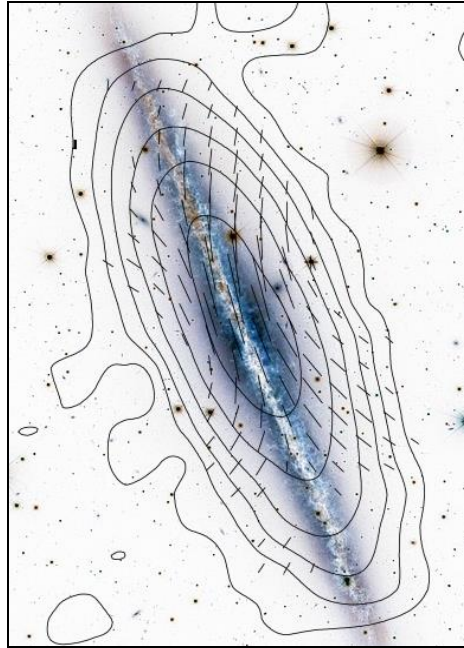


Fig. 41: Edge-on spiral galaxy NGC891. Total radio intensity (contours) and B-vectors at 8.35 GHz (3.6 cm), observed with the Effelsberg telescope (Krause 2009). The background optical image is from the CFHT.

Radio polarization observations of nearby galaxies seen edge-on generally show a disk-parallel field near the disk plane (Dumke et al. 1995). High-sensitivity observations of several edge-on galaxies like NGC253 (Fig. 39), NGC891 (Fig. 41), NGC5775 (Tüllmann et al. 2000; Soida et al. 2011), M104 (Krause et al. 2006), and many galaxies of the CHANG-ES sample (Wiegert et al. 2015) revealed vertical field components which increase with increasing height above and below the galactic plane and also with increasing radius, the so-called *X-shaped* halo fields. The X-pattern is even seen in NGC4565 with its low star-formation rate and a radio-faint halo (Krause 2009); thus this pattern seems to be a general phenomenon.

The large radio halos around the interacting galaxies M82 (Reuter et al. 1992; Adebahr et al. 2017) and NGC4631 (Krause 2009; Mora et al. 2013; Fig. 42) exhibit X-shaped halo fields with almost radial orientations in their inner regions. This indicates that the wind transport is more efficient here than in other spiral galaxies. A small gravitational potential of irregular galaxies or external forces by

neighbouring galaxies may be responsible for high outflow velocities. The action of the α - Ω dynamo can be suppressed under such conditions (Chamandy et al. 2015). The radio halo of NGC4631 was resolved into a few magnetic spurs, emerging from star-forming regions in the disk (Golla & Hummel 1994). These observations also support the idea of a fast galactic outflow that is driven by regions of star formation activity in the disk. The central outflows of the starburst galaxies M82 (Adebahr et al. 2017) and NGC253 (Heesen et al. 2011b) and the Seyfert galaxy NGC4388 (Fig. 51) are probably pervaded by helical magnetic fields.

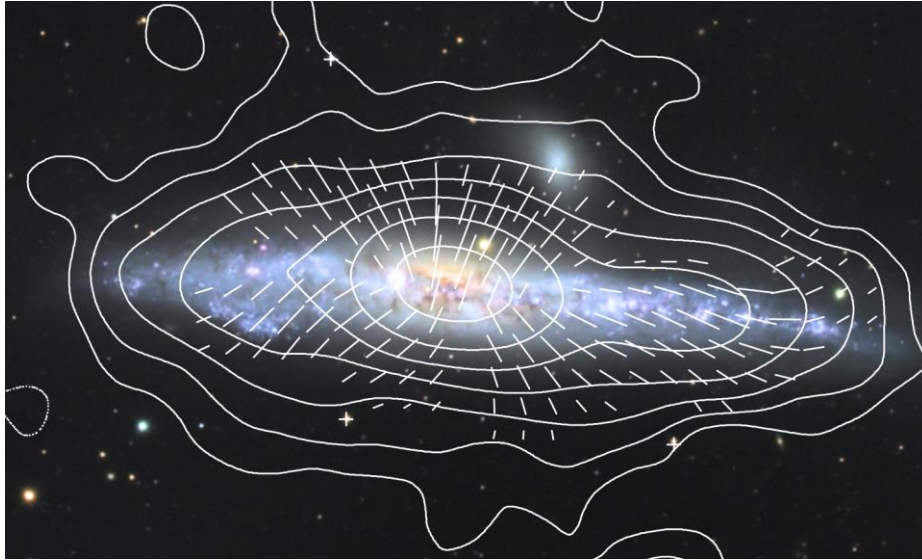


Fig. 42: Edge-on irregular galaxy NGC4631. Total radio intensity (contours) and B-vector at 8.35 GHz (3.6 cm), observed with the Effelsberg telescope (Krause 2009). The background optical image is from the Misti Mountain Observatory.

Polarization "vectors" do not distinguish between halo fields that are sheared into elongated loops or regular dynamo-type fields. A large-scale regular field can only be measured by Faraday rotation measures (RM) (section 2.4). RM patterns are very hard to measure in halos, because the field components along the line of sight are small. The detailed analysis of the multi-frequency observations of the highly inclined galaxy NGC253 (Fig. 39) allowed to identify an axisymmetric disk field with even symmetry and an X-shaped halo field, also of even symmetry (Fig. 43). The combined analysis of RMs of the diffuse emission and extragalactic sources revealed an even-symmetry halo field in the LMC (Mao et al. 2012).

The observation of X-shaped field patterns is of fundamental importance to understand the field origin in halos. α - Ω dynamo models for thin galaxy disks predict fields of even symmetry, in the simplest case a poloidal component of quadrupolar shape (section 2.6). The vertical component of such a quadrupolar field is largest near the rotation axis and decreases with distance from the rotation axis. Such an effect is possibly seen in NGC4631 (Fig. 42), while in several other edge-on galaxies the vertical field component *increases* with increasing distance from the rotation axis, giving rise to an X-shape. Furthermore, the field strength of a purely quadrupole-type field decreases rapidly with distance from the center (e.g. Prouza & Šmída 2003), while the observed radial profiles of polarized emission show a slow exponential decrease. The field structure cannot be a simple quadrupole.

Several analytical descriptions of divergence-free, X-shaped magnetic fields in galaxy halos were presented by Ferrière & Terral (2014), possibly generated by dynamos including outflows with moderate velocities (section 2.6). An alternative analytical model invokes a rotational velocity lag in the halo and predicts an outwards-winding helical field (Henriksen & Irwin 2016). Numerical MHD models predict vertical outflows and strong vertical fields (Pakmor et al. 2017).

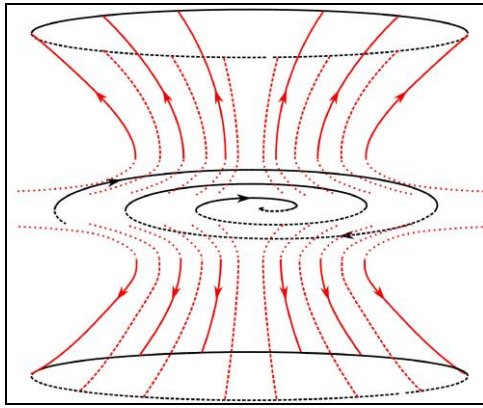


Fig. 43: Model of the symmetric (outwards-directed) halo field of NGC253. The spiral disk field is also symmetric with respect to the plane (from Heesen et al. 2009b).

In summary, the detection of X-shaped fields in all galaxies observed so far can be explained by dynamo action and/or outflows and/or rotational velocity lag. If outflows are a general phenomenon in galaxies, they can magnetize the intergalactic medium (IGM). Starburst dwarf galaxies in the early Universe were especially efficient in magnetizing the IGM. The extent of magnetic fields into the IGM is not yet visible. Energy losses of the cosmic-ray electrons prevent the emission of radio waves beyond some height while magnetic fields may still exist much further outwards. Low-energy electrons live longer, can propagate further into the IGM and emit synchrotron emission at low frequencies (section 2.2). Observations with the Low Frequency Array (LOFAR) are expected to reveal larger radio halos (section 5).

4.8 Interacting galaxies

Gravitational interaction between galaxies leads to asymmetric gas flows, compression, shear, enhanced turbulence and outflows. Compression and shear of gas flows can also modify the structure of galactic and intergalactic magnetic fields. In particular, fields can become aligned along the compression front or perpendicular to the velocity gradients. Such gas flows make turbulent fields highly anisotropic.

The classical interacting galaxy pair is NGC4038/39, the “Antennae” (Fig. 44). It shows bright, extended radio emission filling the volume of the whole system, with no dominant nuclear sources. In the interaction region between the galaxies, where star formation did not yet start, and at the north-eastern edge of the system, the magnetic field is partly ordered, probably the result of compression and shearing motions along the tidal tail, respectively. The regular field in the tidal tail is about $8 \mu\text{G}$ strong and extends to about 20 kpc distance from the galaxy (Basu et al. 2017). Particularly strong, almost unpolarized emission comes from a region of violent star formation, hidden in dust, at the southern end of a dense cloud complex extending between the galaxies. In this region, highly turbulent magnetic fields reach strengths of $\approx 20 \mu\text{G}$. The mean total magnetic field is stronger than in normal spirals, but the mean degree of polarization is unusually low, implying that the ordered field, generated by compression, has become tangled in the region with violent star formation. After an interaction, the magnetic field strength in a galaxy is expected to decrease again to its normal value (Drzazga et al. 2011).

Interaction with a dense intergalactic medium also imprints unique signatures onto magnetic fields and thus the radio emission. The Virgo cluster is a location of especially strong interaction effects, and almost all cluster galaxies observed so far show asymmetries of their polarized emission (Appendix, Table 7). In NGC4254, NGC4522, and NGC4535 (Fig. 45), the polarized emission on one side of the galaxy is shifted towards the edge of the spiral arm, an indication for shear by tidal tails or ram pressure by the intracluster medium. The heavily disrupted galaxy NGC4438 (Vollmer et al. 2007) has almost its whole radio emission (total power and polarized) displaced towards the giant elliptical M86 to which it is also connected by a chain of $\text{H}\alpha$ -emitting filaments.

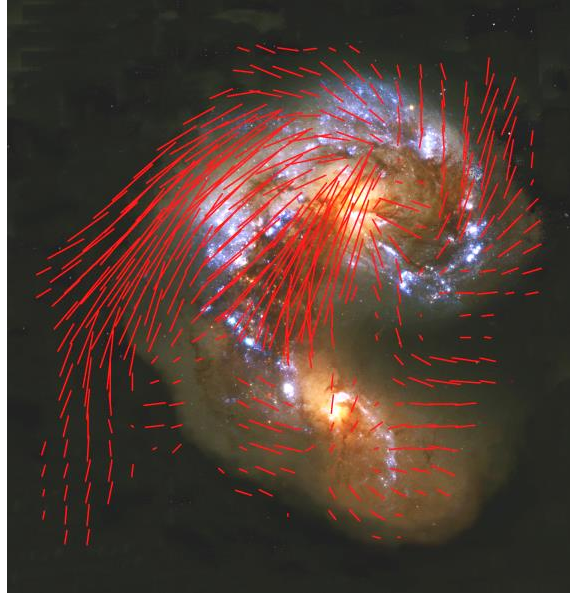


Fig. 44: “Antennae” galaxy pair NGC4038/39. B-vectors of polarized radio intensity at 4.86 GHz (6.2 cm), observed with the VLA (Chyży & Beck 2004). The background optical image is from the Hubble Space Telescope.

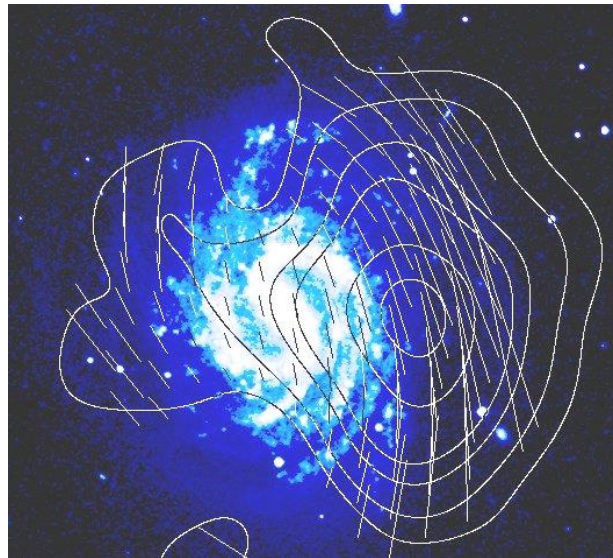


Fig. 45: Spiral galaxy NGC4535 in the Virgo cluster. Polarized radio intensity (contours) and B-vectors at 4.75 GHz (6.3 cm), observed with the Effelsberg telescope (Weżgowiec et al. 2007). The background optical image is from the Digital Sky Survey.

Interaction may also induce violent star-formation activity in the nuclear region or in the disk which may produce huge radio lobes due to outflowing gas and magnetic field. The lobes of the Virgo spiral NGC4569 reach out to at least 24 kpc from the disk and are highly polarized (Fig. 46). However, there is neither an active nucleus nor a recent starburst in the disk, so that the radio lobes are probably the result of nuclear activity in the past.

Tidal interaction is also the probable cause of the asymmetric appearance of NGC3627 within the Leo Triplet (Fig. 47). While the ordered field in the western half is strong and precisely follows the dust lanes, a bright magnetic arm in the eastern half crosses the optical arm and its massive dust lane at a large angle. No counterpart of this feature was detected in any other spectral range. Either the optical arm was recently deformed due to interaction or ram pressure, or the magnetic arm is an out-of-plane feature generated by interaction.

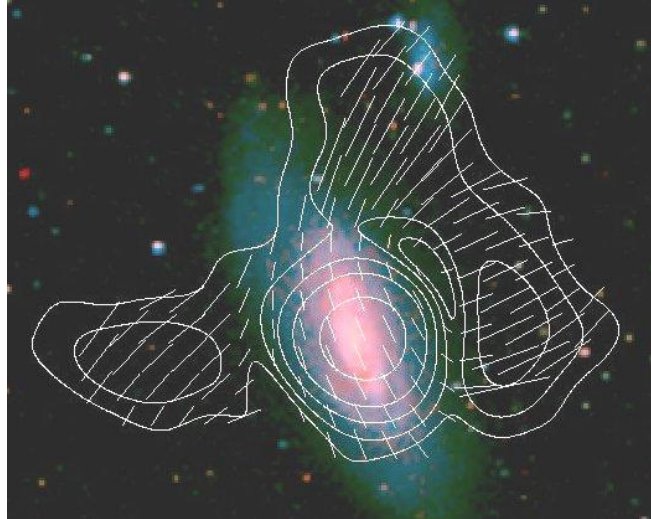


Fig. 46: Spiral galaxy NGC4569 in the Virgo cluster. Polarized radio intensity (contours) and B-vectors at 4.75 GHz (6.3 cm), observed with the Effelsberg telescope (Chyży et al. 2006). The background optical image is from the Digital Sky Survey.

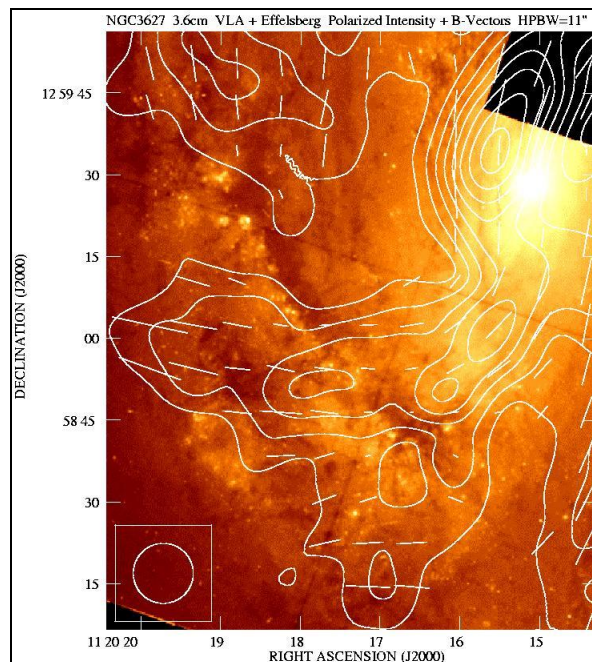


Fig. 47: Interacting spiral galaxy NGC3627. Polarized radio intensity (contours) and B-vectors at 8.46 GHz (3.5 cm), combined from observations with the VLA and Effelsberg telescopes (Soida et al. 2001). The background optical image is from the Hubble Space Telescope.

In a few cases a gaseous bridge between colliding galaxies is associated with radio emission that is due to relativistic electrons pulled out from the disks together with gas and magnetic fields. This phenomenon (called “taffy galaxies”) seems to be rare. Only two objects, UGC12914/5 and UGC813/6, were found so far (Condon et al. 2002; Drzazga et al. 2011). This may be due to the steep spectrum of the bridges, making them hard to detect at centimeter radio wavelengths.

In compact galaxy groups tidal interactions may trigger rapid star formation in one or more member galaxies, causing supersonic outflows of hot gas. Some compact groups have long HI tails, indicating strong, tidally-driven outflows of the neutral gas from the system. If the expelled gas was magnetized it might provide the supply of magnetic fields into the intergalactic space. Starburst galaxies (either dwarf and massive) constitute the basic source responsible for the enrichment of the intra-group

medium with relativistic particles and magnetic fields. There are grounds to expect that the compact galaxy groups show diffuse radio emission, with a spectrum rapidly steepening away from the cosmic-ray sources in galactic disks.

The best studied example of a compact group is Stephan's Quintet (at a distance of 85 Mpc), with its pool of hot gas extending between the galaxies (Nikiel-Wroczyński et al. 2013b). It shows a huge, long filament visible in radio continuum. Strong polarization of this intra-group emission (Fig. 48) indicates a substantial content of ordered (probably shock-compressed) magnetic fields. Intergalactic fields were also found in the compact groups HCG, HCG44, and HCG60 (Nikiel-Wroczyński et al. 2017).

In summary, polarized radio emission is an excellent tracer of tidal effects between galaxies and of ram pressure in the intracluster medium. As the decompression and diffusion timescales of the field are very long, it keeps memory of events in the past, up to the lifetime of the illuminating cosmic-ray electrons. Low-frequency radio observations will trace interactions that occurred many Gyr ago and are no longer visible in other spectral ranges. Tidal tails from interacting galaxies may also constitute a significant source of magnetic fields in the intracluster and intergalactic media.



Fig. 48: Stephan's Quintet of interacting galaxies. Total radio intensity (contours) and B-vectors at 4.86 GHz (6.2 cm), observed with the VLA (from Marian Soida, Kraków University). The background optical image is from the Hubble Space Telescope.

4.9 Galaxies with jets

Nuclear jets are observed in several spiral galaxies. These jets are weak and small compared to those of radio galaxies and quasars. Detection is further hampered by the fact that they emerge at some angle with respect to the disk, so that little interaction with the ISM occurs. If the nuclear disk is oriented almost perpendicular to the disk, the jet hits a significant amount of ISM matter, cosmic-ray electrons are accelerated in shocks, and the jet becomes radio-bright. This geometry was found for NGC4258 by observations of the water maser emission from the nuclear disk that has an inner radius of 0.13 pc and is seen almost edge-on (Greenhill et al. 1995). This is probably why NGC4258 is one of the rare cases where a large and bright radio jet of at least 15 kpc length is observed (van Albada & van der Hulst 1982; Krause & Löhner 2004). The total intensity map of NGC4258 (Fig. 49) reveals that the jets emerge from the Galactic center perpendicular to the nuclear disk which is oriented in east-west direction, and bend out to become the "anomalous radio arms", visible out to the boundaries of the spiral galaxy. The magnetic field orientation is mainly along the jet direction. The equipartition field strength is about 300 μG (at the resolution of about 100 pc) which is a lower limit due to energy losses of the cosmic-ray electrons and the limited resolution.

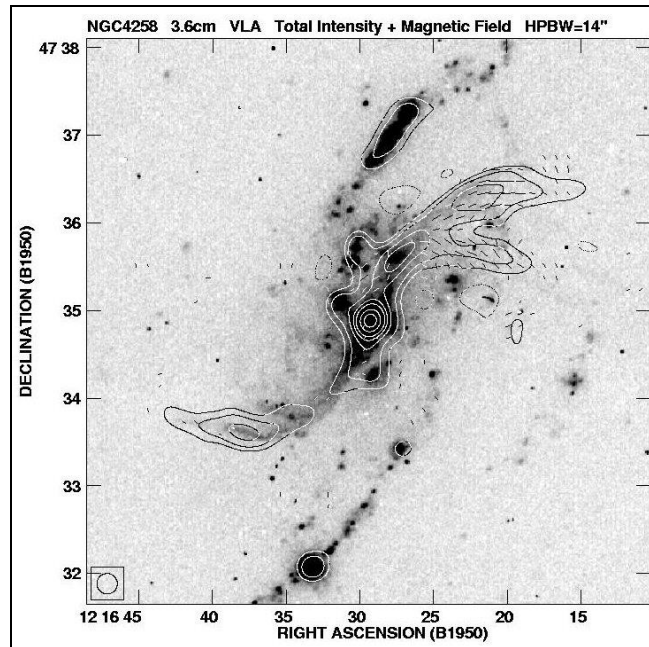


Fig. 49: Spiral galaxy NGC4258 with two jets. Total radio intensity (contours) and B-vectors at 8.46 GHz (3.5 cm), observed with the VLA (Krause & Löhrr 2004). The background $H\alpha$ image is from the Hoher List Observatory of the University of Bonn.

The barred galaxy NGC7479 also shows remarkable jet-like radio continuum features: bright, narrow, 12 kpc long in projection, and containing an aligned magnetic field (Fig. 50). The lack of any optical or near-infrared emission associated with the jets suggests that at least the outer parts of the jets are extraplanar features, although close to the disk plane. The equipartition strength is 35 – 40 μG for the total magnetic field and about 10 μG for the ordered magnetic field in the jets. According to Faraday rotation measurements, the large-scale regular magnetic field along the bar points towards the nucleus on both sides. Multiple reversals on scales of 1 – 2 kpc are detected, probably occurring in the galaxy disk in front of the eastern jet by anisotropic fields in the shearing gas flow in the bar potential.

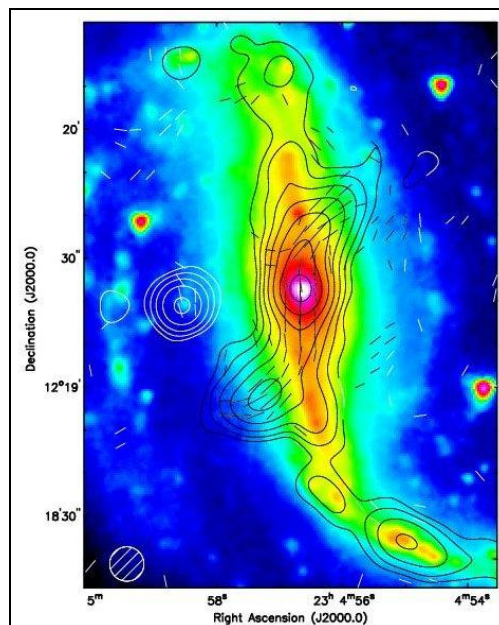


Fig. 50: Barred spiral NGC7479 with two jets. Total radio intensity (contours) and B-vectors at 8.46 GHz (3.5 cm), observed with the VLA (Laine & Beck 2008). The background shows a Spitzer/IRAC infrared image at 3.6 μm (NASA/JPL-Caltech/Seppo Laine).

NGC4388 in the Virgo cluster has a nuclear outflow emerging from the active Seyfert-type nucleus extending to about 5 kpc from the center (Damas-Segovia et al. 2016; Fig. 51). The radio emission is highly polarized, with B-vectors indicating a helical field. Further blobs of polarized emission above the plane in the north-west and south-east with vertical fields probably arise from a galactic wind. Highly polarized radio emission from kpc-sized jets has also been detected e.g. in NGC3079 (Cecil et al. 2001) and in the outflow lobes of the Circinus Galaxy (Elmouttie et al. 1995).

Jets in spiral galaxies may be more frequent than the available radio observations suggest. Future low-frequency observations may help, because they may show weak synchrotron emission from interface regions between the jets and the low-density halo gas.

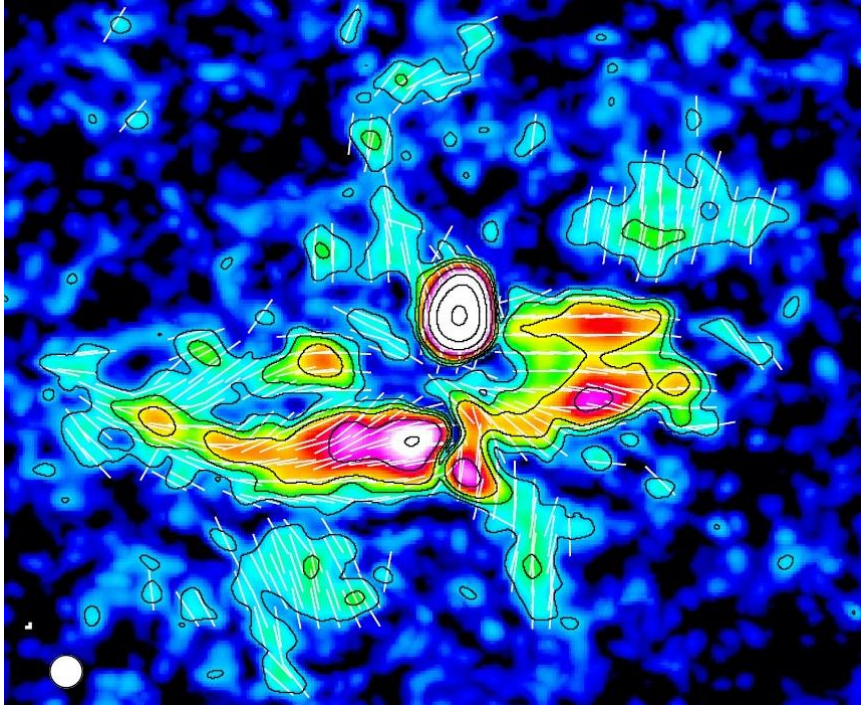


Fig. 51: Edge-on spiral galaxy NGC4388 in the Virgo cluster. Polarized radio intensity (contours) and B-vectors at 6 GHz (5.0 cm), observed with the VLA (Damas-Segovia et al. 2016).

4.10 Early-type and dwarf spheroidal galaxies

Elliptical galaxies with active nuclei are among the brightest known radio sources. Their jets and radio lobes are generated by magneto-hydrodynamic processes that are discussed elsewhere. Radio emission from quiet elliptical and S0 galaxies, if any, is also associated with their nuclei (Fabbiano et al. 1987). A significant fraction of early-type galaxies is still forming stars in the inner regions and emits synchrotron emission (Nyland et al. 2017). Their radio luminosity follows a similar radio-IR correlation as that for spiral galaxies (section 4.3), indicating amplification of turbulent magnetic fields. Polarized emission has not yet been detected, except for the Sa galaxy M104 with its prominent dust ring where Krause et al. (2006) found weak, ordered magnetic fields.

The existence of magnetic fields in the halos of ellipticals without active nucleus and without any star formation is a matter of speculation. Regular fields are not expected in ellipticals because the lack of ordered rotation prevents the action of the α - Ω dynamo. Dwarf spheroidal galaxies have some ordered rotation, but lack turbulent gas. Turbulence in the hot gas of large ellipticals may drive a small-scale dynamo and generate turbulent fields with a few μG strength and turbulent scales of a few 100 pc (Moss & Shukurov 1996). However, there are no cosmic-ray electrons and hence no synchrotron emission. Detection of turbulent magnetic fields is only possible via the dispersion of Faraday rotation measures towards polarized background sources. Most large ellipticals are located in galaxy clusters where Faraday rotation is dominated by the turbulent fields of the intracluster gas. For small ellipticals,

the number of polarized background sources will only be sufficient with much more sensitive radio telescopes like the SKA. This leaves isolated giant ellipticals for future studies.

Dwarf spheroidal galaxies are of interest to search for synchrotron emission from secondary electrons and positrons generated by the decay of dark-matter by WIMP annihilations, e.g. neutralinos (Colafrancesco et al. 2007). These galaxies do not generate thermal emission or primary electrons from star formation. Detection of radio emission would be of high importance, but all attempts failed so far. The main uncertainty is origin of magnetic fields in such systems (see above). If the field strength is a few μG , detection of synchrotron emission from dark-matter decay may be possible. Radio observations of several dwarf galaxies yielded only upper limits so far (Spekkens et al. 2013). The SKA should provide much improved data (Colafrancesco et al. 2015).

5. Outlook

Thanks to radio polarization observations, the global properties of interstellar magnetic fields in external galaxies and the field structures on pc and sub-pc sizes in the Milky Way are reasonably well known. However, the processes connecting the features at large and small scales are not understood because the angular resolution in external galaxies is too low with present-day radio telescopes. Most of the existing polarization data was observed in single frequency bands and may suffer from depolarization by gradients of Faraday rotation or by different Faraday rotation components within the beam or along the line of sight. Modern radio telescopes are equipped with broadband receivers and multichannel polarimeters, allowing application of RM Synthesis (section 2.4) and resolving Faraday components. This method is presently revolutionizing radio polarization observations.

New and planned telescopes will widen the range of observable magnetic phenomena. The importance of polarimetry for the planned giant optical telescopes still needs to be established, while huge progress is expected in the radio range. The PLANCK satellite and several balloon instruments (PILOT, BLAST-pol) has improved the sensitivity of polarimetry in the submillimeter range at arcminute resolution. The Atacama Large Millimetre Array (ALMA) provides greatly improved sensitivity at arcsecond resolution for detailed imaging diffuse polarized emission from dust grains and for detection of the Zeeman effect in molecular clouds in the Milky Way and in external galaxies. High-resolution, deep observations at high frequencies (≥ 5 GHz), where Faraday effects are small, require a major increase in sensitivity for continuum observations which can be achieved by the Jansky Very Large Array (VLA) and the planned Square Kilometre Array (SKA). The detailed structure of the magnetic fields in the ISM of nearby galaxies and in galaxy halos will be observed with the SKA, giving direct insight into the interaction between magnetic fields and the various gas components (Beck et al. 2015). High angular resolution is also needed to distinguish between regular and anisotropic (sheared) fields and to test various models of the interaction between spiral shocks and magnetic fields. The power spectra of turbulent magnetic fields can be measured down to small scales. The SKA will also allow to measure the Zeeman effect in much weaker magnetic fields in the Milky Way and also in nearby galaxies.

The SKA will detect synchrotron emission from Milky Way-type galaxies at redshifts of $z \leq 1.5$ (Fig. 52) and their polarized emission to $z \leq 0.5$ (assuming 10% polarization). Bright starburst galaxies can be observed at larger redshifts, but are not expected to host ordered or regular fields. Total synchrotron emission, signature of total magnetic fields, can be detected in starburst galaxies with the SKA out to large redshifts, depending on luminosity and magnetic field strength (Fig. 52). However, for fields weaker than $3.25 \mu\text{G} (1+z)^2$, energy losses of cosmic-ray electrons are dominated by the inverse Compton effect with photons of the cosmic microwave background, so that the particle energy is transferred mostly to X-rays and not to the radio domain. Furthermore, in the strong fields of young galaxies the energy range of electrons emitting in the GHz range is shifted to low energies where ionization and bremsstrahlung losses are strong. The expected evolution of luminosities and synchrotron spectra of galaxies between redshifts of 5 and 0.1 were computed by Schober et al. (2016). The maximum redshift until which synchrotron emission can be detected can constrain models of the evolution of magnetic fields in young galaxies (Schleicher & Beck 2013).

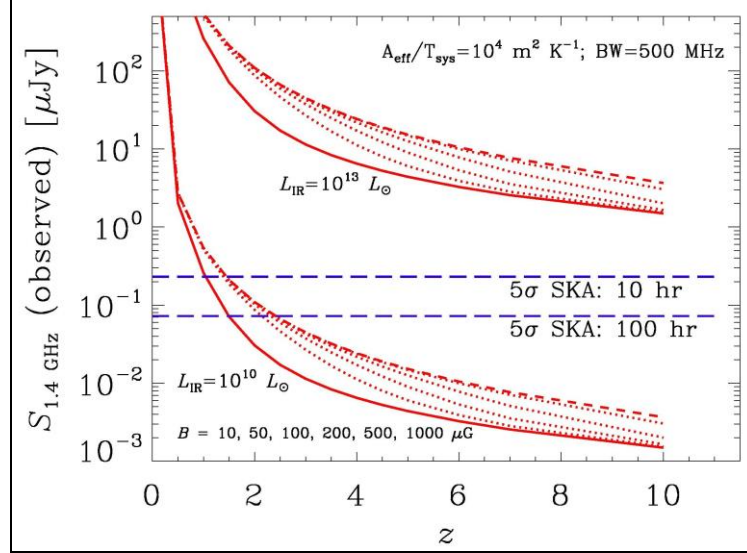


Fig. 52: Total synchrotron emission at 1.4 GHz as a function of redshift z , total magnetic field strength B and total infrared luminosity L_{IR} . The 5σ detection limits for 10 h and 100 h integration time with the SKA are also shown (Murphy 2009).

Ordered fields of nearby galaxies seen edge-on near the disk plane are preferably oriented parallel to the plane (section 4.7). As a result, polarized emission can be detected from distant, *unresolved* galaxies if they are symmetric (not distorted by interaction) and their inclination is larger than about 20° (Stil et al. 2009). This opens another method to search for ordered fields in distant galaxies. As the plane of polarization is almost independent of wavelength, distant spiral galaxies with known orientation of their major axis can also serve as background polarized sources to search for Faraday rotation by intergalactic fields in the foreground.

If polarized emission of galaxies is too weak to be detected, the method of *RM grids* towards polarized background QSOs can still be applied to measure the strength and structure of regular fields. Faraday rotation in an intervening galaxy (identified via absorption lines in its optical spectrum) occurs if its field is regular on spatial scales larger than that corresponding to the angular size of the background source. Regular fields of several μG strengths were discovered in galaxies up to redshifts of about 2 (Bernet et al. 2008; 2013; Kronberg et al. 2008; Farnes et al. 2014b; 2017). The distance limit of this method is given by the polarized flux of the background QSO which can be much larger than that of the intervening galaxy, so that it can be applied to very large distances, even near to those of young QSOs ($z \geq 5$). The *gravitational lens effect* allows to measure several lines of sight through the lensing galaxy and hence to unambiguously measure its RM. The first application of this method led to the discovery of a regular field of a few μG strength in a galaxy at $z = 0.439$ (Mao et al. 2017). This opens the prospect to investigate magnetic fields in young galaxies and to search for their first fields with future radio telescopes like the SKA.

A reliable model for the structure of the magnetic field of an intervening galaxy needs many RM values, hence a sufficiently large number density of polarized background sources. If the background QSO has a polarized jet, some information about the large-scale field pattern in the intervening galaxy can be obtained (Kronberg et al. 1992). At least 10 randomly distributed background sources behind a galaxy disk are needed to recognize simple magnetic patterns, and several 1000 sources for a full reconstruction (Stepanov et al. 2008). The RM values measured today have been reduced by the redshift dilution factor of $(1+z)^{-2}$, so that high RM accuracy is needed. Present-day observations are not sensitive enough, and one has to wait for the SKA and its precursor telescopes.

Detection of regular fields in young galaxies is a critical test of α - Ω dynamo models. Dynamo theory predicts timescales of amplification and coherent ordering of magnetic fields in galaxies (section 2.6). Based on models describing the formation and evolution of dwarf and disk galaxies, the probable evolution of turbulent and regular magnetic fields can be tested observationally (Arshakian et al. 2009; Rodrigues et al. 2015):

- Strong isotropic turbulent fields (in equipartition with turbulent gas motions) and hence unpolarized synchrotron emission are expected in galaxies at $z < 10$.
- Strong regular fields (which are coherent over a scale of about 1 kpc) and hence polarized synchrotron emission and fluctuating RMs are expected in galaxies at $z \leq 3$.
- Large-scale patterns of fully coherent regular fields and hence polarized synchrotron emission and large-scale RM patterns are expected in dwarf and Milky-Way type galaxies $z \approx 1 - 1.5$.
- Giant galaxies (disk radius > 15 kpc) should not yet have generated fully coherent fields.
- Major mergers enhance turbulent fields, but destroy regular fields, and delay the formation of fully coherent fields. The lack of regular fields in nearby galaxies can be a signature of major mergers in the past.

The detections of total synchrotron emission in starburst galaxies at $z \leq 4$ and of RMs from intervening galaxies at $z \leq 2$ (see above) are consistent with dynamo theory. The observed field patterns are so far in agreement with the predictions of the α - Ω dynamo (sections 4.4 and 4.7). Crucial tests of dynamo action will be possible in young galaxies. Detection of regular fields at $z \geq 3$ would call for a faster type of dynamo or a different process. On the other hand, the failure to detect global coherent field patterns in galaxies $z \approx 1$ would indicate that the time needed for field ordering is even longer than the α - Ω dynamo theory predicts. If the bisymmetric spiral (BSS) magnetic pattern turns out to dominate in distant galaxies, in contrast to that in nearby galaxies, this would indicate that the fields could be primordial or intergalactic fields that are twisted and amplified by differential rotation.

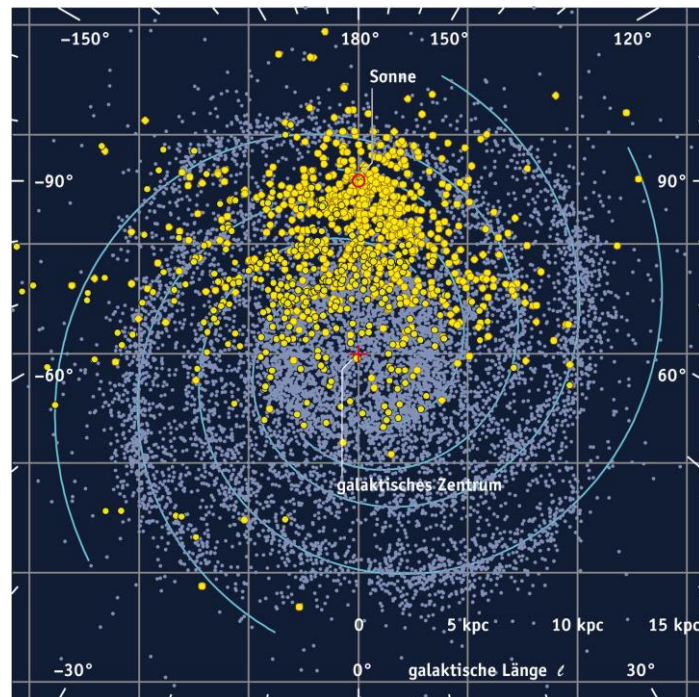


Fig. 53: Simulation of pulsars in the Milky Way that will be detected with the SKA (blue), compared to about 2000 pulsars known today (yellow) (from Jim Cordes, Cornell University). Graphics: Sterne und Weltraum.

The SKA “Cosmic Magnetism” Key Science Project plans to observe a polarization survey over the entire accessible sky with the SKA-MID Band 2 at around 1.4 GHz (Johnston-Hollitt et al. 2015). Within 1 h integration per field this will allow detection of about 10 million discrete extragalactic sources and measurement of their RMs, about 300 RMs per square degree, about 10000 RMs from pulsars in the Milky Way (Fig. 53) and several 100 extragalactic pulsars. About 1000 extragalactic sources are expected in the area around M31 (Fig. 54). This fundamental survey will be used to model the structure and strength of the magnetic fields in nearby and intervening galaxies (Beck et al. 2015), in galaxy clusters, and in the intergalactic medium. The SKA will unravel the 3D structure and configurations of magnetic fields in the Milky Way on sub-parsec to galaxy scales, including the field structure in the Galactic Center (Haverkorn et al. 2015; Han et al. 2015). The global configuration of

the Milky Way's magnetic field in the disk, probed through pulsar RMs, will resolve the controversy about reversals in the Galactic plane. Characteristics of magnetic interstellar turbulence can also be determined from the RM grid. A pilot all-sky survey called POSSUM with the Australian SKA Precursor (ASKAP) is planned. MeerKAT, the South African SKA precursor, and APERTIF, the Dutch SKA pathfinder telescope, have higher sensitivity, but a smaller field of view than ASKAP and will concentrate on measuring RM grids centered on individual objects.

Progress is also expected at low radio frequencies. Present-day measurements of galactic magnetic fields by synchrotron emission are limited by the lifetime and diffusion length of the cosmic-ray electrons that illuminate the fields. With typical diffusion lengths of only 1 kpc away from the acceleration sites in star-forming regions, the size of galaxies at centimeter wavelengths is not much larger than that in the optical or infrared spectral ranges. There is indication that magnetic fields probably extend much further into the intergalactic space (section 4.7). The Low Frequency Array (LOFAR) and the Murchison Widefield Array (MWA), and the low-frequency part of the planned SKA are/will be suitable instruments to search for extended synchrotron radiation at the lowest possible levels in outer galaxy disks and halos and investigate the transition to intergalactic space. While most of the disk is depolarized at low frequencies (Mulcahy et al. 2014), polarization may still be detectable from the outer regions.

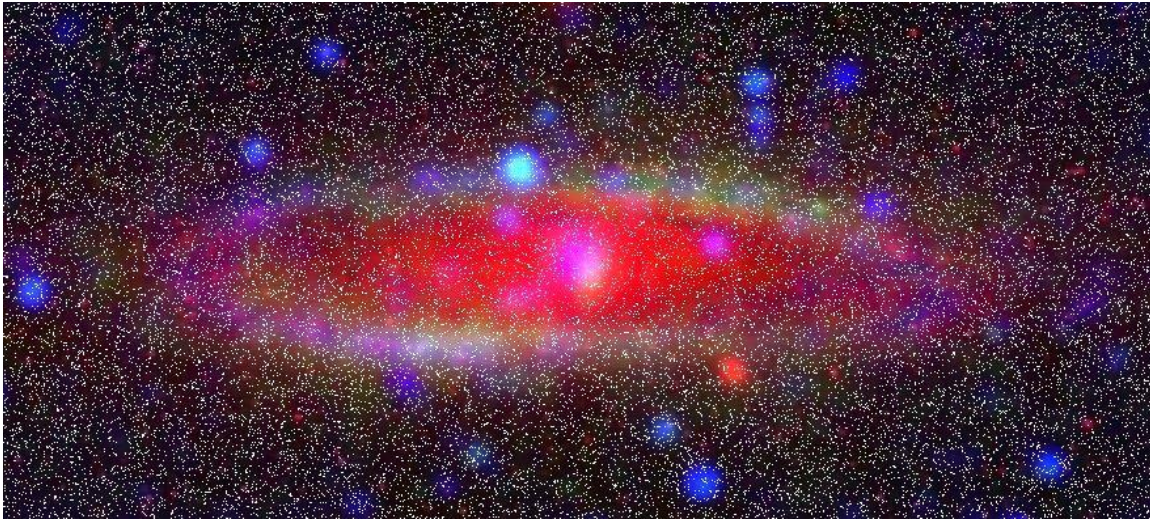


Fig. 54: Simulation of RMs towards background sources (white points) in the region of M31 observable with the SKA within 1 h integration time. Optical emission from M31 is shown in red, diffuse total radio continuum intensity in blue and diffuse polarized intensity in green (from Bryan Gaensler, University of Toronto).

The filaments of the local Cosmic Web may contain *intergalactic magnetic fields*, possibly enhanced by IGM shocks, and this field may be detectable by direct observation of total synchrotron emission or by Faraday rotation towards background sources (Akaori et al. 2014). For fields of $10^{-8} - 10^{-7}$ G with 1 Mpc coherence length and 10^{-5} cm^{-3} electron density, $|\text{RM}|$ of 0.1 – 1 rad m^{-2} is expected. An overall intergalactic field is much weaker and may only become evident as increased $|\text{RM}|$ towards QSOs at redshifts of $z > 3$ by averaging over a large number of sources (Vacca et al. 2016). As the Faraday rotation angle increases with λ^2 , searches for low $|\text{RM}|$ should preferably be done at low frequencies.

In summary, the SKA and its pathfinders (VLA, LOFAR, MWA, APERTIF) and precursors (ASKAP, MeerKAT) will measure the structure and strength of the magnetic fields in the Milky Way, in intervening galaxies, and possibly in the intergalactic medium. Looking back into time, the future telescopes could shed light on the origin and evolution of cosmic magnetic fields. The observational methods are:

- RM grids of extragalactic sources and pulsars to map the detailed 3D structure of the Milky Way's magnetic field (0.2–1 GHz)
- High-resolution mapping of total and polarized synchrotron emission from galaxy disks and halos of nearby galaxies at high frequencies (≥ 5 GHz)
- Mapping of the total and polarized synchrotron emission from the outer disks and halos of nearby galaxies and galaxy groups at low frequencies (≤ 1 GHz)
- Reconstruction of 3D field patterns in nearby galaxies by RM Synthesis of the diffuse polarized emission
- Reconstruction of 3D field patterns in nearby galaxies from RM grids towards polarized background sources
- Recognition of patterns of regular fields in galaxies from RM grids towards polarized background sources (at $z \leq 0.02$)
- Search for polarized synchrotron emission from distant galaxies (at $z \leq 0.5$)
- Search for total synchrotron emission from distant starburst galaxies (at $z \leq 3$)
- Search for regular fields in very distant intervening galaxies towards QSOs (at $z \leq 5$).

Fundamental questions are waiting to be answered:

- When were the first magnetic fields generated and amplified: in young galaxies, in protogalactic clouds, or are they relics from the early Universe, before galaxies were formed?
- How and how fast were magnetic fields amplified and ordered in the interstellar medium?
- How did magnetic fields affect the evolution of galaxies?
- How important are magnetic fields for the physics of galaxies, like the efficiency to form stars from gas, the formation of spiral arms, or the generation of outflows?
- How strong and how ordered are magnetic fields in intergalactic space?
- Can outflows from galaxies magnetize the intergalactic space?
- What is the large-scale structure of the Milky Way's magnetic field?
- How strongly are extragalactic ultrahigh-energy cosmic rays deflected by magnetic fields in the Milky Way and in intergalactic space?

Acknowledgements

The authors would like to thank many of our colleagues who have pursued the studies of magnetic fields in the Milky Way and in galaxies for the past 45 years, especially Elly M. Berkhuijsen, Marita Krause, Sui Ann Mao, Patricia Reich, and Wolfgang Reich, at MPIfR Bonn. Many excellent cooperation projects in this field were performed with groups in Kraków (Poland), DRAO Penticton (Canada), NAOC Beijing (China), Moscow and Perm (Russia), Newcastle (UK), Potsdam and Bochum (Germany). We thank Marek Urbanik for compiling Table 7. Elly M. Berkhuijsen, Katia Ferrière, Marijke Haverkorn, Marita Krause, and Anvar Shukurov are acknowledged for carefully reading of the manuscript and for many useful comments. We thank JinLin Han for many discussions and for providing a few figures. – This work was supported by DFG Research Unit FOR1254.

Appendix

A.1 Catalogue of radio surveys of the Milky Way

Table 2: All-sky or all-hemisphere radio total intensity surveys

Frequency	Beam	Reference
45 MHz	$\approx 4^\circ$	Guzmán et al. 2011
150 MHz	$3^\circ.6$	Landecker & Wielebinski 1970
408 MHz	2°	Haslam et al. 1982
1.4 GHz	$0^\circ.6$	Reich 1982; Reich & Reich 1986; Reich et al. 2001
2.3 GHz	$0^\circ.33$	Jonas et al. 1998 (southern hemisphere)
2.7 GHz	$0^\circ.33$	Reif et al. 1987 (northern hemisphere)
23 – 94 GHz	$0^\circ.8 - 0^\circ.2$	Hinshaw et al. 2009
20 – 100 GHz	1°	Ade et al. (Planck Collaboration) 2016

Table 3: All-sky or all-hemisphere total intensity and linear polarization surveys

Frequency	Beam	Reference
189 MHz	$15.6'$	Bernardi et al. 2013 (southern hemisphere, 2400 deg ²)
408 MHz	7.5°	Wielebinski et al. 1962 (northern hemisphere)
	2°	Berkhuijsen & Brouw 1963 (northern hemisphere)
	7.5°	Wielebinski & Shakeshaft 1964 (northern hemisphere)
	$\approx 1^\circ$	Mathewson & Milne 1965 (southern hemisphere)
0.3 – 1.8 GHz	$30' - 60'$	Wolleben et al. 2009 (GMIMS; all-sky, planned)
1.28 – 1.75 GHz	$40'$	Wolleben et al. 2010a; 2010b; Sun et al. 2015; Hill et al. 2017 (GMIMS-HBN)
1.4 GHz	$36'$	Wolleben et al. 2006; Testori et al. 2008 (all-sky)
1.4 GHz	$\approx 13'$	Rudnick & Brown 2009 (northern hemisphere)
2.3 GHz	$9'$	Carretti et al. 2018 (in prep.) (S-PASS; southern hemisphere)
5 GHz	$44'$	King et al. (2014) (C-BASS; all sky, in preparation)
23 – 94 GHz	$0^\circ.8 - 0^\circ.2$	Kogut et al. 2007; Hinshaw et al. 2009 (all-sky)
28.4 GHz	1°	Ade et al. (Planck Collaboration) 2016 (all-sky)
353 GHz	1°	Ade et al. (Planck Collaboration) 2015a (all-sky)

Table 4: Radio surveys of the Galactic plane with angular resolutions of a few arcminutes

Frequency	Beam	Area (Galactic coordinates)	Reference
325 MHz	$\approx 4'$	selected areas	Wieringa et al. 1993
350 MHz	$\approx 5'$	selected areas	Haverkorn et al. 2003; 2004
408 MHz	$\approx 1'$	$147.3^\circ > l > 74.2^\circ$ $-7.7^\circ < b < 8.7^\circ$	Taylor et al. 2003
1.4 GHz	$\approx 1'$	$147.3^\circ > l > 74.2^\circ$ $-3.6^\circ < b < 5.6^\circ$	Taylor et al. 2003
1.4 GHz	$\approx 1'$	$67^\circ > l > 18^\circ$ $b \pm 1^\circ.5$	Stil et al. 2006
1.4 GHz (PI)	$\approx 1'$	$358^\circ > l > 253^\circ$ $b \pm 1^\circ.5$	Haverkorn et al. 2006
1.4 GHz (PI)	$\approx 1'$	$175^\circ > l > 66^\circ$ $-3^\circ < b < 5^\circ$	Landecker et al. 2010 (CGPS)
1.4 GHz	$9'$	$162^\circ > l > 93^\circ$ $b \pm 4^\circ$	Kallas & Reich 1980
1.4 GHz	$9.4'$	$240^\circ > l > 95.5^\circ$ $-4^\circ < b < 5^\circ$	Reich et al. 1990a; 1997
1.4 GHz (PI)	$9.4'$	$230^\circ > l > 25^\circ$ $-20^\circ < b < 20^\circ$	Uyaniker et al. 1999; Reich et al. 2004 (EMLS)
1.4 GHz (PI)	$\approx 1'$	$332.5^\circ > l > 325.5^\circ$ $-0.5^\circ < b < 3.5^\circ$	Gaensler et al. 2001
2.3 GHz (PI)	$10.75'$	$34^\circ > l > 10^\circ$ $b \pm 5^\circ$	Sun et al. 2014
2.4 GHz	$10.4'$	$238^\circ > l > 365^\circ$ $b \pm 5^\circ$	Duncan et al. 1995
2.4 GHz (PI)	$10.4'$	$238^\circ > l > 5^\circ$ $b \pm 5^\circ$	Duncan et al. 1997
2.7 GHz	$4.3'$	$357.4^\circ < l < 76^\circ$ $b \pm 1.5^\circ$	Reich et al. 1984
2.7 GHz (PI)	$6'$	$74^\circ > l > 4^\circ.9$ $b \pm 1.5^\circ$	Junkes et al. 1987
2.7 GHz	$4.4'$	$76^\circ > l > 358^\circ$ $b \pm 5^\circ$	Reich et al. 1990b
2.7 GHz	$4.4'$	$240^\circ > l > 76^\circ$ $b \pm 5^\circ$	Fürst et al. 1990
2.7 GHz (PI)	$4.3'$	$74^\circ > l > 4^\circ.9$ $b \pm 5^\circ$	Duncan et al. 1999
5 GHz (PI)	$9'$	$129^\circ > l > 122^\circ$ $b \pm 5^\circ$	Sun et al. 2007
5 GHz (PI)	$9'$	$230^\circ > l > 129^\circ$ $b \pm 5^\circ$	Gao et al. 2010
5 GHz (PI)	$9'$	$122^\circ > l > 60^\circ$ $b \pm 5^\circ$	Xiao et al. 2011
5 GHz (PI)	$9'$	$60^\circ > l > 10^\circ$ $b \pm 5^\circ$	Sun et al. 2011; 2014

(PI): with linear polarization data

A.2 Catalogue of radio polarization observations of nearby galaxies

In radio continuum the typical degrees of polarization are much higher than those in the other spectral ranges and further benefit comes from the development of large instruments and sensitive receivers. This is why almost all of our knowledge on interstellar magnetic fields in galaxies is based on their polarized radio emission and Faraday rotation.

A list of spiral, barred, irregular and dwarf galaxies detected in radio polarization until the year 2010 is given in Tables 5, 6, and 7. Most detections were made in the wavelength range 3 – 13 cm where Faraday depolarization is small. At $\lambda \approx 20$ cm, the polarized intensity is generally smaller by a factor of several (Fig. 3). At wavelengths longer than 20 cm, only one detection of polarized emission from spiral galaxies has been reported so far (M31).

Colour images and download links are compiled on: <http://www.mpifr-bonn.mpg.de/atlasmag>.

Table 5: Radio polarization observations and magnetic field structures of galaxies with low or moderate inclination

Galaxy	Telescope & λ (cm)	Structure	Reference
M33	E21,18,11,6,3	BSS	Buczilowski & Beck 1991
	E6,4, V21	ASS+BSS+QSS	Tabatabaei et al. 2008
M51	W21,6	Spiral	Segalovitz et al. 1976
	V21,18	Spiral	Horellou et al. 1992
	E6,3, V21,6	ASS+BSS (disk) +ASS (halo)	Neininger 1992; Berkhuijsen et al. 1997
	W21	BSS (halo)	Heald et al. 2009
	E6,4, V21,6,4	ASS+QSS (disk), +BSS (halo)	Fletcher et al. 2011
	V20L	BSS+vertical (halo)	Mao et al. 2015
	L200	<i>Not detected</i>	Mulcahy et al. 2014
M74=NGC0628	W21	Incomplete spiral	Heald et al. 2009
	E11,4, V10S	Magnetic arms	Mulcahy et al. 2017
M81	E6, V21	BSS?	Krause et al. 1989b
	E6, V21	BSS? (+ASS)	Sokoloff et al. 1992
	V21,6	Interarm fields	Schoofs 1992
M83	V21	Spiral	Sukumar & Allen 1989
	P6	Spiral	Harnett et al. 1990
	E6,3	BSS?	Neininger et al. 1991; 1993
	A13	Magnetic arms	Ehle 1995; Frick et al. 2016
	V6	Magnetic arms + \parallel bar	Frick et al. 2016
	K21	Reversal between disk and halo?	Heald et al. 2016
M101	E11,6,3	Spiral	Gräve et al. 1990
	E11,6	Spiral	Berkhuijsen et al. 2016
NGC0660	V6	\parallel polar ring +X-shape	Drzazga et al. 2011
NGC0877	V6	Spiral	Drzazga et al. 2011
NGC1097	V21,18,6,4	ASS+BSS+QSS + \parallel bar +nuclear spiral	Beck et al. 2005a
NGC1156	V21,6,4, E6,4	Patches of ordered field	Kepley et al., in prep.
NGC1365	V21,18,6,4	ASS+BSS+QSS + \parallel bar +nuclear spiral	Beck et al. 2005a
NGC1559	A13,6	\parallel bar	Beck et al. 2002
NGC1566	A21,13,6	Spiral, interarm	Ehle et al. 1996
NGC1569	W21, V6,4	Spiral, bubbles, loops	Kepley et al. 2010
NGC1672	A13,6	Spiral, interarm	Beck et al. 2002
NGC2207	V6	Spiral +radial streamers	Drzazga et al. 2011
NGC2276	V21,6	BSS?	Hummel & Beck 1995
NGC2403	E11,6	Spiral	Beck unpubl.
	W21	Diffuse	Heald et al. 2009
NGC2442	A13,6	Spiral + \parallel bar	Harnett et al. 2004
NGC2841	W21	Two arcs	Heald et al. 2009
NGC2903	E6,3, V21	Spiral	Beck, unpubl.
	W21	Spiral	Heald et al. 2009

NGC2976	V21, W21, E6,4	Distorted disk+halo field	Drzazga et al. 2016
NGC2997	V21,6,4, A13	Spiral +inner ASS?	Han et al. 1999
NGC3521	E3	Spiral, compressed	Knapik et al. 2000
NGC3627	E3	Spiral + dust lane	Soida et al. 1999
	V6,4	Anomalous arm	Soida et al. 2001
	W21	Spiral	Heald et al. 2009
	E11	Spiral	Nikiel-Wroczyński et al. 2013a
NGC3938	W21	Spiral	Heald et al. 2009
NGC4038/9	V21,6,4	tidal arm	Chyży & Beck 2004
	V10C	Regular field tidal arm	Basu et al. 2017
NGC4214	V6	<i>No ordered field</i>	Kepley et al. 2009
	E6	Fragment of a spiral	Drzazga 2008
NGC4258	W21, V21	In anomalous arms	van Albada & van der Hulst 1982
	V21,6	anomalous arms	Hummel et al. 1989
	V4, E3	nuclear jet + an. arms	Krause & Löhr 2004
NGC4414	V6,4	ASS+BSS+QSS	Soida et al. 2002
NGC4449	E6,3	opt. filaments	Klein et al. 1996
	V6,4	Spiral+radial field	Chyży et al. 2000
NGC4490/85	E6,4	Radial halo field	Knapik et al., in prep.
NGC4736	V6,4	Spiral, ASS?	Chyży & Buta 2008
	W21	Outer lobe	Heald et al. 2009
NGC5033	W21	Inner disk	Heald et al. 2009
NGC5055	E3	Spiral	Knapik et al. 2000
	W21	Spiral	Heald et al. 2009
NGC5426/7	V6	Spiral +spiral	Drzazga et al. 2011
NGC6822	E11,6,3	<i>No ordered field</i>	Chyży et al. 2003; 2011
NGC6907	V6	Spiral	Drzazga et al. 2011
NGC6946	E21,11,6,3	ASS?	Ehle & Beck 1993; Beck 2007
	V21,18,6,4	ASS+QSS	Beck 1991; 2007
	W21	ASS (halo)	Heald et al. 2009
	W21,13	ASS (disk+halo)	Williams et al. 2018
NGC7479	V21,6,4	spiral jet	Beck et al. 2002; Laine & Beck 2008
NGC7552	A6	Spiral + bar	Beck et al. 2002
	G49	Nucleus	Farnes et al. 2014a
IC10	E11,6,3	H α filament	Chyży et al. 2003; 2011
	V6	Filaments	Heesen et al. 2011a
	V6,4	Filaments, X-shaped halo	Chyży et al. 2016
IC342	E11,6	ASS	Gråve & Beck 1988
	E6, V21	ASS	Krause et al. 1989a
	E6, V21	ASS	Sokoloff et al. 1992
	E21,11,6,3	ASS	Beck 2015
	V21,6,4	Magnetic arm, helically twisted field	Beck 2015
	L200	<i>Not detected</i>	Van Eck et al. 2017
IC1613	E11,6	<i>No ordered field</i>	Chyży et al. 2011
UGC813/6	V6	-bridge	Drzazga et al. 2011
UGC12914/5	V6	bridge	Drzazga et al. 2011
Holmberg II	E11,6	<i>No ordered field</i>	Chyży et al., unpubl.
SMC	P21,13	main ridge	Haynes et al. 1986
	A21	Pan-Magellanic?	Mao et al. 2008
LMC	P21,13,6	Magn. loop near 30 Dor	Haynes et al. 1991; Klein et al. 1993
	A21	ASS	Gaensler et al. 2005
	P21, A21	filaments, even-symmetry halo field	Mao et al. 2012
Leo Triplet	E11	<i>No intergalactic field</i>	Nikiel-Wroczyński et al. 2013a
Stephan's Quintet	E4, V21,6	Intergalactic field	Nikiel-Wroczyński et al. 2013b
HCG15	E6, V21	Intergalactic field	Nikiel-Wroczyński et al. 2017
HCG44	E6, V21	Intergalactic field	Nikiel-Wroczyński et al. 2017
HCG60	E6, V21	Intergalactic field	Nikiel-Wroczyński et al. 2017
PKS1229-021	V21,6,2	BSS?	Kronberg et al. 1992
CLASS B1152+199	V20L,10S,5C	ASS?	Mao et al. 2017

Table 6: Radio polarization observations and magnetic field structures of galaxies with high inclination

Galaxy	Telescope & $\lambda(\text{cm})$	Structure	Reference
M31	E21,11,6 V21,6, 3 E11,6, V21 E3 W90	Even-symmetry ASS Spiral (inner region) Even ASS (+QSS) Ring-like Ring-like	Beck 1982; Beck et al. 1989 Beck et al. 1998; Gießübel & Beck 2014 Berkhuijsen et al. 2003; Fletcher et al. 2004 Gießübel 2012 Gießübel et al. 2013
M82	V6,4 E1 V6,3, W21	Radial halo field disk +vertical halo field Helical field in outflow	Reuter et al. 1994 Wielebinski 2006 Adebahr et al. 2017
M104	V21,6	disk +X-shaped halo field	Krause et al. 2006
NGC253	P6,3 V21,6 E6,3 E6,4, V21,6 V21,6,4	plane plane plane, halo spurs Even ASS disk field +even halo field Helical field in outflow cone	Harnett et al. 1990 Carilli et al. 1992 Beck et al. 1994 Heesen et al. 2009a; 2009b Heesen et al. 2011b
NGC660	V5C	plane	Wiegert et al. 2015
NGC891	V6 V21 E3 E4 V20L,5C	plane +halo spurs plane +halo spurs plane +tilted Even ASS disk field +X-shaped halo field X-shaped	Sukumar & Allen 1991 Hummel et al. 1991 Dumke et al. 1995 Krause 2009 Wiegert et al. 2015; Schmidt et al. 2018
NGC1808	V21,6	Halo spurs	Dahlem et al. 1990
NGC2683	V5C	plane	Wiegert et al. 2015
NGC3044	V20L,5C	X-shaped	Wiegert et al. 2015
NGC3079	V6	Extrplanar jet	Duric & Seaquist 1988
NGC3432	E6	Vertical, weak	Drzazga 2008
NGC3448	V5C	X-shaped	Wiegert et al. 2015
NGC3556	V20L,5C	-plane	Wiegert et al. 2015
NGC3628	V21 E3 E4 E11 V20L,5C	Fragments of ord. field plane plane +X-shaped halo field plane X-shaped	Reuter et al. 1991 Dumke et al. 1995 Krause, unpubl. Nikiel-Wroczyński et al. 2013a Wiegert et al. 2015
NGC3735	V20L,5C	X-shaped	Wiegert et al. 2015
NGC4013	V5C	plane	Wiegert et al. 2015
NGC4157	V20L,5C	X-shaped	Wiegert et al. 2015
NGC4217	V6 V20L,5C	X-shaped X-shaped	Soida 2005 Wiegert et al. 2015
NGC4236	E6	<i>No ordered field</i>	Chyży et al. 2007
NGC4565	V21 E3 E6,4, V6 V20L,5C	plane plane plane +X-shaped halo field plane	Sukumar & Allen 1991 Dumke et al. 1995 Krause 2009 Wiegert et al. 2015
NGC4631	V21 V6,4 V21,18 E4 E6 V6 W21 V20L,5C	-plane -plane, spurs X-shaped halo field plane +vertical central field +X-shaped halo field X-shaped plane +vertical field X-shaped X-shaped	Hummel et al. 1991 Golla & Hummel 1994 Beck 2009 Krause 2009; Mora et al. 2013 Mora et al. 2013 Irwin et al. 2012; Mora et al. 2013 Heald et al. 2009 Wiegert et al. 2015; Mora et al. 2018
NGC4656	E6	No ordered field	Chyży et al. 2007
NGC4666	V21,6 V6 V20L,5C	X-shaped X-shaped X-shaped	Dahlem et al. 1997 Soida 2005 Wiegert et al. 2015
NGC4945	P6,3	Halo spurs	Harnett et al. 1989; 1990

NGC5775	V21,6 V4	X-shaped Even ASS disk field +X-shaped halo field	Tüllmann et al. 2000 Soida et al. 2011
NGC5907	V20L,5C E6, V21 E4	X-shaped plane plane +X-shape?	Wiegert et al. 2015 Dumke 1997 Krause, unpubl.
NGC7090	A21,6	Vertical field	Heesen et al. 2016
NGC7331	E3 W21	plane X-shaped	Dumke et al. 1995 Heald et al. 2009
NGC7462	A21,6	Vertical field	Heesen et al. 2016
NGC7582	G49	Nucleus	Farnes et al. 2014a
Circinus	A21, 13	radio lobes	Elmouttie et al. 1995
IC2574	E6	<i>No ordered field</i>	Chyży et al. 2007
UGC10288	V20L,5C	Ordered field in back-ground radio galaxy	Irwin et al. 2013

Table 7: Radio polarization observations and magnetic field structures of galaxies in the Virgo cluster

Galaxy	Telescope & λ (cm)	Structure	Reference
NGC4192	E6,4 V21,6 V20L,5C	ASS? +halo field disk +inclined plane	Weżgowiec et al. 2012 Vollmer et al. 2013 Wiegert et al. 2015
NGC4254	E6,3 V21,6,4, E6,3 W21	Spiral ASS (+BSS), tidally stretched Spiral	Soida et al. 1996 Chyży 2008 Heald et al. 2009
NGC4294	V21,6	Halo field, inclined to disk	Vollmer et al. 2013
NGC4299	V21,6	Fragments of a spiral	Vollmer et al. 2013
NGC4298/ NGC4302	E6,4	disk+intergal. bridge, locally vertical	Weżgowiec et al. 2012
NGC4302	V21,6	Mostly disk	Vollmer et al. 2013
NGC4303	E6,4 V21,6	ASS? Spiral	Weżgowiec et al. 2012 Vollmer et al. 2013
NGC4321	V21,6 W21 E6,4	Spiral Spiral BSS? + bar	Vollmer et al. 2007; 2010 Heald et al. 2009 Weżgowiec et al. 2012
NGC4330	V21,6	Mostly disk	Vollmer et al. 2013
NGC4388	E6,4 V21,6 V5C	Inclined to disk disk +incl. in halo Helical field in nuclear outflow, \perp plane in wind	Weżgowiec et al. 2012 Vollmer et al. 2007; 2010 Damas-Segovia et al. 2016
NGC4396	V21,6	disk + NW tail	Vollmer et al. 2007; 2010
NGC4402	V21,6	disk in southern halo, incl. in northern halo	Vollmer et al. 2007; 2010
NGC4419	V21,6	disk +X-shaped	Vollmer et al. 2013
NGC4424	V6	X-shaped	Vollmer et al. 2013
NGC4438	E6 V6	disk, \perp outflow disk, displaced from disk in the east	Weżgowiec et al. 2007 Vollmer et al. 2007; 2010
NGC4457	V21,6	Spiral	Vollmer et al. 2013
NGC4501	E6,4 V21,6	disk, asymmetric Compressed along SW disk edge	Weżgowiec et al. 2007 Vollmer et al. 2007; 2010
NGC4522	V21,6	plane, compressed	Vollmer et al. 2004
NGC4532	V6	Huge halo field, inclined +vertical, X-shaped	Vollmer et al. 2013
NGC4535	V21,6,4 E6,4 V21,6	Spiral Spiral, asymmetric spiral arm, asymmetric	Beck et al. 2002 Weżgowiec et al. 2007; 2012 Vollmer et al. 2007; 2010
NGC4548	E4 E6	ASS? \perp bar	Weżgowiec et al. 2012 Weżgowiec et al. 2007

NGC4567/ NGC4568	V21,6	Intergal. bridge	Vollmer et al. 2013
NGC4569	E6,4	disk + outflow	Chyży et al. 2006
	W21	disk + outflow	Heald et al. 2009
	V21,6	disk + outflow	Chyży et al., in prep.
NGC4579	V21,6	bar, spiral in outer disk	Vollmer et al. 2013
NGC4654	E6,4	SW arm + gas tail	Weżgowiec et al. 2007
	V21,6	arms, bending out towards gas tail	Vollmer et al. 2007; 2010
NGC4689	V21,6	Fragments of a spiral	Vollmer et al. 2013
NGC4713	V21,6	Spiral	Vollmer et al. 2013
NGC4808	V21,6	Vertical, asymmetric	Vollmer et al. 2013

Instruments: A = Australia Telescope Compact Array, E = Effelsberg 100-m, G = Giant Metrewave Radio Telescope, K = KAT-7, L = Low Frequency Array (LOFAR), P = Parkes 64-m, V = Very Large Array, W = Westerbork Synthesis Radio Telescope

Wavelength codes: 200 = 167-250 cm, 90 = 80-95 cm, 49 = 48-50 cm, 21 = 20-22 cm, 20L = 15-30 cm (L-band), 18 = 18.0 cm, 13 = 12.5-13.4 cm, 11 = 11.1 cm, 10S = 7.5-15 cm (S-band), 6 = 5.8-6.3 cm, 5C = 4.3 – 6.0 cm (C-band), 4 = 3.6 cm, 3 = 2.8 cm, 2 = 2.0 cm, 1 = 9 mm

Field structures: ASS = axisymmetric spiral, BSS = bisymmetric spiral, QSS = quadrisymmetric spiral, MSS = multimode spiral

A.3 Links to the SKA project and its precursor and pathfinder telescopes

<http://www.skatelescope.org>
http://www.scholarpedia.org/article/Square_kilometre_array
<http://www.atnf.csiro.au/SKA>
<http://www.ska.ac.za>
<https://science.nrao.edu/facilities/vla>
<http://www.lofar.org>
<http://www.astron.nl/general/apertif/apertif>
<http://www.mwatelescope.org>

References

- Ade, P.A.R., et al., Planck Collaboration: 2015a, A&A 576, A104
 Ade, P.A.R., et al., Planck Collaboration: 2015b, arXiv:1502.01594
 Ade, P.A.R., et al., Planck Collaboration, 2016, A&A 594, A25
 Adebahr, B., Krause, M., Klein, U., et al.: 2013, A&A 555, A23
 Adebahr, B., Krause, M., Klein, U., Heald, G., Dettmar, R.-J.: 2017, A&A 608, A29
 Akahori, T., Gaensler, B.M., Ryu, D.: 2014, ApJ 790:123
 Appenzeller, I.: 1967, PASP 79, 600
 Arbutina, B., Urošević, D., Andjelić, M. M., Pavlović, M. Z., Vukotić, B.: 2012, ApJ 746, 79
 Arshakian, T.G., Beck, R., Krause, M., Sokoloff, D.: 2009, A&A 494, 21
 Arshakian, T.G., Beck, R.: 2011, MNRAS 418, 2336
 Athanassoula, E.: 1992, MNRAS 259, 345
 Axon, D.J., Ellis, R.S.: 1976, MNRAS 177, 499
 Balbus, S.A., Hawley, J.F.: 1998, Rev. Mod. Phys. 70, 1
 Basu, A., Roy, S.: 2013, MNRAS 433, 1675
 Basu, A., Roy, S., Mitra, D.: 2012, ApJ 756:141
 Basu, A., Beck, R., Schmidt, P., Roy, S.: 2015a, MNRAS 449, 3879
 Basu, A., Wadadekar, Y., Beelen, A., et al.: 2015b, ApJ 803:51
 Basu, A., Mao, S.A., Kepley, A.A., et al.: 2017, MNRAS 464, 1003
 Battaner, E., Florido, E.: 2000, Fund. Cosmic Phys. 21, 1
 Beck, A.M., Lesch, H., Dolag, K., Kotarba, H., Geng, A., Staszyszyn, F.A.: 2012, MNRAS 422, 2152
 Beck, R.: 1982, A&A 106, 121
 Beck, R.: 1991, A&A 251, 15
 Beck, R.: 2001, Sp. Sci. Rev. 99, 243
 Beck, R.: 2005, in *Cosmic Magnetic Fields*, eds. R. Wiełebinski & R. Beck, Springer, Berlin, p. 41
 Beck, R.: 2007, A&A 470, 539
 Beck, R.: 2009, Astrophys. Space Sci. 320, 77
 Beck, R.: 2015, A&A 578, A93
 Beck, R.: 2016, AARev 24:4
 Beck, R., Krause, M.: 2005, AN 326, 414
 Beck, R., Loiseau, N., Hummel, E., et al.: 1989, A&A 222, 58
 Beck, R., Carilli, C.L., Holdaway, M.A., Klein, U.: 1994, A&A 292, 409
 Beck, R., Brandenburg, A., Moss, D., Shukurov, A., Sokoloff, D.: 1996, ARAA 34, 155
 Beck, R., Berkhuijsen, E.M., Hoernes, P.: 1998, A&AS 129, 329
 Beck, R., Shoutenkov, V., Ehle, M., et al.: 2002, A&A 391, 83
 Beck, R., Shukurov, A., Sokoloff, D., Wiełebinski, R.: 2003, A&A 411, 99
 Beck, R., Fletcher, A., Shukurov, A., et al.: 2005a, A&A 444, 739
 Beck, R., Ehle, M., Fletcher, A., et al.: 2005b, in: *The Evolution of Starbursts*, eds. S. Hüttemeister et al., AIP Conf. Proc. 783, p. 216
 Beck, R., Frick, P., Stepanov, R., Sokoloff, D.: 2012, A&A 543, A113
 Beck, R., Bomans, D., Colafrancesco, S., et al.: 2015, PoS(AASKA14)094
 Behr, A.: 1961, ZfA 53, 95
 Bell, A.R.: 1978, MNRAS 182, 443
 Bell, E.F.: 2003, ApJ 586, 794
 Bell, M.R., Junklewitz, H., Enßlin, T.A.: 2011, A&A 535, A85
 Bennett, C.L., Hill, R.S., Hinshaw, G., et al.: 2003, ApJS 148, 97
 Berkhuijsen, E.M., Brouw, W.N.: 1963, BAN 17, 185
 Berkhuijsen, E.M., Horellou, C., Krause, M., et al.: 1997, A&A 318, 700
 Berkhuijsen, E.M., Beck, R., Hoernes, P.: 2003, A&A 398, 937
 Berkhuijsen, E.M., Urbanik, M., Beck, R., Han, J.L.: 2016, A&A 588, A114
 Bernardi, G., Greenhill, L.J., Mitchell, D.A., et al.: 2013, ApJ 771:105
 Bernet, M.L., Miniati, F., Lilly, S.J., et al.: 2008, Nat 454, 302
 Bernet, M.L., Miniati, F., Lilly, S.J.: 2013, ApJ 772, L28
 Beuermann, K., Kanbach, G., Berkhuijsen, E.M.: 1985, A&A 153, 17
 Blasi, P., Amato, E.: 2012, J. Cosm. Astropart. Phys., 010
 Boulares, A., Cox, D.P.: 1990, ApJ 365, 544
 Brandenburg, A., Subramanian, K.: 2005, Phys. Rep. 417, 1
 Braun, R., Heald, G., Beck, R.: 2010, A&A 514, A42
 Brentjens, M.A., de Bruyn, A.G.: 2005, A&A 441, 1217
 Brouw, W.N., Spoelstra, T.A.T.: 1976, A&AS 26, 129
 Brown, J.C., Taylor, A.R., Jackel, B.J.: 2003, ApJS 145, 213
 Brown, J.C., Haverkorn, M., Gaensler, B.M., et al.: 2007, ApJ 663, 258
 Buczylowski, U.R., Beck, R.: 1991, A&A 241, 47
 Burlaga, L.F., Ness, N.F.: 2016, ApJ 829:134
 Burn, B.J.: 1966, MNRAS 133, 67
 Caprioli, D.: 2011, J. Cosm. Astropart. Phys., 026

- Carilli, C.L., Holdaway, M.A., Ho, P.T.P., de Pree, C.G.: 1992, ApJ 399, L59
 Carretti, E., Haverkorn, M., McConnell, D., et al.: 2010, MNRAS 405, 1670
 Cecil, G., Bland-Hawthorn, J., Veilleux, S., Filippenko, A.V.: 2001, ApJ 555, 338
 Chamandy, L., Subramanian, K., Shukurov, A.: 2013, MNRAS 428, 3569
 Chamandy, L., Shukurov, A., Subramanian, K., Stoker, K.: 2014, MNRAS 443, 1867
 Chamandy, L., Shukurov, A., Subramanian, K.: 2015, MNRAS 446, L6
 Chamandy, L., Shukurov, A., Taylor, A.R.: 2016, ApJ 833:43
 Chandrasekhar, S., Fermi, E.: 1953, ApJ 118, 113
 Cho, J., Lazarian, A.: 2005, ApJ 631, 361
 Chyży, K.T.: 2008, A&A 482, 755
 Chyży, K.T., Beck, R.: 2004, A&A 417, 541
 Chyży, K.T., Buta, R.J.: 2008, ApJ 677, L17
 Chyży, K.T., Beck, R., Kohle, S., Klein, U., Urbanik, M.: 2000, A&A 356, 757
 Chyży, K.T., Knapik, J., Bomans, D.J., et al.: 2003, A&A 405, 513
 Chyży, K.T., Soida, M., Bomans, D.J., et al.: 2006, A&A 447, 465
 Chyży, K.T., Bomans, D.J., Krause, M., et al.: 2007, A&A 462, 933
 Chyży, K.T., Weżgowiec, M., Beck, R., Bomans, D.J.: 2011, A&A 529, A94
 Chyży, K.T., Drzazga, R.T., Beck, R., et al.: 2016, A&A, ApJ 819:39
 Chyży, K.T., Sridhar, S.S., Jurusik, W.: 2017, A&A 603, A121
 Colafrancesco, S., Profumo, S., Ullio, P.: 2007, Phys. Rev. D 75, 023513
 Colafrancesco, S., Regis, M., Marchegiani, P., et al.: 2015, PoS(AASKA14)100
 Condon, J.J., Helou, G., Jarrett, T.H.: 2002, AJ 123, 1881
 Crocker, R.M., Jones, D.I., Melia, F., et al.: 2010, Nat 463, 65
 Crutcher, R.M., Kazes, I., Troland, T.H.: 1987, A&A 181, 119
 Crutcher, R.M., Troland, T.H., Lazareff, B., et al.: 1999, ApJ 514, 121
 Crutcher, R.M., Hakobian, N., Troland, T.H.: 2009, ApJ 692, 844
 Crutcher, R.M., Wandelt, B., Heiles, C., Falgarone, E., Troland, T.H.: 2010, ApJ 725, 466
 Dahlem, M., Aalto, S., Klein, U., et al.: 1990, A&A 240, 237
 Dahlem, M., Lisenfeld, U., Golla, G.: 1995, ApJ 444, 119
 Dahlem, M., Petr, M.G., Lehnert, M.D., Heckman, T.M., Ehle, M.: 1997, A&A 320, 731
 Damas-Segovia, A., Beck, R., Vollmer, B., et al.: 2016, ApJ 824:30
 Davis, L.J., Greenstein, J.L.: 1951, ApJ 114, 206
 de Avillez, M.A., Breitschwerdt, D.: 2005, A&A 436, 585
 Dobbs, C.L., Price, D.J.: 2008, MNRAS 383, 497
 Dobbs, C.L., Price, D.J., Pettitt, A.R., Bate, M.R., Tricco, T.S.: 2016, MNRAS 461, 4482
 Dobler, G., Draine, B., Finkenbeiner, D.P.: 2009, ApJ 699, 1374
 Draine, B.T., Lazarian, A.: 1998, ApJ 494, L19
 Drzazga, R.T.: 2008, M.Sc. Thesis, Jagiellonian Univ. Kraków
 Drzazga, R.T., Chyży, K.T., Jurusik, W., Wiórkiewicz, K.: 2011, A&A 533, A22
 Drzazga, R.T., Chyży, K.T., Heald, G.H., Elstner, D., Gallagher III, J.S.: 2016, A&A 589, A12
 Dumas, G., Schinnerer, E., Tabatabaei, F.S., et al.: 2011, AJ 141:41
 Dumke, M.: 1997, PhD Thesis, Univ. of Bonn
 Dumke, M., Krause, M.: 1998, in *The Local Bubble and Beyond*, eds. D. Breitschwerdt et al., Springer, Berlin, p. 555
 Dumke, M., Krause, M., Wielebinski, R., Klein, U.: 1995, A&A 302, 691
 Duncan, A.R., Haynes, R.F., Jones, K.L., Stewart, R.T.: 1995, MNRAS 277, 36
 Duncan, A.R., Haynes, R.F., Jones, K.L., Stewart, R.T.: 1997, MNRAS 291, 279
 Duncan, A.R., Reich, P., Reich, W., Fürst, E.: 1999, A&A 350, 447
 Duric, N., Seaquist, E.R.: 1988, ApJ 326, 574
 Durrer, R., Neronov, A.: 2013, A&A Rev 21, 62
 Eatough, R.P., Falcke, H., Karuppusamy, R., et al.: 2013, Nat 501, 391
 Ehle, M.: 1995, Ph.D. Thesis, Univ. of Bonn
 Ehle, M., Beck, R.: 1993, A&A 273, 45
 Ehle, M., Beck, R., Haynes, R.F., et al.: 1996, A&A 306, 73
 Ellis, R.S., Axon, D.J.: 1978, Ap&SS 54, 425
 Elmouttie, M., Haynes, R.F., Jones, K.L., et al.: 1995, MNRAS 275, L53
 Elstner, D., Beck, R., Gressel, O.: 2014, A&A 568, A104
 Elvius, A.: 1962, Bull. Lowell Obs. 5, 281
 Fabbiano, G., Klein, U., Trinchieri, G., Wielebinski, R.: 1987, ApJ 312, 111
 Farnes, J.S., Green, D.A., Kantharia, N.G.: 2014a, MNRAS 437, 3236
 Farnes, J.S., O'Sullivan, S.P., Corrigan, M.E., Gaensler, B.M.: 2014b, ApJ 795:63
 Farnes, J.S., Rudnick, L., Gaensler, B.M., et al.: 2017, ApJ 841:67
 Farrar, G.R.: 2016, Proc IAU 29B, 723
 Fauvet, L., Macías-Pérez, J.F., Aumont, J., et al.: 2011, A&A 526:145
 Fendt, Ch., Beck, R., Lesch, H., Neininger, N.: 1996, A&A 308, 713
 Fendt, Ch., Beck, R., Neininger, N.: 1998, A&A 335, 123
 Feretti, L., Giovannini, G., Govoni, F., Murgia, M.: 2012, A&A Rev 20:54
 Fermi, E.: 1949, Phys. Rev. 75, 1169

- Ferrière, K.: 2001, *Rev. Mod. Phys.* 73, 1031
- Ferrière, K.: 2009, *A&A* 505, 1183
- Ferrière, K., Terral, P.: 2014, *A&A* 561, A100
- Fiebig, D., Güsten, R.: 1989, *A&A* 214, 333
- Fish, V.L., Reid, M.J., Argon, A.L., Menten, K.M.: 2003, *ApJ* 596, 328
- Fletcher, A.: 2010, in *The Dynamic Interstellar Medium*, eds. R. Kothes et al., ASP Conf. Ser., Vol. 438, p. 197
- Fletcher, A., Berkhuijsen, E.M., Beck, R., Shukurov, A.: 2004, *A&A* 414, 53
- Fletcher, A., Beck, R., Shukurov, A., Berkhuijsen, E.M., Horellou, C.: 2011, *MNRAS* 412, 2396
- Fosalba, P., Lazarian, A., Prunet, S., Tauber, J.A.: 2002, *ApJ* 546, 762
- Frick, P., Sokoloff, D., Stepanov, R., Beck, R.: 2011, *MNRAS* 414, 2540
- Frick, P., Stepanov, R., Beck, R., et al.: 2016, *A&A* 585, A21
- Fürst, E., Reich, W., Reich, P., Reif, K.: 1990, *A&AS* 85, 691
- Gaensler, B., M., Dickey, J.M., McClure-Griffiths, N.M., et al.: 2001, *ApJ* 549, 959
- Gaensler, B.M., Haverkorn, M., Staveley-Smith, L., et al.: 2005, *Science* 307, 1610
- Gaensler, B.M., Haverkorn, M., Burkhart, B., et al.: 2011, *Nat* 478, 214
- Gao, X.Y., Reich, W., Han, J.L., et al.: 2010, *A&A* 515, A64
- Gent, F.A., Shukurov, A., Sarson, G.R., Fletcher, A., Mantere, M.J.: 2013, *MNRAS* 430, L40
- Georgelin, Y.M., Georgelin, Y.P.: 1976, *ApJ* 49, 57
- Giacinti, G., Kachelrieß, M., Semikoz, D.V.: 2017, arXiv:1710.08205
- Gießübel, R.: 2012, Ph.D. thesis, University of Cologne
- Gießübel, R., Beck, R.: 2014, *A&A* 571, A61
- Gießübel, R., Heald, G., Beck, R., Arshakian, T.G.: 2013, *A&A* 559, A27
- Goldreich, P., Kylafis, N.D.: 1981, *ApJ* 243, L75
- Golla, G., Hummel, E.: 1994, *A&A* 284, 777
- Gomes, A.L., Magalhães, A.M., Pereyra, A., Rodrigues, C.V.: 2015, *ApJ* 806:94
- Gräve, R., Beck, R.: 1988, *A&A* 192, 66
- Gräve, R., Klein, U., Wielebinski, R.: 1990, *A&A* 238, 39
- Gray, A., Landecker, T.L., Dewdney, P.E., Taylor, A.R.: 1998, *Nat* 393, 660
- Greaves, J.S., Holland, W.S., Jenness, T., Hawarden, T.G.: 2000, *Nat* 404, 732
- Greenhill, L.J., Jiang, D.R., Moran, J.M., et al.: 1995, *ApJ* 440, 619
- Gressel, O., Elstner, D., Ziegler, U.: 2013, *A&A* 560, A93
- Guzmán, A.E., May, J., Alvarez, H., Maeda, K.: 2011, *A&A* 525, A138
- Han, J.L.: 2008, *IAUS* 242, 55
- Han, J.L.: 2017, *ARAA* 55, 111
- Han, J.L., Qiao, G.J.: 1994, *A&A* 288, 759
- Han, J.L., Zhang, J.S.: 2007, *A&A* 464, 609
- Han, J.L., Beck, R., Berkhuijsen, E.M.: 1998, *A&A* 335, 1117
- Han, J.L., Beck, R., Ehle, M., Haynes, R.F., Wielebinski, R.: 1999, *A&A* 348, 405
- Han, J.L., Manchester, R.N., Lyne, A.G., Qiao, G.J., van Straten, W.: 2006, *ApJ* 642, 868
- Han, J.L., Demorest, P., van Straten, W., Lyne, A.G.: 2009, *ApJS* 181, 557
- Han, J.L., van Straten, W., Lazio, T.J.W., et al.: 2015, *PoS(AASKA14)041*
- Han, J.L., Manchester, R.N., van Straten, W., Demorest, P.: 2018, *ApJS* 234:11
- Hanasz, M., Otmianowska-Mazur, K., Kowal, G., Lesch, H.: 2009, *A&A* 498, 335
- Hanayama, H., Takahashi, K., Kotake, K., et al.: 2005, *ApJ* 633, 941
- Harnett, J.I., Haynes, R.F., Klein, U., Wielebinski, R.: 1989, *A&A* 216, 39
- Harnett, J.I., Haynes, R.F., Wielebinski, R., Klein, U.: 1990, *Proc. Astr. Soc. Australia* 8, 257
- Harnett, J., Ehle, M., Fletcher, A., et al.: 2004, *A&A* 421, 571
- Haslam, C.G.T., Salter, C.J., Stoffel, H., Wilson, W.E.: 1982, *A&AS* 47, 1
- Haverkorn, M.: 2015, in *Magnetic Fields in Diffuse Media*, Astrophysics and Space Science Library, Vol. 407, eds. A. Lazarian, E. M. de Gouveia Dal Pino & C. Melioli, p. 483
- Haverkorn, M., Katgert, P., de Bruyn, A.G.: 2003, *A&A* 403, 1031, and 403, 1045
- Haverkorn, M., Katgert, P., de Bruyn, A.G.: 2004, *A&A* 427, 169, and 427, 549
- Haverkorn, M., Gaensler, B.M., McClure-Griffiths, N.M., et al.: 2006, *ApJS* 167, 230
- Haverkorn, M., Akahori, T., Carretti, E., et al.: 2015, *PoS(AASKA14)096*
- Haynes, R.F., Klein, U., Wielebinski, R., Murray, J.D.: 1986, *A&A* 159, 22
- Haynes, R.F., Klein, U., Wayte, S.R., et al.: 1991, *A&A* 252, 475
- Heald, G.: 2015, in *Magnetic Fields in Diffuse Media*, Astrophysics and Space Science Library, Vol. 407, eds. A. Lazarian, E. M. de Gouveia Dal Pino & C. Melioli, p. 41
- Heald, G., Braun, R., Edmonds, R.: 2009, *A&A* 503, 409
- Heald, G., de Blok, W.J.G., Lucero, D., et al.: 2016, *MNRAS* 462, 1238
- Heesen, V., Beck, R., Krause, M., Dettmar, R.-J.: 2009a, *A&A* 494, 563
- Heesen, V., Krause, M., Beck, R., Dettmar, R.-J.: 2009b, *A&A* 506, 1123
- Heesen, V., Rau, U., Rupen, M.P., Brinks, E., Hunter, D.A.: 2011a, *ApJ* 739, L23
- Heesen, V., Beck, R., Krause, M., Dettmar, R.-J.: 2011b, *A&A* 535, A79
- Heesen, V., Brinks, E., Leroy, A.K., et al.: 2014, *AJ* 147:103
- Heesen, V., Dettmar, R.-J., Krause, M., Beck, R., Stein, Y.: 2016, *MNRAS* 458, 332
- Heesen, V., Krause, M., Beck, R., et al.: 2018, *MNRAS*, in press
- Heiles, C.: 2000, *AJ* 119, 923

- Heiles, C., Crutcher, R.: 2005, in *Cosmic Magnetic Fields*, eds. R. Wielebinski & R. Beck, Springer, Berlin, p. 137
- Henriksen, R.N., Irwin, J.A.: 2016, MNRAS 458, 4210
- Hildebrand, R.H., Kirby, L., Dotson, J.L., et al.: 2009, ApJ 696, 567
- Hiltner, W.A.: 1958, ApJ 128, 9
- Hinshaw, G., Weiland, J.L., Hill, R.S., et al.: 2009, ApJS 180, 225
- Hoang, T., Lazarian, A.: 2008, MNRAS 388, 117
- Hoang, T., Lazarian, A.: 2014, MNRAS 438, 680
- Horellou, C., Beck, R., Berkhuijsen, E.M., Krause, M., Klein, U.: 1992, A&A 265, 417
- Houde, M., Vaillancourt, J.E., Hildebrand, R.H., Chitsazzadeh, S., Kirby, L.: 2009, ApJ 706, 1504
- Houde, M., Fletcher, A., Beck, R., et al.: 2013, ApJ 766:49
- Hummel, E., Beck, R.: 1995, A&A 303, 691
- Hummel, E., Krause, M., Lesch, H.: 1989, A&A 211, 266
- Hummel, E., Beck, R., Dahlem, M.: 1991, A&A 248, 23
- Iacobelli, M., Haverkorn, M., Orrú, E., et al.: 2013, A&A 558, A72
- Iacobelli, M., Burkhart, B., Haverkorn, M., et al.: 2014, A&A 566, A5
- Ideguchi, S., Tashiro, Y., Akahori, T., Takahashi, K., Ryu, D.: 2014, ApJ 792:51
- Ideguchi, S., Tashiro, Y., Akahori, T., Takahashi, K., Ryu, D.: 2017, ApJ 843:146
- Irwin, J., Beck, R., Benjamin, R.A., et al.: 2012, AJ 144:44
- Irwin, J., Krause, M., English, J., et al.: 2013, AJ 146:164
- Jaffe, T.R., Leahy, J.P., Banday, A.J., et al.: 2010, MNRAS 401, 1013
- Jaffe, T.R., Ferrière, K.M., Banday, A.J., et al.: 2013, MNRAS 431, 683
- Jansson, R., Farrar, G.R.: 2012a, ApJ 757:14
- Jansson, R., Farrar, G.R.: 2012b, ApJ 761:L11
- Jelić, V., de Bruyn, A.G., Mevius, M., et al.: 2014, A&A 568, A101
- Jelić, V., de Bruyn, A.G., Pandey, V.N., et al.: 2015, A&A 583, A137
- Johnston-Hollitt, M., Hollitt, C.P., Ekers, R.: 2003, in *The Magnetized Interstellar Medium*, eds. B. Uyaniker et al., Copernicus, Katlenburg, p. 13
- Johnston-Hollitt, M., Govoni, F., Beck, R., et al.: 2015, PoS(AASKA14)092
- Jonas, J.L., Baart, E.E., Nicolson, G.D.: 1998, MNRAS 297, 977
- Jones, T.J.: 1989, AJ 98, 2062
- Jones, T.J.: 2000, AJ 120, 2920
- Jones, A., Wang, L., Krisciunas, K., Freeland, E.: 2012, ApJ 748:17
- Junkes, N., Fürst, E., Reich, W.: 1987, A&A 69, 451
- Kalberla, P.M.W., Kerp, J.: 2016, A&A 595, A37
- Kalberla, P.N.W., Kerp, J., Haud, U., Haverkorn, M.: 2017, A&A 607, A15
- Kallas, E., Reich, W.: 1980, A&AS 42, 227
- Kepley, A.A., Mühle, S., Everett, J., et al.: 2010, ApJ 712, 536
- Kiepenheuer, K.O.: 1950, Phys. Rev. 79, 738
- King, O.G., Jones, M.E., Blackhurst, E.J., et al.: 2014, MNRAS 438, 2426
- Klein, U., Fletcher, A.: 2015, *Galactic and Intergalactic Magnetic Fields*. Springer, Berlin
- Klein, U., Weiland, H., Brinks, E.: 1991, A&A 246, 323
- Klein, U., Haynes, R.F., Wielebinski, R., Meinert, D.: 1993, A&A 271, 402
- Klein, U., Hummel, E., Bomans, D.J., Hopp, U.: 1996, A&A 313, 396
- Knapik, J., Soida, M., Dettmar, R.-J., Beck, R., Urbanik, M.: 2000, A&A 362, 910
- Kogut, A., Dunkley, J., Bennett, C.L., et al.: 2007, ApJ 665, 355
- Krause, F., Beck, R.: 1998, A&A 335, 789
- Krause, M.: 1990, in *Galactic and Intergalactic Magnetic Fields*, ed. R. Beck et al., Kluwer, Dordrecht, p. 187
- Krause, M.: 2009, Rev. Mex. AA 36, 25
- Krause, M., Löhr, A.: 2004, A&A 420, 115
- Krause, M., Hummel, E., Beck, R.: 1989a, A&A 217, 4
- Krause, M., Beck, R., Hummel, E.: 1989b, A&A 217, 17
- Krause, M., Wielebinski, R., Dumke, M.: 2006, A&A 448, 133
- Krause, M., Irwin, I., Wiegert, T., et al.: 2018, A&A, in press
- Kronberg, P.P.: 2016, *Cosmic Magnetic Fields*. Cambridge University Press, Cambridge
- Kronberg, P.P., Perry, J.J., Zukowski, E.L.H.: 1992, ApJ 387, 528
- Kronberg, P.P., Bernet, M.L., Miniati, F., et al.: 2008, ApJ 676, 70
- Kulpa-Dybeł, K., Otmianowska-Mazur, K., Kulesza-Żydzik, B., et al.: 2011, ApJ 733:L18
- Kulsrud, R.M., Cen, R., Ostriker, J.P., Ryu, D.: 1997, ApJ 480, 481
- Lacki, B.C., Beck, R.: 2013, MNRAS 430, 3171
- Lacki, B.C., Thompson, T.A., Quataert, E.: 2010, ApJ 717, 1
- Laine, S., Beck, R.: 2008, ApJ 673, 128
- Landecker, T.L., Wielebinski, R.: 1970, Aust. J. Phys. Astrophys. Suppl. 16, 1
- Landecker, T.L., Reich, W., Reid, R.I., et al.: 2010, A&A 520, A80
- Lazar, M., Schlickeiser, R., Wielebinski, R., Poedts, S.: 2009, ApJ 693, 1133
- Lazarian, A., de Gouveia Dal Pino, E.M., Melioli, C.: 2015, *Magnetic Fields in Diffuse Media*, Springer, Berlin
- Lesch, H., Schlickeiser, R., Crusius, A.: 1988, A&A 200, L9
- Levin, S.M., Langer, W.D., Kuiper, T.B.H., et al.: 2000, AAS 197, 1016
- Li, H.-B., Henning, T.: 2011, Nat 479, 499

- Li, H., Dowell, C.D., Goodman, A., Hildebrand, R., Novak, G.: 2009, ApJ 704, 891
- Li, J.-T., Beck, R., Dettmar, R.-J., et al.: 2016, MNRAS 456, 1723
- Lisenfeld, U., Völk, H.J., Xu, C.: 1996, A&A 314, 745
- Lou, Y.-Q., Han, J.L., Fan, Z.: 1999, MNRAS 308, L1
- Mao, S.A., Gaensler, B.M., Stanimirović, S., et al.: 2008, ApJ 688, 1029
- Mao, S.A., Gaensler, B.M., Haverkorn, M., et al.: 2010, ApJ 714, 1170
- Mao, S.A., McClure-Griffiths, N.M., Gaensler, B.M., et al.: 2012, ApJ 759:25
- Mao, S.A., Zweibel, E., Fletcher, A., et al.: 2015, ApJ 800:92
- Mao, S.A., Carilli, C., Gaensler, B.M., et al.: 2017, Nat Astr 1, 612
- Machida, M., Nakamura, K.E., Kudoh, T., et al.: 2013, ApJ 764:81
- Mathewson, D.S., Milne, D.K.: 1965, Aust. J. Phys. 18, 635
- Mathewson, D.S., Ford, V.L.: 1970a, Mem. RAS 74, 139
- Mathewson, D.S., Ford, V.L.: 1970b, ApJ 160, L43
- McBride, J., Heiles, C.: 2013, ApJ 763:8
- Men, H., Ferrière, K., Han, J.L.: 2008, A&A 486, 819
- Mikhailov, E., Kasparova, A., Moss, D., et al.: 2014, A&A 568, A66
- Mitra, D., Wielebinski, R., Kramer, M., Jessner, A.: 2003, A&A 398, 993
- Montgomery, J.D., Clemens, D.P.: 2014, ApJ 786:41
- Mora, S.C., Krause, M.: 2013, A&A 560, A42
- Mora, S.C., Krause, M., Basu, A., et al.: 2018, A&A, in prep.
- Moss, D., Shukurov, A.: 1996, MNRAS 279, 229
- Moss, D., Shukurov, A., Sokoloff, D., et al.: 2001, A&A 380, 55
- Moss, D., Sokoloff, D., Beck, R., Krause, M.: 2010, MNRAS 407, A61
- Moss, D., Stepanov, R., Arshakian, T.G., et al.: 2012, A&A 537, A68
- Moss, D., Beck, R., Sokoloff, D., et al.: 2013, A&A 556, A147
- Moss, D., Stepanov, R., Krause, M., et al.: 2015, A&A 578, A94
- Mouschovias, T.Ch., Tassis, K.: 2009, MNRAS 400, L15
- Mulcahy, D.D., Horneffer, A., Beck, R., et al.: 2014, A&A 568, A74
- Mulcahy, D.D., Beck, R., Heald, G.H.: 2017, A&A 600, A6
- Mulcahy, D.D., Horneffer, A., Beck, R., et al.: 2018, A&A, in press
- Murphy, E.J.: 2009, ApJ 706, 482
- Neininger, N.: 1992, A&A 263, 30
- Neininger, N.: Klein, U., Beck, R., Wielebinski, R.: 1991, Nat 352, 781
- Neininger, N., Beck, R., Sukumar, S., Allen, R.J.: 1993, A&A 274, 687
- Neronov, A., Vovk, I.: 2010, Science 328, 73
- Nikiel-Wroczyński, B., Soida, M., Urbanik, M., et al.: 2013a, A&A 553, A4
- Nikiel-Wroczyński, B., Soida, M., Urbanik, M., et al.: 2013b, MNRAS 435, 149
- Nikiel-Wroczyński, B., Urbanik, M., Soida, M., et al.: 2017, A&A 603, A97
- Niklas, S.: 1995, Ph.D. thesis, University of Bonn
- Niklas, S., Beck, R.: 1997, A&A 320, 54
- Nishiyama, S., Hatano, H., Tamura, M., et al.: 2010, ApJ 722, L23
- Nord, M.E., Lazio, T.J.W., Kassim, N.E., et al.: 2004, AJ 128, 1646
- Nota, T., Katgert, P.: 2010, A&A 513, A65
- Noutsos, A., Johnston, S., Kramer, M., Karastergiou, A.: 2008, MNRAS 386, 1881
- Novak, G., Dotson, J.L., Dowell, C.D., et al.: 2000, ApJ 529, 241
- Nyland, K., Young, L.M., Wrobel, J.M., et al.: 2017, MNRAS 464, 1029
- Oppermann, N., Junklewitz, H., Robbers, G., et al.: 2012, A&A 542, A93
- Ordog, A., Brown, J.C., Kothes, R., Landecker, T.L.: 2017, A&A 603, A15
- Otmianowska-Mazur, K., Elstner, D., Soida, M., Urbanik, M.: 2002, A&A 384, 48
- Pakmor, R., Marinacci, F., Springel, V.: 2014, ApJ 783:L20
- Pakmor, R., Gómez, F.A., Grand, R.J.J., et al.: 2017, MNRAS 469, 3185
- Parker, E.N.: 1979, *Cosmical Magnetic Fields*, Clarendon Press, Oxford
- Patrikeev, I., Fletcher, A., Stepanov, R., et al.: 2006, A&A 458, 441
- Pavel, M.D., Clemens, D.P., Pinnick, A.F.: 2012, ApJ 749:71
- Phillips, S., Kearsy, S., Osbourne, J.L., et al.: 1981, A&A 98, 286
- Prouza, M., Šmída, R.: 2003, A&A 410, 1
- Rand, R.J., Kulkarni, S.R.: 1989, ApJ 343, 760
- Reber, G.: 1944, ApJ 100, 279
- Rees, M.J.: 2005, in *Cosmic Magnetic Fields*, eds. R. Wielebinski & R. Beck, Springer, Berlin, p. 1
- Reich, W.: 1982, A&AS 48, 219
- Reich, W.: 2003, A&A 401, 1023
- Reich, W.: 2006, *Cosmic Polarization*, ed. Roberto Fabri, Research Signpost, p. 91
- Reich, W., Reich, P.: 1986, A&AS 63, 205
- Reich, W., Fürst, E., Steffen, P., et al.: 1984, A&AS 58, 197
- Reich, W., Sofue, Y., Wielebinski, R., Seiradakis, J.H.: 1988, A&A 191, 303
- Reich, W., Reich, P., Fürst, E.: 1990a, A&AS 83, 539
- Reich, W., Fürst, E., Reich, P., Reif, K.: 1990b, A&AS 85, 633
- Reich, P., Reich, W., Fürst, E.: 1997, A&AS 126, 413

- Reich, P., Testori, J., Reich, W.: 2001, A&A 376, 861
- Reich, W., Fürst, E., Reich, P., et al.: 2004, in *The Magnetized Interstellar Medium*, eds. B. Uyaniker et al., Copernicus, Katlenburg, p. 51
- Reif, K., Reich, W., Steffen, P., et al.: 1987, Mitt. AG 70, 419
- Reuter, H.-P., Krause, M., Wielebinski, R., Lesch, H.: 1991, A&A 248, 12
- Reuter, H.-P., Klein, U., Lesch, H., Wielebinski, R., Kronberg, P.P.: 1992, A&A 256, 10
- Reuter, H.-P., Klein, U., Lesch, H., Wielebinski, R., Kronberg, P.P.: 1994, A&A 282, 724
- Rieder, M., Teyssier, R.: 2016, MNRAS 457, 1722
- Rieder, M., Teyssier, R.: 2017, MNRAS 471, 2674
- Robitaille, J.-F., Scaife, A.M.M., Carretti, E., et al.: 2017, MNRAS 468, 2957
- Rodrigues, L.F.S., Shukurov, A., Fletcher, A., Baugh, C.M.: 2015, MNRAS 450, 3472
- Roy, S., Prameh Rao, A., Subrahmanyam, R.: 2008, A&A 478, 435
- Rudnick, L., Brown, S.: 2009, AJ 137, 145
- Rüdiger, G., Kitchatinov, L.L., Hollerbach, R.: 2013, *Magnetic Processes in Astrophysics*, Wiley, Weinheim
- Ruiz-Granados, B., Rubiño-Martín, J.A., Florido, E., Battaner, E.: 2010, ApJ 723, L44
- Ruzmaikin, A.A., Shukurov, A.M., Sokoloff, D.D.: 1988, *Magnetic Fields of Galaxies*, Kluwer, Dordrecht
- Scarrott, S.M., Ward-Thompson, D., Warren-Smith, R.F.: 1987, MNRAS 224, 299
- Scarrott, S.M., Rolph, C.D., Semple, D.P.: 1990, in *Galactic and Intergalactic Magnetic Fields*, eds. R. Beck et al., Kluwer, Dordrecht, p. 245
- Scarrott, S.M., Rolph, C.D., Wolstencroft, R.W., Tadhunter, C.N.: 1991, MNRAS 249, 16P
- Schleicher, D.R.G., Miniati, F.: 2011, MNRAS 418, L143
- Schleicher, D.R.G., Beck, R.: 2013, A&A 556, A142
- Schleicher, D.R.G., Beck, R.: 2016, A&A 593, A77
- Schleicher, D.R.G., Banerjee, R., Sur, S., et al.: 2010, A&A 522, A115
- Schlickeiser, R.: 2012, Phys. Rev. Lett. 109, 261101
- Schlickeiser, R., Felten, T.: 2013, ApJ 778:39
- Schmidt, P., Krause, M., Heesen, V., et al.: 2018, A&A, in prep.
- Schmidt, Th.: 1976, A&A Suppl. 24, 357
- Schnitzeler, D.H.F.M.: 2010, MNRAS 409, 99
- Schnitzeler, D.H.F.M., Katgert, P., de Bruyn, A.G.: 2009, A&A 494, 611
- Schnitzeler, D.H.F.M., Eatough, R.P., Ferrière, K., et al.: 2016, MNRAS 459, 3005
- Schober, J., Schleicher, D.R.G., Klessen, R.S.: 2016, ApJ 827:109
- Schoofs, S.: 1992, Diploma Thesis, University of Bonn
- Segalovitz, A., Shane, W.W., de Bruyn, A.G.: 1976, Nat 264, 222
- Seiradakis, J.H., Lasenby, A.N., Yusef-Zadeh, F., et al.: 1985, Nat 317, 697
- Shukurov, A.: 2005, in *Cosmic Magnetic Fields*, eds. R. Wielebinski & R. Beck, Springer, Berlin, p. 113
- Siejkowski, H., Otmianowska-Mazur, K., Soida, M., Bomans, D.J., Hanasz, M.: 2014, A&A 562, A136
- Simard-Normandin, M., Kronberg, P.P.: 1980, ApJ 242, 74
- Sobey, C., and the LOFAR and MWA collaborations: 2017, arXiv:1712.06258
- Soida, M.: 2005, in *The Magnetized Plasma in Galaxy Evolution*, eds. K.T. Chyży et al., Jagiellonian Univ., Kraków, p. 185
- Soida, M., Urbanik, M., Beck, R.: 1996, A&A 312, 409
- Soida, M., Urbanik, M., Beck, R., Wielebinski, R.: 1999, A&A 345, 461
- Soida, M., Urbanik, M., Beck, R., Wielebinski, R., Balkowski, C.: 2001, A&A 378, 40
- Soida, M., Beck, R., Urbanik, M., Braine, J.: 2002, A&A 394, 47
- Soida, M., Krause, M., Dettmar, R.-J., Urbanik, M.: 2011, A&A 531, A127
- Sokoloff, D., Shukurov, A., Krause, M.: 1992, A&A 264, 396
- Sokoloff, D., Bykov, A.A., Shukurov, A., et al.: 1998, MNRAS 299, 189, and MNRAS 303, 207 (Erratum)
- Spekkens, K., Mason, B. S., Aguirre, J. E., Nhan, B.: 2013, ApJ 773, 61
- Steininger, T., Enßlin, T.A., Greiner, M., et al.: 2018, arXiv:1801.04341
- Stepanov, R., Frick, P., Shukurov, A., Sokoloff, D.: 2002, A&A 391, 361
- Stepanov, R., Arshakian, T.G., Beck, R., Frick, P., Krause, M.: 2008, A&A 480, 45
- Stil, J.M., Taylor, A.R., Dickey, J.M., et al.: 2006, AJ 132, 1158
- Stil, J.M., Krause, M., Beck, R., Taylor, R.: 2009, ApJ 693, 1392
- Stix, M.: 1975, A&A 42, 85
- Sukumar, S., Allen, R.J.: 1989, Nat 340, 537
- Sukumar, S., Allen, R.J.: 1991, ApJ 382, 100
- Sun, X.H., Reich, W.: 2010, Research in Astron. Astrophys. 10, 1287
- Sun, X.H., Han, J.L., Reich, W., et al.: 2007, A&A 463, 993
- Sun, X.H., Reich, W., Waelkens, A., Enßlin, T.A.: 2008, A&A 477, 573
- Sun, X.H., Reich, W., Han, J.L., et al.: 2011, A&A 527, A74
- Sun, X.H., Gaensler, B.M., Carretti, E., et al.: 2014, MNRAS 437, 2936
- Sun, X.H., Landecker, T.L., Gaensler, B.M., et al.: 2015, ApJ 811:40
- Sur, S., Shukurov, A., Subramanian, K.: 2007, MNRAS 377, 874
- Tabatabaei, F.S., Beck, R., Krügel, E., et al.: 2007, A&A 475, 133
- Tabatabaei, F.S., Krause, M., Fletcher, A., Beck, R.: 2008, A&A 490, 1005
- Tabatabaei, F.S., Schinnerer, E., Murphy, E.J., et al.: 2013a, A&A 552, A19
- Tabatabaei, F.S., Berkhuijsen, E.M., Frick, P., Beck, R., Schinnerer, E.: 2013b, A&A 557, A129

- Tabatabaei, F.S., Martinsson, T.P.K., Knapen, J.H., et al.: 2016, ApJ 818:L10
- Tamburro, D., Rix, H.-W., Leroy, A.K., et al.: 2009, AJ 137, 4424
- Tang, Y.-W., Ho, P.T.P., Koch, P.M., et al.: 2009, ApJ 700, 251
- Taylor, A.R., Gibson, S.J., Peracaula, M., et al.: 2003, AJ 125, 3145
- Taylor, A.R., Stil, J.M., Sunstrum, C.: 2009, ApJ 702, 1230
- Terral, P., Ferrière, K.: 2017, A&A 600, A29
- Testori, J.C., Reich, P., Reich, W.: 2008, A&A 484, 733
- Thompson, T.A., Quataert, E., Waxman, E., Murray, N., Martin, C.L.: 2006, ApJ 645, 186
- Thum, C., Morris, D.: 1999, A&A 344, 923
- Tribble, P.C.: 1991, MNRAS 250, 726
- Tüllmann, R., Dettmar, R.-J., Soida, M., Urbanik, M., Rossa, J.: 2000, A&A 364, L36
- Tüllmann, R., Breitschwerdt, D., Rossa, J., Pietsch, W., Dettmar, R.-J.: 2006, A&A 457, 779
- Urbanik, M., Elstner, D., Beck, R.: 1997, A&A 326, 465
- Uyaniker, B., Fürst, E., Reich, W., et al.: 1999, A&AS 138, 31
- Vacca, V., Oppermann, N., Enßlin, T., et al.: 2016, A&A 591, A13
- Vallée, J.P.: 1996, A&A 308, 433
- van Albada, G.D., van der Hulst, J.M.: 1982, A&A 115, 263
- Van Eck, C.L., Brown, J.C., Stil, J.M., et al.: 2011, ApJ 728:97
- Van Eck, C.L., Brown, J.C., Shukurov, A., Fletcher, A.: 2015, ApJ 799:35
- Van Eck, C.L., Haverkorn, M., Alves, M.I.R., et al.: 2017, A&A 597, A98
- Verschuur, G.L.: 1968, Phys. Rev. Lett. 21, 775
- Vishniac, E.T., Lazarian, A., Cho, J.: 2003, in *Turbulence and Magnetic Fields in Astrophysics*, eds. E. Falgarone & T. Passot, Springer, Berlin, p. 376
- Vollmer, B., Beck, R., Kenney, J.D.P., van Gorkum, J.H.: 2004, AJ 127, 3375
- Vollmer, B., Soida, M., Beck, R., et al.: 2007, A&A 464, L37
- Vollmer, B., Soida, M., Chung, A., et al.: 2010, A&A 512, A36
- Vollmer, B., Soida, M., Beck, R., et al.: 2013, A&A 553, A116
- Webber, W.R., Simpson, G.A., Cane, H.V.: 1980, ApJ 236, 448
- West, J.L., Safi-Harb, S., Jaffe, T., et al.: 2016, A&A 587, A148
- Weżgowiec, M., Urbanik, M., Vollmer, B., et al.: 2007, A&A 471, 93
- Weżgowiec, M., Urbanik, M., Beck, R., et al.: 2012, A&A 545, A69
- Weżgowiec, M., Ehle, M., Beck, R.: 2016, A&A 585, A3
- Widrow, L.M.: 2002, Rev Mod Phys 74, 775
- Wiegert, T., Irwin, J., Miskolczi, A., et al.: 2015, AJ 150:81
- Wielebinski, R.: 2006, Astron. Nachr. 327, 510
- Wielebinski, R.: 2012, JAHH 15, 76
- Wielebinski, R., Shakeshaft, J.R.: 1964, MNRAS 128, 19
- Wielebinski, R., Beck, R.: 2005, *Cosmic Magnetic Fields*, Springer, Berlin
- Wielebinski, R., Shakeshaft, J.R., Pauliny-Toth, I.I.K.: 1962, The Observatory 82, 158
- Wielebinski, R., Reich, W., Han, J.L., Sun, X.H.: 2008, ASP Conf. Ser. 396, 13
- Wieringa, M., de Bruyn, A.G., Jansen, D., et al.: 1993, A&A 286, 215
- Williams, A.L., Heald, G., Wilcots, E.M., Zweibel, E.G.: 2018, ApJ, submitted
- Wolleben, M., Reich, W.: 2004, A&A 427, 537
- Wolleben, M., Landecker, T.L., Reich, W., Wielebinski, R.: 2006, A&A 448, 411
- Wolleben, M., Landecker, T.L., Carretti, E., et al.: 2009, in *Cosmic Magnetic Fields: From Planets, to Stars and Galaxies*, eds. K.G. Strassmeier et al., Cambridge UP, Cambridge, p. 89
- Wolleben, M., Landecker, T.L., Hovey, G.J., et al.: 2010a, AJ 139, 1681
- Wolleben, M., Fletcher, A., Landecker, T.L., et al.: 2010b, ApJ 724, L48
- Wu, Q., Kim, J., Ryu, D.: 2015, New Astr 34, 21
- Xiao, L., Han, J.L., Reich, W., et al.: 2011, A&A 529, A15
- Xu, J., Han, J.L.: 2014, RAA 14, 942
- Yates, K.W.: 1968, Aust. J. Phys. 21, 167
- Yoast-Hull, T.M., Everett, J.E., Gallagher III, J.S., Zweibel, E.G.: 2013, ApJ 768:53
- Yusef-Zadeh, F., Morris, M., Chance, D.: 1984, Nat 310, 557
- Yusef-Zadeh, F., Roberts, D.A., Goss, M.W., et al.: 1996, ApJ 466, L25